

# Spin-Orbit Coupling in Optical Superlattices

by

Wujie Huang

Submitted to the Department of Physics  
in partial fulfillment of the requirements for the degree of

Doctor of Philosophy

at the

MASSACHUSETTS INSTITUTE OF TECHNOLOGY

February 2016

© Massachusetts Institute of Technology 2016. All rights reserved.



Author .....  
Department of Physics  
October 19, 2015

Certified by .....  
Wolfgang Ketterle  
John D. MacArthur Professor of Physics  
Thesis Supervisor

Accepted by .....  
Nergis Mavalvala  
Professor of Physics, Associate Department Head for Education



# Spin-Orbit Coupling in Optical Superlattices

by

Wujie Huang

Submitted to the Department of Physics  
on October 19, 2015, in partial fulfillment of the  
requirements for the degree of  
Doctor of Philosophy

## Abstract

Quantum simulation is emerging as an exciting and active frontier in atomic physics. It allows us not only to verify existing models with high precision, but also to engineer novel systems with strong correlations and exotic topologies. Recent efforts have been made to include synthetic gauge fields and spin-orbit couplings into ultracold quantum gas experiments, which would enable us to study the quantum Hall effect, topological insulators as well as topological superfluids. This thesis will describe the experimental implementation of a new spin-orbit coupled system using pseudospin-1/2 in an optical superlattices, as well as progress towards detecting the stripe phase in this system.

The first part of this thesis describes the development of a new apparatus for performing quantum simulations with sodium and lithium in optical lattices. A quantum simulation program is challenging itself, therefore having a stable platform for preparing quantum gases is essential for this task. We'll describe our development in reliable and efficient production of sodium Bose-Einstein condensates and lithium degenerate Fermi gases, as well as the characterization of our optical lattice system in a superfluid to a Mott-insulator quantum phase transition. The dynamics of a Bloch oscillation in a tilted lattice has also been studied as an important step towards the implementation of synthetic magnetic fields in our system.

The second part of this thesis describes the experimental realization of spin-orbit coupling in a pseudospin-1/2 system using an optical superlattice. This new scheme uses orbital states in a tilted double-well as the pseudospins, therefore does not require near-resonant Raman light to flip the spins and promise longer lifetimes compared to earlier spin-orbit coupling experiments in atomic gases. It also features a robust miscible ground state with stationary density stripes, which is closely related to the concept of supersolidity in condensed matter systems. We'll present our experimental implementation of this new system, signatures of the resonant spin-orbit coupling, as well as progress toward experimental detection of the stripe phase via Bragg scattering. This pseudospin-1/2 system could also be used for simulating quantum magnetism, and potentially novel models with topological properties and Majorana excitations.

Thesis Supervisor: Wolfgang Ketterle  
Title: John D. MacArthur Professor of Physics

## Acknowledgments

First and foremost, I'd like to thank my research advisor Prof. Wolfgang Ketterle for showing me the wonderful physics in cold atom systems, and providing me this great opportunity to carry out the experimental research. I want to sincerely thank you for giving me encouragement, freedom and guidance throughout the years.

During my Ph.D. I've worked with a number of very talented and generous people on the BEC2 experiments. Christian is an expert in optics and electronics as well as a very patient and supportive teacher and friend. He taught me useful experimental techniques when I joined this lab with little experience, and also guided me to explore other aspects of life. Aviv has a great amount of positive energy, and commitment to making everything great. I'm impressed by his engineering and programming talent in building this formidable machine and the word generator. Our postdoc Jon's early work in developing the frequency doubling for green light turned out to be crucial for our superlattice experiments. In addition, I'd like to thank Jon for making our lab trip to Foxwoods possible: it was a memorable experience. Thanks to Ed, for staying patient and positive throughout the difficult times in developing our new apparatus. There's no doubt that you are very talented and have good character, and I wish you success in your new journey.

In the latest spin-orbit coupling experiment carried out with the new apparatus, I've worked with a number of very promising young talents. Junru has always been a great labmate that one can rely on. He is not afraid to make changes to the existing setup, and always does his best to bring the machine back to the working condition when something stops functioning. Fixing the machine can sometimes be frustrating, however, you have all the good qualities one needs to carry out excellent research. I wish you best of luck! Boris is a great addition to the lab to bring BEC2 social life alive. Thank you for your efforts to make our lab roadtrip possible. With your hard work and commitment, I'm sure you will soon become the new master of the BEC2 machine. Furkan's attention to the details and perfection in his lab projects and our latest data analysis surprised me. I see great potential from you. Our UROP student

Sean really impressed me with what a MIT undergrad can do in his/her dorm room. I cannot wait to see you play a more important role in the future experiments.

I'd like to thank Prof. Martin Zwierlein for being my academic advisor throughout my years at MIT, and also serving my thesis committee. Thank you for the inspiring and encouraging discussions at the start of every semester. I look forward to hearing your continuing great success and exciting new results from your group.

I'd also like to thank everyone in the Ketterle group for lending me equipments, sharing technical insights and generating fruitful discussions in our plenary meeting. I'd like to especially thank colleagues who have considerable overlap with me in my years at MIT: Thanks to Timur, Tout, Myoung-Sun and Alan in BEC3 for being a great neighbor, and lending us a hand whenever needed; Thanks to Colin, Cody, Woo Chang, Hiro and David in BEC4 for stimulating insightful discussions and sharing experimental techniques they've developed in the rubidium lab; Thanks to Niki, Jesse and Ivana in BEC5 for spreading smiles and laughs across the hallway, and sharing your expertise in designing electronic circuits and reducing laser noise. It has been a privilege for me to work in this group and I'll miss all of you.

It is also a great pleasure to work in the CUA community. I met Mark on the first day I came to MIT, and thank you for being a great friend and offering me invaluable help along the years. I'd also like to thank Peter, Sebastian, Cheng, Ibon, Payman in Fermi1 lab, and Ariel, Tarik, Waseem, Lawrence, Melih, Matt in BEC1/Fermi2 lab, as well as Hao, Wenlan, Molu, Alexei in the Vuletic group. I want to thank each one of you for your generous help and the great memories together.

I want to thank the Chinese community at MIT to make me feel like home and be able to focus on my study and research. I want to thank my friends in the Department of Physics, including Wenjun Qiu, Bo Zhen, Yannan Zheng, Yabi Wu, Wenlan Chen, Jiazhong Hu, Jiexi Zhang, Hao Zhang, Mingming Yang, Lu Feng, Lei Dai and others. I'd like to thank everyone in the CSSA basketball team. It was my great pleasure to serve as your captain for two years. It was probably the most memorable highlight of my life at MIT.

I want to thank the ones I had once fallen in love with. You gave me passion, and

made me take a pause to appreciate the beauty of life besides science.

I'd like to thank my advisors and mentors in Tsinghua, Hui Zhai and Prof. Lee Chang, for guiding me into this exciting field and setting the high standards of being a physicist.

Last and certainly not least, I would like to thank my parents and brother for the unconditional support. As I said during my thesis defense, "there is only one home, and that's the place I miss so much at this moment".



# Contents

<b>1</b>	<b>Introduction</b>	<b>19</b>
1.1	Background . . . . .	19
1.1.1	Quantum simulation . . . . .	19
1.1.2	Cold atoms as quantum simulators . . . . .	20
1.1.3	A brief history . . . . .	20
1.2	Thesis Outline . . . . .	21
<b>2</b>	<b>Production of Quantum Degenerate Gases</b>	<b>23</b>
2.1	Overview of the Experimental Apparatus for $^{23}\text{Na}$ - $^6\text{Li}$ in Optical Lattices	25
2.2	Condensation of $^{23}\text{Na}$ in the $F = 1$ Hyperfine State . . . . .	31
2.2.1	Single-species $^{23}\text{Na}$ MOT . . . . .	32
2.2.2	Evaporative cooling in a plugged magnetic-quadrupole trap . . . . .	33
2.2.3	BEC in an optical dipole trap . . . . .	35
2.3	Sympathetic Cooling of $^6\text{Li}$ with $^{23}\text{Na}$ in the $F = 2$ State . . . . .	36
2.3.1	The hyperfine states of $^6\text{Li}$ and $^{23}\text{Na}$ . . . . .	37
2.3.2	Condensation of $^{23}\text{Na}$ in the $F = 2$ hyperfine state . . . . .	38
2.3.3	Sympathetic cooling of $^6\text{Li}$ with $^{23}\text{Na}$ . . . . .	39
2.4	Hyperfine State Preparation of $^{23}\text{Na}$ . . . . .	41
2.4.1	Microwave transitions between hyperfine states . . . . .	42
2.4.2	Radio-frequency transitions between hyperfine states . . . . .	43
2.4.3	Two-photon transitions between hyperfine states . . . . .	44

<b>3</b>	<b>Bose-Einstein Condensates in Optical Lattices</b>	<b>45</b>
3.1	Introduction . . . . .	45
3.2	Basic Lattice Physics . . . . .	47
3.2.1	Band structure and Bloch states . . . . .	47
3.2.2	Tight binding and Wannier states . . . . .	50
3.2.3	Lattice calibration via Kapitza-Dirac diffraction . . . . .	53
3.3	Superfluid to Mott-Insulator Quantum Phase Transition . . . . .	54
3.3.1	Mean-field theory for a Bose-Hubbard model . . . . .	54
3.3.2	Observation of the superfluid to Mott insulator transition . . . . .	62
3.4	Tilted Lattices and Bloch Oscillations . . . . .	64
3.4.1	Bloch oscillation . . . . .	65
3.4.2	Dynamical instability . . . . .	66
<b>4</b>	<b>Quantum Simulation in Superlattices</b>	<b>71</b>
4.1	Introduction . . . . .	71
4.2	Experimental Setup and Techniques . . . . .	74
4.2.1	Second-harmonic generation for 532 nm green lattice . . . . .	74
4.2.2	Controlling the phase of the superlattice . . . . .	77
4.2.3	Considerations for the Raman beams . . . . .	85
4.2.4	Experimental layout . . . . .	86
4.3	Experimental Characterization and Calibration of a Superlattice . . . . .	86
4.3.1	Superlattice band structure . . . . .	87
4.3.2	Calibration and dynamical control of the superlattice phase . . . . .	89
4.3.3	Interband population transfer and band mapping . . . . .	95
4.4	Theory of Spin-Orbit Coupling in a Superlattice . . . . .	99
4.4.1	Single-particle spin-orbit coupling Hamiltonian . . . . .	100
4.4.2	Spin-orbit coupling and onsite couplings . . . . .	104
4.4.3	Quantum phase transition of an interacting spin-orbit coupled condensate . . . . .	106
4.5	Experimental Realization of Spin-Orbit Coupling in a Superlattice . . . . .	108

4.5.1	State preparation in a superlattice . . . . .	108
4.5.2	Dynamics in the double-wells . . . . .	110
4.5.3	Detection of the spin-orbit coupling in time-of-flight . . . . .	112
4.5.4	Experimental observation of resonant spin-orbit coupling . . . . .	120
4.5.5	Detection of the spin-orbit coupling in Bragg scattering . . . . .	122
<b>5</b>	<b>Density Fluctuations in Quantum Degenerate Fermi Gases</b>	<b>127</b>
<b>6</b>	<b>Outlook and Conclusion</b>	<b>129</b>
6.1	Outlook . . . . .	129
6.2	Conclusion . . . . .	131
<b>A</b>	<b>Suppression of Density Fluctuations in a Quantum Degenerate Fermi Gas</b>	<b>133</b>
<b>B</b>	<b>Speckle Imaging of Spin Fluctuations in a Strongly Interacting Fermi Gas</b>	<b>143</b>
<b>C</b>	<b>Correlations and Pair Formation in a Repulsively Interacting Fermi Gas</b>	<b>149</b>
<b>D</b>	<b>Kapitza-Dirac Diffraction Simulation</b>	<b>159</b>
<b>E</b>	<b>Superlattice Band Structure Calculation</b>	<b>163</b>
<b>F</b>	<b>Simulation of Double-Slit Interference Pattern in a Superlattice</b>	<b>167</b>



# List of Figures

2-1	Overview of BEC2 sodium-lithium apparatus. . . . .	26
2-2	Layout of the optics on the experimental table. . . . .	31
2-3	Evaporative cooling of F=1 Na with radio-frequency . . . . .	34
2-4	Evaporative cooling of F=1 Na with 1.7 GHz microwave . . . . .	35
2-5	Hyperfine structures of $^{23}\text{Na}$ and $^6\text{Li}$ . . . . .	37
2-6	Gravity-assisted spin purification and optical pumping of F=2 Na . . . . .	38
2-7	Sympathetic cooling of Li with F=2 Na . . . . .	40
2-8	Sympathetic cooling efficiency . . . . .	41
2-9	Spin flip via Rapid Adiabatic Passage: the Landau-Zener sweep . . . . .	42
2-10	Rabi oscillations in spin flip . . . . .	43
2-11	Spin flip with radio-frequency and the Stern-Gerlach experiment . . . . .	43
2-12	Spin flip via two-photon transition . . . . .	44
3-1	Band structure of a one-dimensional optical lattice . . . . .	49
3-2	Bloch states in optical lattices . . . . .	50
3-3	Wannier states in the lowest band . . . . .	51
3-4	Kapitza-Dirac diffraction patterns . . . . .	53
3-5	Experimental calibration of the lattice depth via Kapitza-Dirac diffraction . . . . .	54
3-6	Numerical calculation of tunneling $t$ and on-site interaction $U$ . . . . .	57
3-7	Bose-Hubbard model phase diagram . . . . .	59
3-8	Bose-Hubbard model phase diagram in an inhomogeneous system . . . . .	60
3-9	Wedding-cake density profile in a harmonic trap . . . . .	61

3-10	Experimental observation of superfluid to Mott insulator transition . . .	63
3-11	Mott insulator lifetime measurement . . . . .	64
3-12	Experimental demonstration of Bloch oscillations . . . . .	66
3-13	Experimental observation of dynamical instability . . . . .	67
3-14	Relaxation of quasi-momentum states near the edge of the brillouin zone	69
4-1	The spin-orbit coupling band structure . . . . .	72
4-2	The pseudo-spin scheme to simulate spin-orbit coupling physics . . .	73
4-3	Optimal crystal temperature for 532 nm second-harmonic generation	76
4-4	532 nm second-harmonic-generation conversion efficiency . . . . .	77
4-5	Superlattice phase control via AOM frequency shifter . . . . .	81
4-6	Experimental schematics of the superlattice experiment . . . . .	87
4-7	Diffraction patterns of various beams . . . . .	88
4-8	Band structure of the superlattice . . . . .	90
4-9	Predicted time-of-flight patterns of the Raman-coupled $p = +k_L$ states	91
4-10	Superlattice phase calibration via diffraction . . . . .	91
4-11	Experimental sequence for the dynamical control on superlattice phase	92
4-12	Experimental demonstration of dynamical control on the superlattice phase . . . . .	93
4-13	Measurement of long-term drifts of the superlattice phase . . . . .	95
4-14	Interband population transfer in a 1064 nm lattice via amplitude mod- ulation and Raman coupling . . . . .	96
4-15	Interband coupling resonances and the band structure in a 1064 nm lattice . . . . .	97
4-16	Raman coupling into higher bands in a green lattice in TOF . . . . .	99
4-17	Quantum phases of an interacting spin-orbit coupled condensate . . .	107
4-18	Experimental calibration of the energy offset $\Delta$ . . . . .	111
4-19	The ground states of the lowest two bands in the superlattice . . . . .	112
4-20	Relaxation into the ground state in the second band . . . . .	113

4-21	The relative phases and the corresponding interference of the $k = 0$ component for 50/50 population . . . . .	116
4-22	The relative phases and the corresponding interference of the $k = \pm k_L$ component for 100/0 population with only the OC or SOC . . . . .	117
4-23	The relative phases and the corresponding interference of the $k = \pm k_L$ component for 100/0 population with both the OC and SOC . . . . .	118
4-24	No interference between quasi-momentum $q = 0$ and $q = k_L$ states . .	119
4-25	Typical time-of-flight image in the spin-orbit coupling experiment . .	120
4-26	Resonant spin-orbit coupling measurement . . . . .	121
4-27	The stationary stripes and moving density modulations . . . . .	123
4-28	Bragg scattering experiment for detecting the stripe phase . . . . .	124



# List of Tables

4.1	The index of refraction for 532/1064 nm in glass . . . . .	78
4.2	The natural units in 532/1064 nm superlattices . . . . .	89
4.3	The Bragg angles for detecting the stripe phase . . . . .	125



# Chapter 1

## Introduction

### 1.1 Background

#### 1.1.1 Quantum simulation

The idea of quantum simulation originates from remarks made by Richard Feynman in 1982, that physical systems can be hard to simulate with a computer. This statement is particularly true for quantum systems, as the memory required to represent a state (space complexity) and the time required to do computations (time complexity) with them increase exponentially with the number of degrees of freedom being simulated.

One way to overcome the difficulties is to design and build novel quantum computers. They perform unitary operations instead of logic gates, and operate on quantum bits instead of classical bits. Because of their vastly larger state space and greater computational power, quantum computers could allow us to tackle difficult problems that are not tractable with classical machines. To make scalable and robust quantum computers is currently a field of enormous activity and interest.

Another promising solution is to simulate the same problem in a different quantum system. Assuming physics is universe, studying problems in a clean and well controlled setting allows us to gain an edge in solving them, as well as to engineer novel quantum models to be explored.

### 1.1.2 Cold atoms as quantum simulators

Since the first realization of Bose-Einstein condensation and later Fermi degeneracy of neutral atomic gases, ultracold atoms have shown themselves to be an ideal candidate for quantum simulations. Bose condensates and degenerate Fermi gases are pure forms of quantum matter. Furthermore, the diluteness of the atomic clouds and their weak couplings to the environment allow them long coherence times for quantum simulation experiments.

The powerful toolbox for preparing, manipulating and probing atoms for quantum simulations has been developed over the years. Here I'd like to mention a few examples to demonstrate the powerfulness and convenience of these tools. First, optical lattices are created by interfering laser beams. By changing the geometry and polarization of the beams, we are able to make cubic, triangular, checkerboard or other very different lattices in a single experimental setup. Second, Feshbach resonances would allow us to tune the two-body interactions, ranging from strong attractions to strong repulsions. Finally, atoms can be imaged in absorption, phase contrast, or single atom detection via fluorescence [5]. All of these tools make the ultracold atom system particularly attractive, and greatly facilitate the quantum simulation program.

### 1.1.3 A brief history

The field of quantum simulation using ultracold atoms has become diverse in recent years. To me still, there are focused efforts in the following directions. The first one is to simulate the Bose-Hubbard model with a single-component Bose gas in 3D optical lattices. The quantum phase transition from a superfluid to a Mott insulator has been observed in this system [15]. With newly developed microscopy techniques and single-site resolution imaging, one can characterize the system with high precision [16, 17].

The second direction is to simulate the Fermi-Hubbard model with an interacting two-component Fermi gas in optical lattices. This is partly motivated by the high- $T_c$  superconductivity and quantum magnetism. Experimental progress in this direction includes observation of fermionic superfluid [3], band insulator and Mott insulator [19,

20], and most recently results on probing the anti-ferromagnetic correlations near the Néel transition [21, 22].

In the past five years or so, a third direction has emerged to simulate gauge fields, spin-orbit couplings and topological states. New lattice modulation and laser-assisted techniques have been developed to generate complex tunneling amplitudes. Highlights in this direction so far include creating strong synthetic magnetic fields [23, 24, 25, 26], and realizing novel Hamiltonians with topological properties [27, 28]. These exciting developments have opened up a whole new phase of quantum simulations in ultracold atoms, and motivate the work that will be presented in this thesis.

## 1.2 Thesis Outline

This thesis will present progress towards experimental realization of exotic Hamiltonians in optical lattices, including spin-orbit couplings in an optical superlattice and subsequent experimental detection of the stripe phase, as well as synthetic magnetic fields. It is organized as follows.

- **Chapter 2** presents an overview of the new apparatus, and discusses technical details of the development of the machine after its initial construction, including the creation of its first Bose-Einstein condensates and degenerate Fermi gases, as well as the techniques for spin state preparation.
- **Chapter 3** introduces the physics in optical lattices, and describes the development of building and characterizing our optical lattice system. It also discusses our studies of dynamical instability in tilted lattices and progress towards implementing synthetic magnetic fields.
- **Chapter 4** discusses the experimental realization of spin-orbit coupling in the pseudospin-1/2 system in an optical superlattice. It will detail how to create, control and characterize the superlattice, as well as the experimental detection of the spin-orbit couplings and the stripe phase.

- **Chapter 5** briefly describes three density fluctuation measurements in a Fermi gas. These experiments were performed in an apparatus that was later decommissioned.
- **Chapter 6** presents an outlook for the future directions of the experiment and the conclusion.

## Chapter 2

# Production of Quantum Degenerate Gases

When I first joined this lab in 2009, I was totally shocked to see the seemingly fragile glass cell surrounded by complicated magnetic coils, and cables and fibers were over the place tangled up on the ceiling and floor. It is still a mystery to me how I managed to learn and operate such a formidable apparatus in the following two years without any prior experience, and together with my labmates to carry out the atomic density fluctuation experiments with it.

This old apparatus, originally built in 1998, was the second of its kind on this hallway to perform BEC experiments [1]. It had been upgraded to a dual-species sodium-lithium machine [2], and become one of the first machines to achieve quantum degeneracy in fermions. In the following years, old generations of BEC2 people had produced a series of pioneering works, including the first observation of fermionic superfluidity in optical lattices [3] and the study of critical velocity of fermionic superfluidity in the BCS-BEC crossover [4].

However, by the time I joined this lab, the old BEC2 apparatus already started to show limitations for our long-term goal, which is to carry out quantum simulation in optical lattices. It often required a few hours of tweaking and optimizing for a proper performance, and was only stable enough to operate late during the night. In addition, it had many layers of unnecessary complexity, partially because of its long history

of upgrades, making it difficult to adapt changes for new experiments. Furthermore, vacuum in the main chamber started to degrade, as a few key components such as gate valves and titanium filaments begun to fail. These would ultimately limit our cloud lifetime for studying superexchange physics in optical lattices. In the end, the decision was made to develop a next-generation apparatus for optical lattice experiments.

The primary focuses of designing the new apparatus are the reliability, versatility, and low complexity. Consistent performance and low maintainance of the new apparatus could allow us to work more efficiently and concentrate on the experiment itself. For example, we have built enclosures with individual temperature stabilization to have much better control of ambient temperature fluctuations. We have also switched to a solid state laser system from the notorious dye laser for producing 589 nm light, and carefully considered the mechanical stiffness and stability of mounting techniques against beam drifts.

In addition, the design of our new apparatus aimed for versatility rather than for one particular strength or area of research such as single-site resolution microscope experiments [5] or multi-species cold molecule experiments (e.g., Na-Li-K [6]). We decided to continue the Ketterle group tradition of making general purpose cold atom machines, which may not be the ultimate tool for any specific study, but are suitable to a wide variety of experiments.

Finally, in the new apparatus we have also tried to design built-in features that reduce unnecessary complexity and facilitate future upgrades. For instance, we have MOT light prepared on the back side of the main breadboards, and delivered with translation stages so that it does not interfere with future use of high value surfaces of these breadboards. We selected a much simpler plugged quadrupole magnetic trap design, compared with the more complicated Ioffe-Pritchard design used previously. Almost all laser beams are fiber coupled and delivered so that the experimental table is decoupled from light preparation.

While the noise measurements were being carried out in 2011, the next-generation apparatus was already in the process of being designed and prepared by the members of the lab. Its initial design and construction are described in detail in Aviv Keshet's

thesis [7]. Edward Su and I took over the machine from the point of its first magneto-optical trap, and eventually made our first sodium BEC in the new apparatus a year after. Some technical details of the design and implementation for the development in this phase can be also found in Edward Su’s thesis [8]. After another year of work on cooling lithium and testing the new optical lattice system, now we are on the verge of pushing the frontier of quantum simulation in optical lattices again.

This chapter will describe our efforts to reliably and efficiently produce quantum gases for optical lattice experiments. First we’ll provide a brief overview of our new apparatus in its current state. We’ll then discuss a few key developments in the process of achieving quantum degenerate gases of sodium and lithium in this apparatus. Finally, we’ll describe the techniques to manipulate the hyperfine states of sodium as a way to prepare the states. This chapter is by no means a complete guidebook for designing and constructing a new apparatus for quantum gases experiments. For that, the reader is advised to refer to early theses in Ketterle lab [1, 2, 7, 9] and references therein.

## 2.1 Overview of the Experimental Apparatus for $^{23}\text{Na}$ - $^6\text{Li}$ in Optical Lattices

The new BEC2 apparatus is a general-purpose machine for  $^{23}\text{Na}$  and  $^6\text{Li}$  dual-species experiments. It shares some features with machines that were built around the same time in Fermi1 (for  $^{23}\text{Na}$ - $^6\text{Li}$ - $^{40,41}\text{K}$ ) and BEC5 (for  $^7\text{Li}$ ) on the hallway of the CUA. The following contains a brief description of this apparatus.

Fig. 2-1 presents an overview of the whole apparatus. A two-species oven on the far right is the source for  $^{23}\text{Na}$  and  $^6\text{Li}$  atoms. The oven chamber is connected through a differential pumping tube to a small intermediate chamber, which is then connected to the main chamber at the beginning of the Zeeman slower through a second stage of differential pumping. The oven-to-intermediate and intermediate-to-main interfaces can be sealed off with VAT gate valves, allowing the main chamber to be kept under

ultra-high vacuum during oven refills. The intermediate chamber provides additional differential pumping and acts as a buffer protection, so that the intermediate-to-main gate valve sits in a cleaner environment and is less likely to fail. Each of these vacuum chambers is monitored by its own vacuum ion gauge, and constantly pumped by its own ion pump.

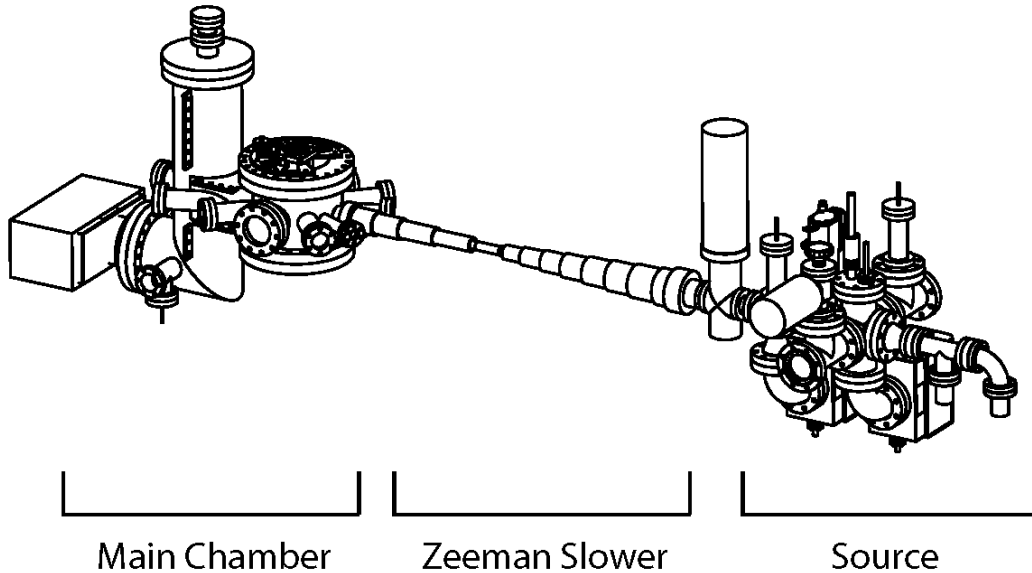


Figure 2-1: Overview of our sodium-lithium apparatus. The oven cups (right) containing sodium and lithium are heated up to produce atomic beams, which are then cooled through the Zeeman slower (middle) and trapped in the main chamber (left). The main chamber on the left is a custom-made steel chamber with numerous viewports for optical access and high-current magnetic coils mounted in the vertical buckets. This figure is adapted from [7].

### Main vacuum chamber

The main chamber is designed to prioritize optical access, and to accommodate the bucket windows, with two on the top and bottom, and one on the side. The bucket window design allows us to bring coils and optics much closer to the atomic cloud, and therefore achieve strong magnetic fields and high resolution imaging. All viewports are given a multi-wavelength coatings optimized for 532 nm, 589 nm, 671 nm, and 1064 nm, except the side bucket window and its facing viewport were given a single-V

anti-reflection coating for 671 nm, intended to be the best-performing imaging axis for lithium.

## **Magnetic coils**

The high-current magnetic coils are mounted inside the top and bottom buckets to provide strong magnetic fields. Each of them was wound with five individual layers, which were then wired in series and combined into an outer and inner segment. Both segments in the top-bucket coil can be configured, via a mechanical relay H-bridge, into a Helmholtz or anti-Helmholtz configuration with its counterpart in the bottom bucket, making the new coil system really easy to switch and reconfigure. These high-current magnetic coils are constantly cooled with pressurized water, designed to handle the power consumption at 500 A. When running this current in both segments, the Helmholtz configuration yields a bias field over 1000 G, and the anti-Helmholtz configuration yields a magnetic field gradient of 1000 Gauss/cm, readily covering the broad s-wave Feshbach resonance of  ${}^6\text{Li}$  near 830G, and the strong magnetic gradient needed for fast evaporative cooling.

## **Temperature stabilization**

Ambient temperature and humidity stabilization is crucial for the success of atomic physics experiments. The old BEC2 experiments suffered terribly from this problem, as the room temperature could drift a few degrees over the day, and the only practical hours of data taking were in the middle of the night.

To address this problem in the new apparatus, we have upgraded the room temperature stabilization system, and more importantly, have built enclosures and individual temperature control for the experiment and laser tables. The details of our new temperature stabilization system can be found in [7]. In practice, the daily room temperature fluctuates within a couple of degrees, and the ambient temperature on the tables fluctuates around tenth of a degrees, when the enclosure doors are fully closed. To keep the machine away from extreme high humidity, we have also installed a stand-alone dehumidifier to supplement the existing dehumidification performed by

the air conditioners, and maintain the room humidity always below 35%.

### **Solid-state 589 nm laser system**

For our sodium BEC experiments, a laser source at 589 nm of at least 1.4 Watts and with a linewidth of about 1 MHz or better is required. Historically, this was achieved by using a tunable dye laser with Rhodamine 6G dye in BEC2. However, the dye laser was notoriously difficult to operate, and was a major source of experiment downtime.

Finally, it was replaced by a turnkey all-solid-state system from MPB Photonics. This scheme was made possible by recent advances in the Raman amplifiers. In this system, the 1178 nm light from a Toptica DL pro diode laser is amplified through the Raman amplifier to about 5.8 Watts, and then frequency-doubled to create the 589 nm yellow light.

This compact package offers an almost maintenance-free yellow laser solution, and we are in general very happy about it. There is one caveat that I want to mention: even though MPB claims the minimal threshold of seed power is 13 mW, this value is way below the saturation limit. This means, a stronger seed always generates more yellow light. On the other hand, a weaker seed requires the Raman amplifier to run at a higher current to maintain the same final yellow output, which shortens the lifetime of the pump diodes.

In practice, we run this system at a seed power greater than 25 mW, and will get a total output of 1.35 W yellow light. The degradation from 30 mW to 20 mW of the maximum seed from the Toptica laser is observed over the past two years. Therefore to overcome this degradation, one has to either replace the Toptica laser diode in the near future, or to look for alternatives of the seed, such as the promising distributed feedback lasers (DFB) that provide high power at low cost.

### **532 nm plug laser**

In the new apparatus, we abandoned the Ioffe-Pritchard trap in favor of the quadrupole trap, because of its simplicity in design and convenience in use. However, different from the Ioffe-Pritchard trap in which a harmonic trap is created on top of a bias field,

the simplest quadrupole trap with a pair of coils run current in opposing directions always creates a zero magnetic field at the trap center. As the magnetically trapped atoms pass through the trap center of zero field, their magnetic dipoles cannot adiabatically follow the field direction, causing them to undergo Majorana spin flips to the untrapped states and get ejected from the trap.

The problem was solved by either moving the zero field point around to create a time-averaged trapping potential, the so-called TOP trap in JILA experiments [10], or by combining the magnetic potential with a repulsive [11] or attractive [12] optical potential so that the atoms are trapped away from the region of zero field.

In our experiment, we have a 10-Watt 532 nm laser Millennia from Spectra Physics used as a repulsive optical potential to plug the zero magnetic field. It's an old laser and has already shown its aging. With a degraded output of 6 Watts, we are still able to keep the machine running. However, if the old pump diodes fail, one could either get diode replacement for the old laser directly from Spectra Physics if the cost is low, or consider buying newer cost-effective lasers discussed in section 4.2.1, or multitask the frequency-doubled green light for both the plug and the superlattices.

### **High power 1064 nm system**

Far-off-resonant light is used to generate optical dipole traps and optical lattices for quantum gases experiments. To study exotic states in quantum simulation with optical lattices, especially physics deep in the Mott-insulator such as quantum magnetism, it is often desirable to work at low densities near one particle per site, and we want large lattice beams with low curvature and simultaneously enough intensity to reach deep into the Mott insulator regime. This in practice means a few Watts per beam for sodium, and up to 10 Watts per beam for lithium. Safely, reliably and efficiently making and controlling high-power light is essential for our experiments..

With high-power laser beams, it's important to carefully choose optics with high optical damage threshold and low thermal drifts, since these damages are irreversible and some of these drifts are hard to trouble-shoot. It is highly recommended to take these factors into considerations at the designing phase. Based on our experience, it

is preferred to use high-power optics for a millimeter beam with more than a couple of Watts. These include high-power AOMs, high-power fibers and connectors, fused-silica lenses and air-spaced polarizing beamsplitting cubes.

We have several water-cooled fused-silica AOMs from AA Opto-Electronic to intensity stabilize 20-Watt 1064 nm beams. These AOMs have large aperture (2-3 mm), high diffraction efficiency ( $\sim 90\%$ ) and relatively low thermal drifts. However, fused-silica AOMs have a low figure-of-merit in the acousto-optic effect, and therefore needs a strong RF signal to drive (in our case about 30 Watts). The best alternative seems to be AOM made in Tellurium dioxide ( $\text{TeO}_2$ ), which is rated at a lower maximum CW laser power of  $5 \text{ W/mm}^2$  but requires less RF. We get these AOMs from IntraAction.

For high power fibers, we use photonic crystal fibers from NKT Photonics, with the maximum available mode area, which are the LMA-25 series without polarization maintaining, and the LMA-PM-15 series with polarization maintaining. These fibers are all end-sealed and custom connectorized to SMA-905 high-power connectors by a French technology center called Alphanov. These high-power connectors are rated to handle beams up to 50 Watts. In practice, we found no major thermal issues for a 10 Watts CW input without any active cooling. By installing thermoelectric coolers (TEC) on these connectors to transfer away the excessive heat, other labs reported that no severe thermal drifts were found with more than 20 Watts CW light. Finally, we use fiber collimators with fused silica components from Micro Laser Systems (FC5-Y-FS) or large area collimators from Schäfter+Kirchhoff GmbH (60FC-SMA series).

## Optics layout

Because of its superior mechanical stability, the horizontal axes tend to be the busiest in terms of optics density, as sensitive beams are preferred to be installed in this plane. A schematic diagram of the optics layout in the horizontal plane is shown in Fig. 2-2. The two  $45^\circ$  axes with large viewports are shared by the MOT beams and the lattice beams, and the two smaller  $22.5^\circ$  windows are used by the plug and optical repumping beam separately. Imaging is available along most major axis for easy beam alignment and flexible detection. In addition, there are a pair of MOT beams, an optical lattice

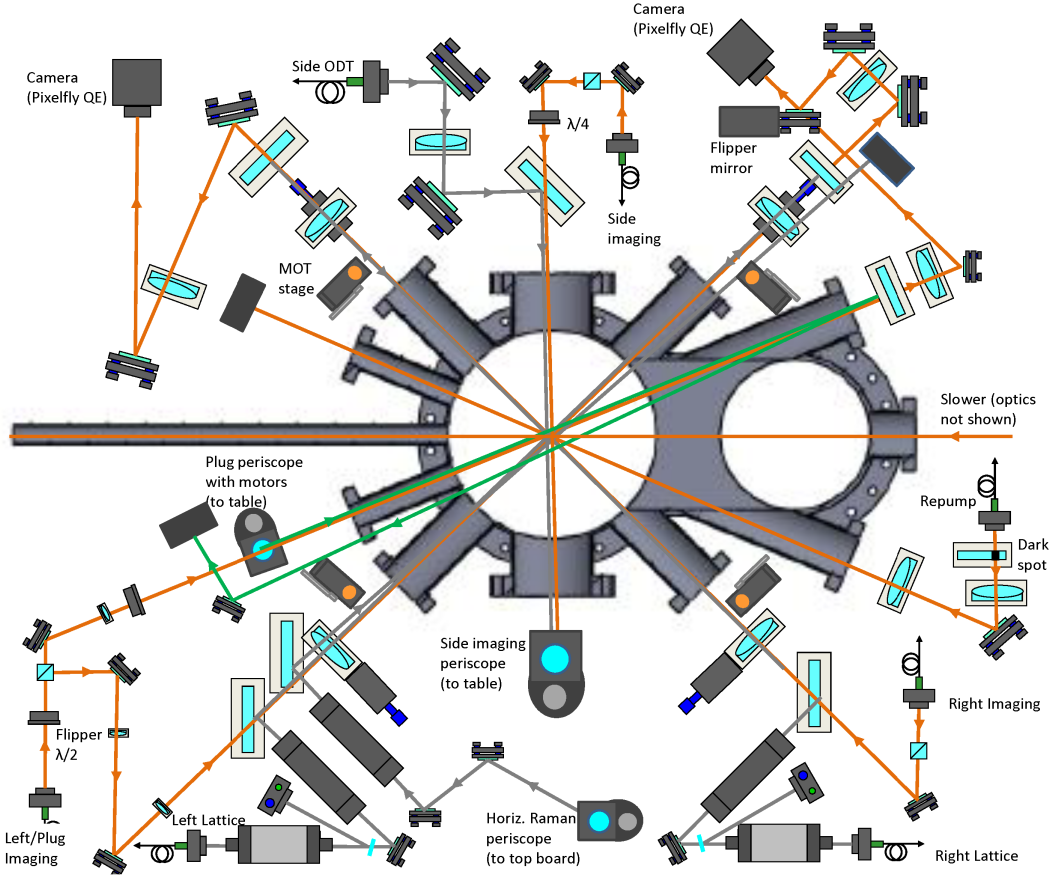


Figure 2-2: Layout of the optics on the experimental table. This diagram illustrates the layout of the optics in the horizontal plane, including the plug beam and two lattice beams in orthogonal axes shared by MOT beams. Imaging are available along the plug axis, both horizontal lattice axes, the vertical axis, as well as the side axis. This figure is adapted from [8].

beam, as well as the primary imaging along the vertical axis, which are not shown in this diagram.

## 2.2 Condensation of $^{23}\text{Na}$ in the $F = 1$ Hyperfine State

In the following two sections, we will describe the development of making quantum degenerate gases of sodium and lithium in our new apparatus. These discussions will be mainly focused on the benchmark results in every stage for this particular machine,

as well as the experimental techniques that we've found useful in troubleshooting and performance evaluation. For general introduction and broader aspects of cooling  $^{23}\text{Na}$  and  $^6\text{Li}$  into quantum degeneracy, please also refer to the pioneering works in [2, 9].

### 2.2.1 Single-species $^{23}\text{Na}$ MOT

The traditional dark-spot MOT of sodium is used in our experiment to trap as many sodium atoms as possible [13]. Typically, our MOT loading takes about 8 seconds, and then we transfer the sodium atoms from the dark-spot MOT into the magnetic trap with a vertical axial gradient of 50 G/cm,

Once the first MOT is obtained, critical components such as the slower frequency and repumping sidebands, the MOT light polarization, and the dark-spot alignment in the repumping beam are within the working range and unlikely to change. However, there are pieces that might potentially drift over the weeks and deteriorate the MOT. Based on our experience, the top candidates are the power balance in each pair of the counter-propagating MOT beams, the current in the last section of the slower which defines the final velocity of the decelerated atoms in the main chamber, and of course the laser lock and total yellow light output. In most cases, by checking through this list, one could recover a decent sodium MOT for the experiment.

When something has drifted away from its proper settings, it might be confusing to figure out what's wrong and how to make improvement. In this case, we find setting up a MOT loading monitor very helpful for debugging the system [13]. A very weak probe beam is sent through the cloud with a continuous frequency scan of over 100 MHz (via two double-passed AOMs) near the sodium D2 line. For a decent dark-spot MOT with very high atomic density, a plateau of over 50 MHz with nearly complete absorption is expected, and the excited-state hyperfine structure could no longer be resolved. Similarly, a MOT fluorescence detector can be set up to diagnose the slower performance in the MOT loading, as well as the transfer efficiency from the dark-spot MOT to the magnetic trap.

If the MOT loading is very slow, another possibility could be the alkali in the oven is depleted. Usually, we need to refill the sodium oven almost every year, while the

lithium oven is running at a conservative temperature and is expected to last for the entire lifetime of the apparatus. An independent check of whether the oven needs a refill is to measure the atomic flux. A laser beam near the sodium D2 line is sent into the intermediate chamber perpendicular to the atomic beam, and a narrow resonant absorption of 3 - 5% corresponds to a good atomic flux for laser cooling and trapping.

In the end, a high density cloud in the magnetic trap is needed for the subsequent evaporative cooling. For us, several billion of trapped sodium atoms is a good starting point. To correctly estimate the atom number with such high density, an off-resonance imaging after a short time-of-flight is used, using the scaled absorption cross sections.

### **2.2.2 Evaporative cooling in a plugged magnetic-quadrupole trap**

After loading the atoms from the dark-spot MOT, the magnetic trap is ramped up to 750 G/cm for fast evaporation. While we are able to achieve the BEC in 8 seconds without trap decompression, we obtain a larger condensate of about  $5 \times 10^6$  atoms after reducing the trap gradient to 75 G/cm with further evaporation in the decompressed trap for an additional 3 seconds. The first BEC in the new apparatus was obtained in the magnetic trap and the corresponding radio-frequency evaporation sequence is illustrated in Fig. 2-3.

The plug beam initially came from a Spectra-Physics Millennia Xs (diode-pumped solid-state laser) with a full output of 9.5 W at 532 nm. This unit unfortunately failed later and was replaced with a similar unit but at a degraded output at 6 Watts. The plug beam is in a free-space setup, prepared on the bottom layer of the experimental table and then sent to the horizontal breadboard with a periscope. The plug has a waist around  $100 \mu m$ , and its position is controlled by motorized actuators (Newport TRA12CC) on the last mirror before the vacuum chamber for beam alignment. The motorized actuator is convenient in aligning the plug to the magnetic field zero point, however, there are always some unexplained fluctuations in the plug beam pointing. Preliminary investigation suggests that it is from the laser itself, and therefore could

be eliminated by coupling through a fiber, with an improvement in beam shape but a sacrifice in power.

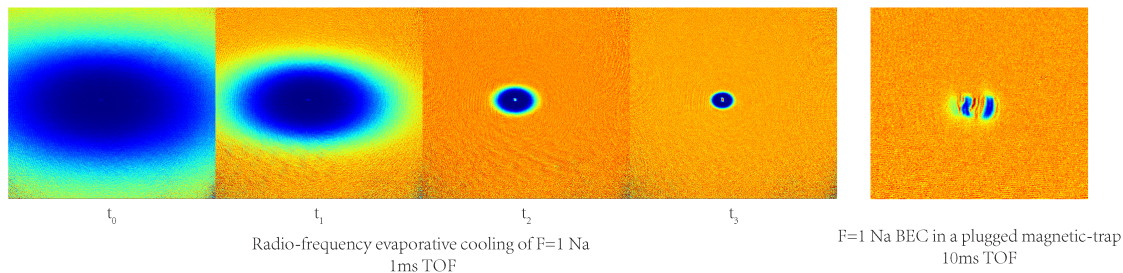


Figure 2-3: Evaporative cooling of sodium in the  $F = 1$  state with radio-frequency. From left to right are the images of the cloud at different stages in the evaporation after 1  $ms$  time-of-flight from a plugged quadrupole trap. A plugged hole can be seen at the center of the cloud. By the end of the evaporative cooling, a sodium condensate in the  $F = 1$  state emerges in the plugged magnetic trap, shown on the far right with a 10  $ms$  time-of-flight.

Forced evaporative cooling of the sodium typically occurs on either the microwave transition  $|1, -1\rangle \rightarrow |2, -2\rangle$ , or the radio-frequency (RF) transition  $|1, -1\rangle \rightarrow |1, 0\rangle$ . The RF evaporation is often easier to implement and has a better performance, but the strong RF radiation can interfere with the normal operation of electronic devices ranging from power supplies and motorized actuators to flow and temperature sensors. Since evaporation on the microwave transition near 1.7 GHz is necessary anyway for the sympathetic cooling of lithium, in which only sodium atoms are evaporated, it is used as our primary scheme for evaporative cooling.

We have an in-vacuum antenna that is connected via a 2-wire electrical feedthrough and designed mainly for driving RF hyperfine transitions. There is also an outside antenna mounted inside the top bucket, mainly for driving microwave hyperfine transitions. Both of them have a single loop copper wire design.

The results of the microwave and radio-frequency evaporation can be compared in Fig. 2-3 and Fig. 2-4. The final atom number at the end of the evaporation seems sensitive to the Rabi frequency of the transition. For our primary microwave evaporation, a 50W microwave amplifier (EMPOWER 1119) is located as close as possible and connected to the outside antenna by a short SMA cable to avoid unintended at-

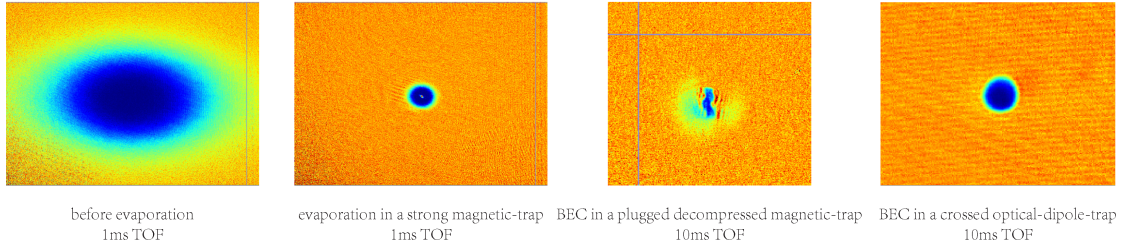


Figure 2-4: Evaporative cooling of sodium in the  $F = 1$  state with 1.7 GHz microwave. Evaporative cooling using microwave produces similar results as the case using radio-frequency. At the end, a sodium condensate in the  $F = 1$  state is produced in the plugged magnetic trap, and subsequently transferred into an optical dipole trap.

tenuation. Unfortunately, it's somewhat impractical to boost the microwave transfer and the Rabi frequency further, by either using a resonant circuit on the antenna since the evaporation frequencies are ranging from 1.4 GHz to 1.8 GHz, or switching to a horn antenna design because horn antenna at these frequencies gets very big and won't fit in the space.

### 2.2.3 BEC in an optical dipole trap

Even though we could get a BEC in the plugged magnetic trap, as almost all quantum simulation experiments are carried out in the optical dipole traps nowadays, efficiently transferring the atoms from the magnetic trap into a robust dipole trap is an essential landmark for our quantum gases sample preparation.

We decide to have a crossed dipole trap, because compared to a single-beam dipole trap, it doesn't require extremely focused beams and create elongated cloud. To save space on the optical table and minimize sloshing motion when ramping up the lattices, originally we intended to use LCD waveplates to switch the same beams between dipole traps and lattices. However, it turns out that, these nematic liquid crystal waveplates are typically controlled by amplitude-modulating a square wave at 5-20 kHz, which creates intrinsic intensity noise and heats up the cloud. If optical access permits, it is recommended to have separate lattice and ODT beams, decoupling the sample preparation from the subsequent experiments.

We've set up imaging along the optical dipole beams (as well as all lattice beams) to conveniently focus the beam at the cloud and achieve coarse alignment. For the fine alignment, atoms caught in each of the dipole beams are locating the beam position, and are used to align the beams to the magnetic trap center using in-trap imaging. The cloud lifetime in the crossed trap is sensitive to overlap between the dipole beams, and is maximized to fine tune their relative position. Finally, the plug beam could be slightly tweaked to maximize the transfer from the magnetic trap to the dipole trap.

Since there is always heating associated with the transfer into the dipole trap, we prefer to be more conservative near the end of evaporation in the magnetic trap, to be able to load more atoms into the ODT, and then perform further evaporation there. In practice, typically with dipole beams of 2 Watts in power each and of around 100  $\mu m$  waist, we are always able to catch a decent atom number in the dipole trap. The crossed ODT is then slowly ramped down to its half depth for evaporation, in order to create a pure BEC. The typical atom number of the condensate in our crossed dipole trap is about several million, good enough for most quantum simulation experiments. An example of the  $F = 1$  state BEC in the crossed dipole trap is shown in Fig. 2-4.

## 2.3 Sympathetic Cooling of ${}^6\text{Li}$ with ${}^{23}\text{Na}$ in the $F = 2$ State

Evaporative cooling would not work for a spin polarized Fermi gas, because the Pauli statistics strongly suppresses s-wave collisions and thermalization process at low temperature. The way to overcome this problems is to employ some form of sympathetic cooling between two distinguishable particles, which could be two spin states of the same atom, or two different isotopes of the same chemical element, or two different chemical elements. We continue the Ketterle lab tradition of using  ${}^{23}\text{Na}$  to cool  ${}^6\text{Li}$ , because the large number of sodium from the dark-spot MOT and the favorable collision properties between these two species have proved that the bosonic sodium is a great coolant for the fermionic lithium.

### 2.3.1 The hyperfine states of ${}^6\text{Li}$ and ${}^{23}\text{Na}$

The hyperfine structures of  ${}^{23}\text{Na}$  and  ${}^6\text{Li}$  are shown in Fig. 2-5. The hyperfine splitting of  ${}^{23}\text{Na}$  and  ${}^6\text{Li}$  is at 1.7 GHz and 228 MHz, respectively. The lowest two hyperfine states  $|1/2, -1/2\rangle$  and  $|1/2, 1/2\rangle$  of  ${}^6\text{Li}$  are usually used as spin up and spin down in a two-component Fermi gas experiment. In the previous section, we have demonstrated the Bose-Einstein condensation in  $|1, -1\rangle$  state of the  ${}^{23}\text{Na}$   $F = 1$  hyperfine manifold.

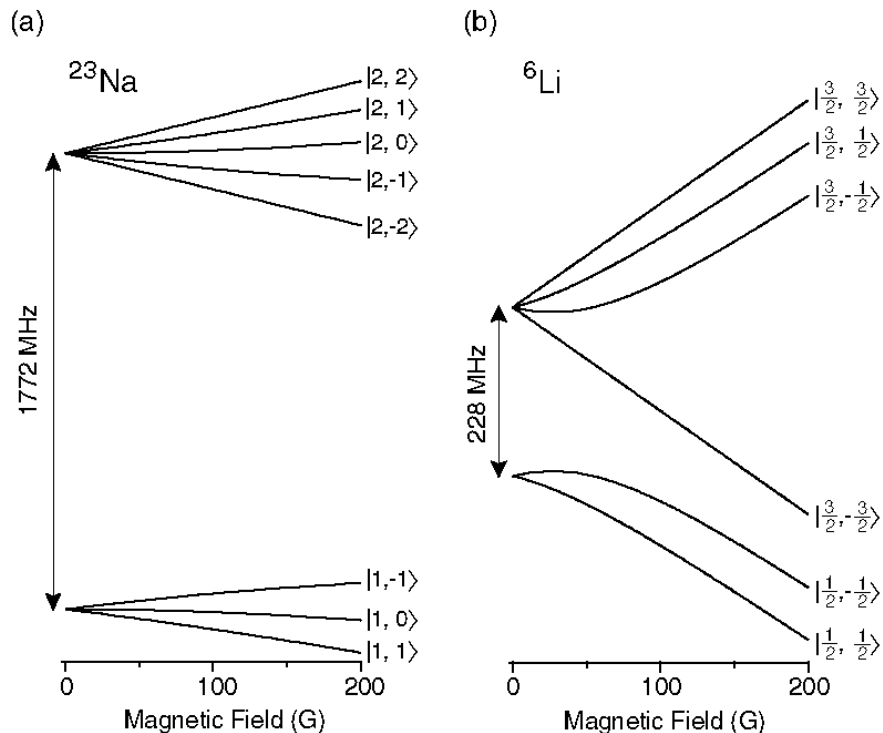


Figure 2-5: The hyperfine structures of  ${}^{23}\text{Na}$  and  ${}^6\text{Li}$ . The hyperfine states are labeled in their low-field  $|F, m_F\rangle$  basis. In the previous section, sodium was cooled to BEC in the  $|1, -1\rangle$  lower hyperfine state. In this section, to sympathetically cool lithium, the combination of lithium in  $|3/2, 3/2\rangle$  and sodium in  $|2, 2\rangle$  states is used, because both states are magnetically trappable and stable against spin-exchange collisions. This figure is adapted from [2].

Among these hyperfine states, the combinations of  ${}^{23}\text{Na}$  and  ${}^6\text{Li}$  that are both magnetic trappable and stable against spin exchange collisions are  $|1, -1\rangle + |1/2, -1/2\rangle$  and  $|2, 2\rangle + |3/2, 3/2\rangle$ . Earlier studies [2] have shown that the latter produce the best results in sympathetic cooling of sodium and lithium, and is used in our experiment

to achieve a quantum degenerate Fermi gas.

### 2.3.2 Condensation of $^{23}\text{Na}$ in the $F = 2$ hyperfine state

Most sodium atoms in a dark-spot MOT are in  $|1, -1\rangle$  state. To sympathetically cool lithium, we need to first transfer the sodium atoms from  $|1, -1\rangle$  state to  $|2, 2\rangle$  state, and then evaporatively cool  $|2, 2\rangle$  state sodium with 1.7 GHz microwave radiation.

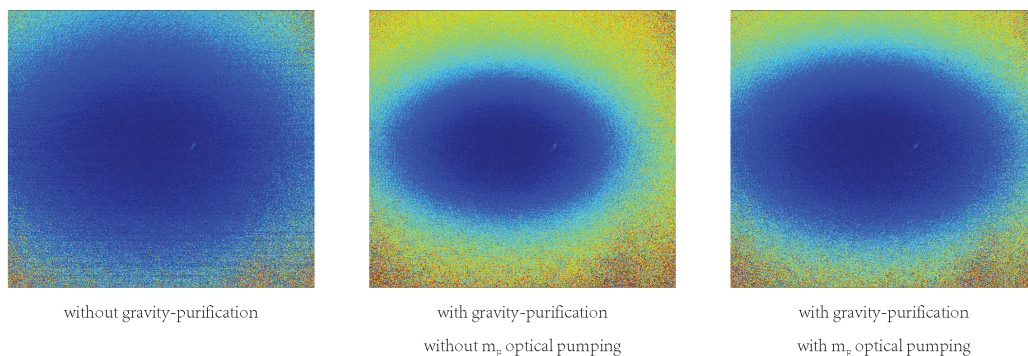


Figure 2-6: Gravity-assisted spin purification and optical pumping of sodium into the  $F = 2$  upper hyperfine state. An additional stage of  $m_F$  optical pumping at  $F = 2$  hyperfine states boosts the transfer efficiency by about 20 percent. Gravity-assisted spin purification removes the unwanted  $|F = 2, m_F = 0, 1\rangle$  states, preventing inelastic spin-exchange collisions and consequent heating.

The transfer from  $F = 1$  to  $F = 2$  states in sodium is achieved by optical pumping. The  $\sigma^+$  polarized light couples the  $F = 1$  states into the excited states, and then the atoms partially decay into the  $F = 2$  states in spontaneous emission. To optical pump the atoms onto the preferred Zeeman state  $|2, 2\rangle$  and improve the pumping efficiency, an  $m_F$  pumping with  $\sigma^+$  polarized light at  $F = 2 \rightarrow F' = 2$  transition is applied to make  $|2, 2\rangle$  a dark state and avoid unnecessary heating of the cloud. This additional  $m_F$  optical pumping boosted the transfer efficiency into the correct Zeeman state by more than 20 percent, illustrated in Fig.2-6.

Atoms in the other Zeeman sub-levels  $|F = 2, m_F = 0, 1\rangle$  of  $F = 2$  hyperfine states are susceptible to spin exchange collisions and consequent heating, and need to be removed from the trap before evaporation. Traditionally with an Ioffe-Pritchard trap,

this is accomplished by applying a bias field to split the  $F = 2$  Zeeman sub-levels, and then selectively transferring these unwanted states into untrapped  $|F = 1, mF = 0, 1\rangle$  lower hyperfine states using microwave transitions. In our new apparatus with the quadrupole magnetic trap, we've developed a new gravity-assisted spin purification scheme, demonstrated in Fig. 2-6. This method uses the fact that the Zeeman states have different magnetic moments, and therefore experience different trapping forces in the magnetic trap. As we lower the trap, magnetic force is not able to hold up the atoms against gravity in the unwanted states  $|F = 2, mF = 0, 1\rangle$ , and therefore only atoms in  $|F = 2, mF = 2\rangle$  are preserved in the end.

Finally, the microwave evaporation in the  $F = 2$  state is fairly similar to the case of  $F = 1$ , except that the microwave frequency is ramped down, instead of being ramped up. The three-body collision loss rate is a bit higher for  $F = 2$  states compared with  $F = 1$  states, and therefore the magnetic trap needs to be decompressed earlier before further evaporation. The evaporation sequence is empirically chosen to optimize the final atom number in the condensate.

### 2.3.3 Sympathetic cooling of ${}^6\text{Li}$ with ${}^{23}\text{Na}$

While there were major upgrades on the sodium table and infra-red setup, the lithium table was almost kept the same. Most efforts were made to improve the temperature stability, by moving the hot lithium cell onto a separate breadboard outside the main table, and by building small enclosures to confine the air circulation. In addition, a New Focus Vortex II tunable laser (TLB-6900) was bought and phase locked to the main laser. This laser has a total output of 15 mW and a large mode-hop free tuning range ( $>120$  GHz), perfect for the lithium high-field imaging near the Feshbach resonance.

In making a lithium MOT in our new apparatus, a tapered amplifier was added to boost the slower light power and the MOT loading. In order to optimize the Zeeman slower for a sodium-lithium dual-species MOT, first the current in its last section is tweaked for the sodium MOT, and then the lithium slower frequency is scanned to find its optimal value for the lithium MOT. Currently with things tweaked and optimized,

we have a good performing dual-species MOT. However, future generation is advised to consider adding tapered amplifier to the MOT/repump light for compensating the larger beam sizes in our new MOT system.

During the transfer from dual-species MOT into magnetic trap, we also optically pump  ${}^6\text{Li}$  into the stretched  $|3/2, 3/2\rangle$  state. Again, two  $\sigma^+$  polarized laser beams are used, resonant with the transitions from  $F = 1/2$  and  $3/2$  ground states. In case of  ${}^6\text{Li}$ , the excited states are not resolved, so the discussion of the dark state during the optical pumping in  ${}^{23}\text{Na}$  does not arise here. The optical pumping performance can be checked by imaging the  $F = 1/2$  and  $3/2$  state population independently. The gravity-assisted spin purification method doesn't work for lithium when both species are loaded in the magnetic trap, due to the much lighter weight of the lithium atoms. One could first load lithium alone and purify its spin states in the magnetic trap, and then load the sodium subsequently. However, we find this procedure too cumbersome and in practice unnecessary.

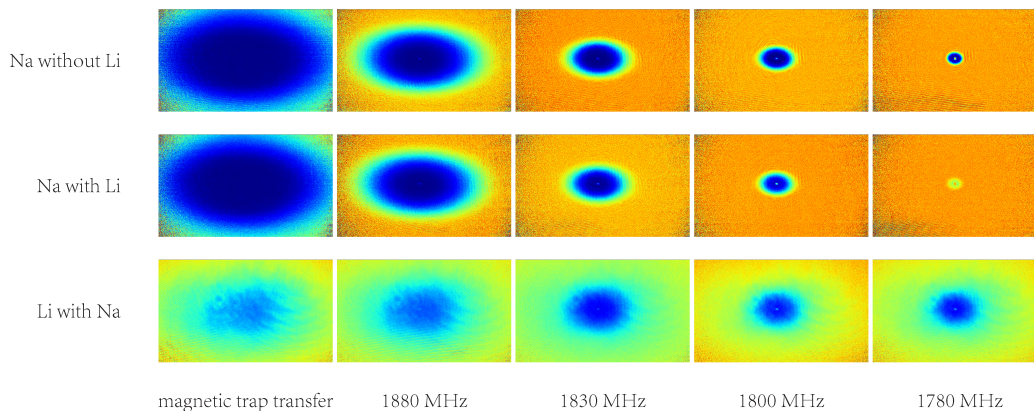


Figure 2-7: The sympathetic cooling of lithium with sodium in the  $F = 2$  state. The lithium cloud shows a decreased temperature as we evaporate the sodium. However, with a fully loaded MOT, the lithium gas doesn't reach the deep quantum degeneracy even when all sodium atoms are evaporated.

This is pretty much all we have to do. At this point, we simply evaporate sodium the same way as in Section 2.3.2. The sympathetic cooling of lithium is observed in Fig. 2-7, as we evaporate sodium, the temperature of the lithium cloud also decreases.

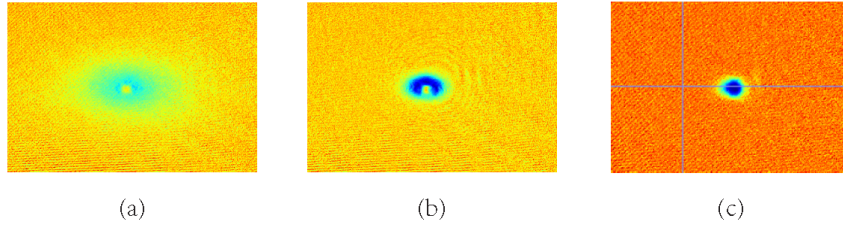


Figure 2-8: The efficiency of the sympathetic cooling. The two images on the left show the lithium cloud at the end of sympathetic cooling with initially (a) more lithium atoms or (b) fewer lithium atoms loaded into the magnetic trap. Image (c) shows a lithium cloud loaded into the optical dipole trap after the sympathetic cooling.

However, it seems that for a fully loaded lithium MOT, we are not able to reach the quantum degeneracy of lithium even when all the sodium atoms are evaporated. To trade in the  ${}^6\text{Li}$  atom number for deeper quantum degeneracy, we deliberately switch on the lithium slower light only at the end of the MOT loading. This tradeoff turned out to be quite favorable, as we were able to get a very cold lithium cloud after the sympathetic cooling in the magnetic trap, and subsequently loading it into the optical dipole trap created a quantum degenerate Fermi gas of  ${}^6\text{Li}$ , shown in Fig. 2-8.

## 2.4 Hyperfine State Preparation of ${}^{23}\text{Na}$

In the final section, I'll describe how we use microwave and radio-frequency radiations to drive transitions between the hyperfine states in sodium. These experiments are performed in order to benchmark the performance of our antennas by measuring the corresponding Rabi frequencies, as well as to develop the required techniques for state preparation in future experiments, such as a spin mixture of lithium  $|1/2, -1/2\rangle$  and  $|1/2, 1/2\rangle$  states in strongly interacting Fermi gases, or a pure sodium condensate in the stretched  $|2, \pm 2\rangle$  state for the synthetic gauge field experiments in the optical lattices, where very homogeneous tilts are created by applying a magnetic field gradient across the cloud. Finally, two-photon transitions are also demonstrated in the  $F = 1$  to  $F = 2$  transition in sodium, as it has been proved to be a powerful way to measure the filling number in the Mott insulator state [14].

### 2.4.1 Microwave transitions between hyperfine states

Landau-Zener transition is a powerful method to prepare spin mixture states in quantum gases. In the first experiment, we have performed a Landau-Zener sweep between  $F = 1$  and  $F = 2$  hyperfine states in sodium, shown in Fig. 2-9. A weak bias magnetic field is turned on to split the Zeeman sub-levels, and the microwave radiation centered at 1762.9 MHz is linearly swept over 0.3 MHz in 10 milliseconds, slow enough to keep the sodium atoms following the adiabatic passage. In the first one-way sweep, almost all sodium atoms flip to the other hyperfine states, and the second return-trip sweep confirms that this process is fully reversible and does not create much heating.

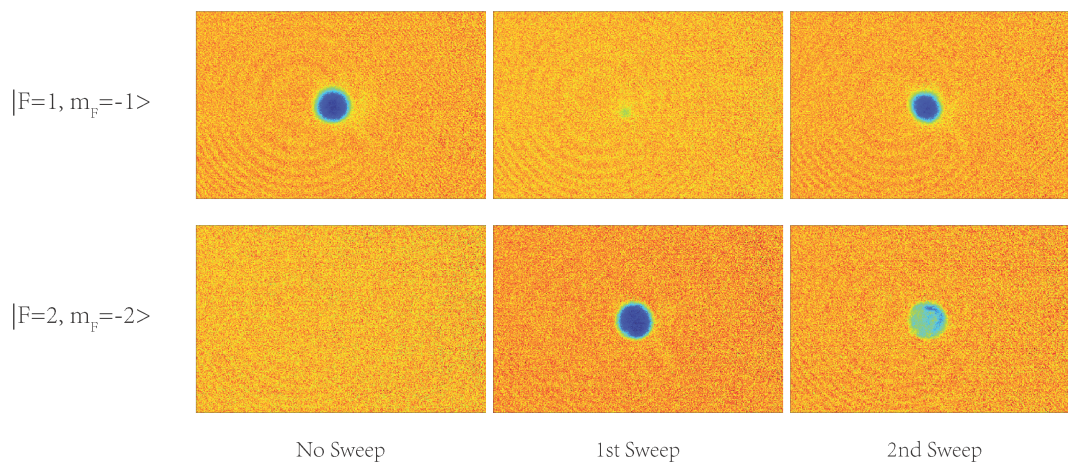


Figure 2-9: Spin flips between sodium  $F = 1$  and  $F = 2$  hyperfine states via Landau-Zener transition with microwave radiations around 1.763 GHz. The transfer efficiency is close to unity shown in the single sweep, and this process is reversible without much heating demonstrated in the double sweep.

In the second experiment, we drive the microwave transition on resonance to make coherent transfer in the Rabi oscillation between  $F = 1$  and  $F = 2$  hyperfine states. Again, a weak bias field is applied to split the Zeeman sub-levels, before the microwave pulse is switched on at the resonance frequency for a variable time. The population in the initial and final state can be measured independently, and are shown as a function of the microwave pulse time in Fig. 2-10. A full Rabi oscillation was observed, and the Rabi frequency of this microwave transition is estimated to be around 4 kHz.

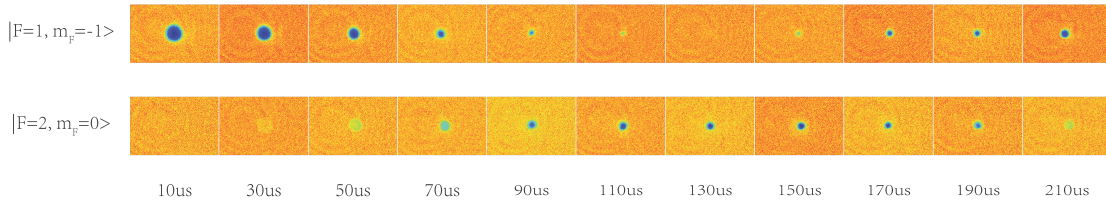


Figure 2-10: Rabi oscillations in the microwave transition between  $|1, -1\rangle$  and  $|2, 0\rangle$  hyperfine states. A weak bias field is switched on to split the Zeeman sub-levels, and a microwave radiation pulse at the resonance frequency of 1768.738 MHz is applied to the sodium condensate in the dipole trap for a variable duration. These images show an resonant Rabi oscillation at the estimated Rabi frequency of about 4 kHz.

## 2.4.2 Radio-frequency transitions between hyperfine states

Similarly, radio-frequency can be used to drive transitions between Zeeman sub-levels in the hyperfine states. For  $F = 1$  hyperfine state in sodium, there are three Zeeman sub-levels  $|F = 1, mF = 0, \pm 1\rangle$ . However, the selection rules predict that there is no direct one-photon transition between the  $|1, -1\rangle$  and  $|1, 1\rangle$  states.

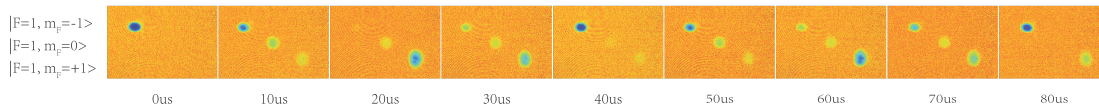


Figure 2-11: Spin flips between  $F = 1$  hyperfine states with radio-frequency radiations and the Stern-Gerlach experiment. A radio-frequency pulse at 2.933 MHz is switched on for a variable time to drive the two-photon transition between  $|1, -1\rangle$  and  $|1, 1\rangle$ . A magnetic field gradient is rapidly switched on during the time-of-flight to separate the Zeeman sub-levels and perform a Stern-Gerlach experiment to read out the population in each hyperfine state. These images show an estimated Rabi frequency of 25 kHz.

To drive the RF transition, again a weak bias field is turned on to split the Zeeman sub-levels. The hyperfine coupling in  $^{23}\text{Na}$  is so strong that, this bias field is far inside the low field regime of the Breit-Rabi problem, and therefore these three Zeeman sub-levels have linear Zeeman shifts and are equally spaced. We drive this RF transition at the resonance frequency of 2.933 MHz for a variable time. Due to the linear Zeeman shifts, effectively all three states are coupled, and a way to selectively read out each state is needed. In contrast to the microwave transition, this splitting is much smaller

than the sodium natural linewidth of 9.8 MHz, and thus cannot be resolved optically. Instead, we perform a Stern-Gerlach type experiment, where a strong magnetic field gradient is suddenly switched on during the time-of-flight to spatially separate these Zeeman sub-levels, and a single absorption image is taken to measure the population in each state, as demonstrated in Fig. 2-11. The measured Rabi frequency for the RF transitions is about 25 kHz in our system.

### 2.4.3 Two-photon transitions between hyperfine states

Finally, we perform a two-photon transition between the  $F = 1$  and  $F = 2$  hyperfine states in sodium. This is relevant because the two-photon techniques can be applied to the clock transition, which is between  $|1, -1\rangle$  to  $|2, 1\rangle$  states in sodium, to measure the filling number in a Mott insulator [14]. This transition is called the clock transition, because both the initial and final states have the same first-order Zeeman shift, and therefore it is widely used in atomic clocks to avoid the Zeeman shifts and broadening from magnetic field fluctuations.

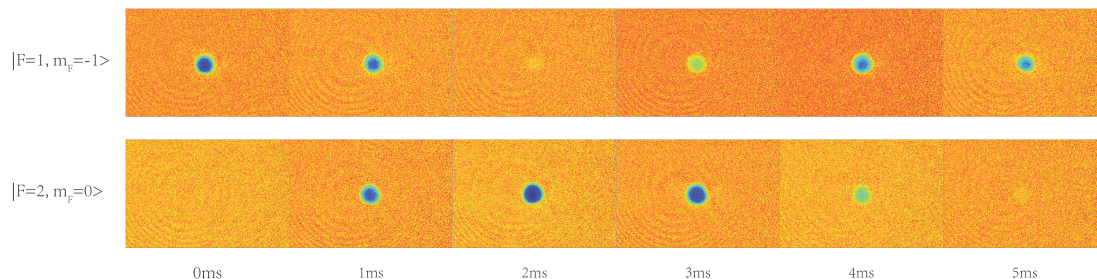


Figure 2-12: Two-photon Rabi oscillations between  $F = 1$  and  $F = 2$  hyperfine states in sodium. The two-photon coupling is provided by 1.77 GHz microwave photons and 2.4 MHz radio-frequency photons. The observed resonant Rabi oscillations indicate a two-photon Rabi frequency of about 200 Hz.

In Fig. 2-12, we have shown the Rabi oscillation of a two-photon transition between the  $|1, -1\rangle$  to  $|2, 0\rangle$  states in sodium. The final state is identified by the relative position of the nearby resonances. This two-photon coupling is provided by a microwave at 1769.237 MHz and a radio-frequency at 2.408 MHz. The resonant Rabi frequency of the two-photon transition is measured to be around 200 Hz.

# Chapter 3

## Bose-Einstein Condensates in Optical Lattices

### 3.1 Introduction

Quantum simulation using ultracold gases in the optical lattices has become an very active field in the past decade. This system has not only been demonstrated as a great platform for testing fundamental concepts in quantum physics, but also has promised a set of novel Hamiltonians that are far beyond the reach of other systems. The early success of quantum simulations has also attracted a lot of interests from other fields of physics in condensed matter and high energy communities, as it has proved itself a powerful tool to tackle some long-standing unsolved problems in physics.

The field of quantum simulation in optical lattices has become very diverse lately. However to me, the progress of the mainstream and the milestones in this field can be divided into roughly speaking three phases. The first phase is focused on the behavior of the condensates in optical lattices, from the first experimental observation of the quantum phase transition from a superfluid to a Mott insulator from the interference peaks during time-of-flight [15], to the recent microscopic studies of this phase transition using single-site resolution imaging [16, 17], and thorough characterization of the quantum criticality near the transition [18]. The second phase is regarding fermions in optical lattices, including the experimental observation of fermionic superfluidity [3],

band insulator and Mott insulator [19, 20], and most recent efforts towards probing the anti-ferromagnetic state in a Fermi-Hubbard model [21, 22]. In the past five years or so, there has been a wave of research works on bringing gauge fields into the system with complex tunnelings [23, 24, 25, 26], and simulating novel Hamiltonians with topological properties [27, 28]. These exciting progresses have opened up a whole new phase of quantum simulations in optical lattices.

During the design and construction of our new apparatus, the goal we envisioned initially was to observe the antiferromagnetic ordering in the Fermi-Hubbard model. However, another opportunity later arose, as a novel scheme for implementing synthetic gauge fields became available. A different lab in our group working with  $^{87}\text{Rb}$  was in the process of implementing this scheme, but they observed anomalous heating that had prevented them from reaching the ground state of the Harper Hamiltonian. It appeared that the fast tunneling of sodium and the ease of making large magnetic gradients in our apparatus might be the solution to solve this heating problem. These thoughts have led to an extended study of the relationship between interactions and the Bloch oscillations described at the end of this chapter. Now the rubidium lab have found strong evidence of observing the ground state of the Harper Hamiltonian [26], we have largely turned our focus towards implementing spin-orbit coupling in superlattices and synthetic gauge fields with fermions, presented in the next chapter.

In this chapter, we will first introduce the basic picture and concepts of the physics in optical lattices. Then we experimentally demonstrate the quantum phase transition from a superfluid to a Mott insulator, as a way to characterize our new optical lattice system. Finally, we will describe our experiments of making very strong tilts in an one-dimensional optical lattice to drive the Bloch oscillations, as well as our studies on the interaction effects in the Bloch oscillations, such as dynamical instability and relaxation in the quasi-momentum states. All of these studies pave the road to a new implementation of spin-orbit coupling in a superlattice described in the next chapter.

## 3.2 Basic Lattice Physics

In general, the Hamiltonian of a quantum gas consists of a single-particle term and an interaction term,

$$H = H_0 + H_{int} \quad (3.1)$$

Let us start with the single-particle Hamiltonian, which includes the kinetic energy  $-\hbar^2\nabla^2/2m$  and the external potential  $V(r)$ . In solid-state systems, the external potential is usually from the static electric field of crystalline ions. In an optical lattice system, the external potential is from the AC-Stark shift via photon-atom interaction, and consists of two parts

$$H_0 = -\hbar^2\nabla^2/2m + V_L(r) + V_T(r) = H_{0L} + V_T(r) \quad (3.2)$$

the former  $V_L(r)$  is a periodic lattice potential created by the standing wave, while the latter  $V_T(r)$  is any additional potential, for example, the harmonic confinement from optical dipole traps. As the extra potential is often slowly-varying compared to the optical lattices, one can make the assumption that it is constant locally and first study  $H_{0L}$  in a homogeneous setting, and then consider the inhomogeneous effects of  $V_T(r)$  with a local chemical potential  $\mu(r) = \mu - V_T(r)$  in the local density approximation (LDA).

### 3.2.1 Band structure and Bloch states

In this section, we include a solid-state textbook calculation of the band structure in an one-dimensional optical lattice. The more general question can be raised as, how do we solve the eigen-problem for a periodic potential?

The eigen-states of an optical lattice, also known as the Bloch states  $\phi_{\mathbf{k}}^n(r)$  (with band index  $n$  and quasi-momentum  $\mathbf{k}$ ), need to satisfy

$$H_{0L}|\phi_{\mathbf{k}}^n(r)\rangle = \varepsilon_{\mathbf{k}}^n|\phi_{\mathbf{k}}^n(r)\rangle \quad (3.3)$$

where  $\phi_{\mathbf{k}}^n(r) = e^{i\mathbf{k}\cdot\mathbf{r}}u_{\mathbf{k}}^n(r)$  and  $u_{\mathbf{k}}^n(r)$  has the same periodicity as the lattice by Bloch's theorem.

One needs to diagonalize the Hamiltonian to find the eigen-states. In the basis of plane waves, the kinetic energy term is diagonal. A key observation is that, for the case of a sinusoidal potential, only plane waves with momentum shift  $\pm 2k_L$  are coupled. This dramatically reduces the size of the Hilbert space we need to consider. Finally, the eigenvalues of the Hamiltonian tell us the band structure, and superposition of the plane waves weighted by the eigenstates give us the Bloch states.

For the rest of this section, we'll walk through some details of this calculation. First of all, since  $u_{\mathbf{k}}^n(r)$  has the same periodicity of the lattice, one can expand  $u_{\mathbf{k}}^n(r)$  in its Fourier components,

$$u_{\mathbf{k}}^n(r) = \frac{1}{\sqrt{\Omega}} \sum_G a_{\mathbf{k}}^n(G) e^{iG\cdot r} \quad (3.4)$$

substitute  $\phi_{\mathbf{k}}^n(r)$  with the Fourier expansion into the eigen-problem,

$$H_{0L} \sum_G a_{\mathbf{k}}^n(G) \frac{e^{i(G+k)\cdot r}}{\sqrt{\Omega}} = \varepsilon_{\mathbf{k}}^n \sum_G a_{\mathbf{k}}^n(G) \frac{e^{i(G+k)\cdot r}}{\sqrt{\Omega}} \quad (3.5)$$

We convert the equations into a matrix form by multiplying  $e^{-i(G'+k)\cdot r}/\sqrt{\Omega}$  on both sides and applying integration over space,

$$\sum_G a_{\mathbf{k}}^n(G) H_{G',G} = \sum_G a_{\mathbf{k}}^n(G) \varepsilon_{\mathbf{k}}^n \delta_{G',G} \quad (3.6)$$

with matrix element of the Hamiltonian

$$H_{G',G} = \frac{1}{\Omega} \int e^{-i(G'+k)\cdot r} \left( -\frac{\hbar^2}{2m} \nabla^2 \right) e^{i(G+k)\cdot r} dr + \frac{1}{\Omega} \int e^{-i(G'+k)\cdot r} V_L e^{i(G+k)\cdot r} dr \quad (3.7)$$

The first term is non-vanishing only when  $G' = G$ , meaning that the kinetic energy is diagonal in momentum. The second term corresponds to an optical-lattice potential  $V = V_0 \sin^2(k_L r)$ , which only couples plane waves with  $G' = G \pm 2k_L$ , in addition to

an overall energy offset.

$$H_{G',G} = \frac{\hbar^2}{2m}|G+k|^2\delta_{G,G'} + \frac{V_0}{2}\delta_{G,G'} - \frac{V_0}{4}(\delta_{G+2k_L,G'} + \delta_{G-2k_L,G'}) \quad (3.8)$$

In summary, the single-particle Hamiltonian in an optical lattice in the basis of plane waves is written as

$$H(k) = \begin{pmatrix} \dots & \dots & & & & & \\ \dots & \frac{\hbar^2}{2m}|k-2k_L|^2 + V_0/2 & & -V_0/4 & & & \\ & & -V_0/4 & & \frac{\hbar^2}{2m}|k|^2 + V_0/2 & & -V_0/4 \\ & & & -V_0/4 & & \frac{\hbar^2}{2m}|k+2k_L|^2 + V_0/2 & \dots \\ & & & & & & \dots \\ & & & & & & \dots \end{pmatrix} \quad (3.9)$$

For actual numerical calculation, one needs to cut off this infinite matrix at a certain size, because couplings into those high momentum states are far detuned and thus negligible. With efficient commercial matrix eigen-solver from Matlab or Mathematica, one finds the band structure and the corresponding Bloch states.

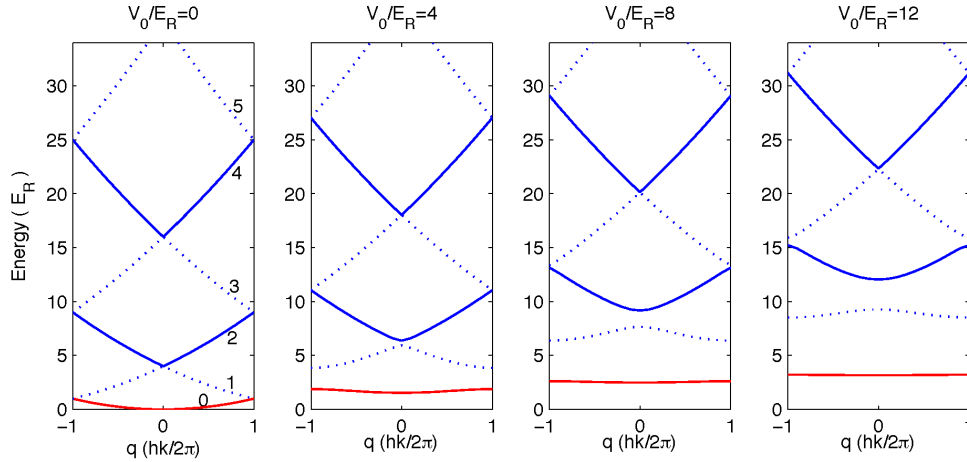


Figure 3-1: The band structures of a one-dimensional lattice are plotted for lattice depths between  $0E_R$  and  $12E_R$ . Even bands are shown in solid lines, odd bands are shown in dotted lines, and the lowest band is shown in red. As the lattice gets deeper, the lowest band becomes flat and the band gap becomes large.

In Fig. 3-1 and 3-2, we've plotted the Bloch bands for various lattice depths, and

the Bloch states at the center and the edge of the Brillouin zone.

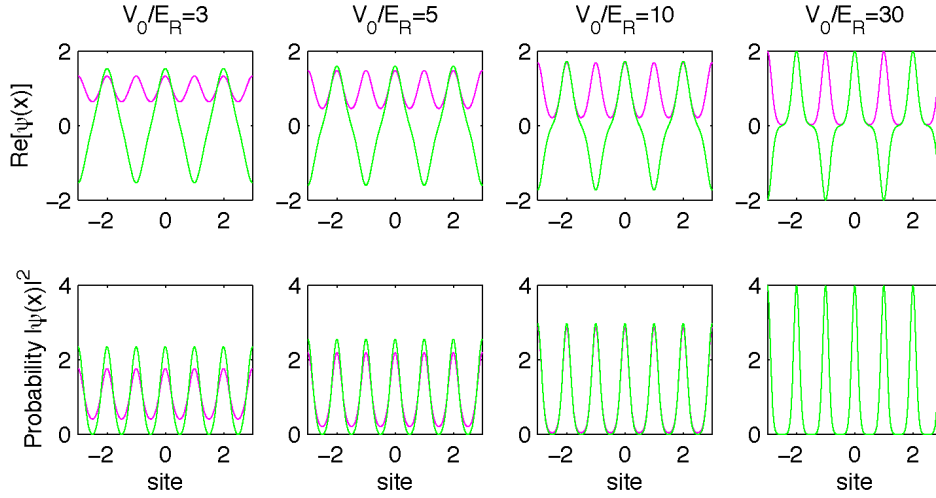


Figure 3-2: The real part and probability (absolute-value squared) of Bloch states  $\phi_{\mathbf{q}}(r)$  with quasi-momentum  $\mathbf{q} = 0$  (in purple) and  $\mathbf{q} = \hbar k_L$  (in green) in the lowest band, for a one-dimensional lattice with depths of  $V_0/E_R=3, 5, 10$  and  $30$ , respectively.

### 3.2.2 Tight binding and Wannier states

To study the physics of localized particles, such as superfluid to Mott insulator phase transition and quantum magnetism in optical lattices, it is often more convenient to consider the tight binding limit and use a set of localized states, the so-called Wannier states.

It's worth mentioning that Bloch states and Wannier states are both complete orthonormal basis for the single-particle Hilbert space, as the field operator can be decomposed as

$$\psi_{\sigma}^{\dagger}(r) = \sum_{i,n} w_n^*(r - R_i) c_{in\sigma}^{\dagger} = \sum_{\mathbf{k},n} \phi_{\mathbf{k}}^n(r) c_{\mathbf{k}n\sigma}^{\dagger} \quad (3.10)$$

The difference is that Bloch states describe the itinerant behavior in the metallic or superfluid phase, while Wannier states features localization in the insulator phase. This is in analogy to the wave-particle duality in quantum physics, in which the wave representation and the particle representation complement each other.

One can construct a set of Wannier states  $w_{\mathbf{R}_i}^n(r) = w_n(r - R_i)$ , which are localized at every lattice site  $\mathbf{R}_i$ , using linear combinations of the Bloch states in the same band,

$$w_{\mathbf{R}_i}^n(r) = w_n(r - R_i) = \frac{1}{\sqrt{N}} \sum_{\mathbf{k}} e^{-i\mathbf{k}\cdot\mathbf{R}_i} \phi_{\mathbf{k}}^n(r) = \frac{1}{\sqrt{N}} \sum_{\mathbf{k}} e^{i\mathbf{k}\cdot(\mathbf{r}-\mathbf{R}_i)} u_{\mathbf{k}}^n(r) \quad (3.11)$$

One caveat here is that, there are actually many different ways of choosing the linear combinations, namely the relative phases of the Bloch states in the superposition. The consensus regarding this procedure is to choose the superposition that gives the maximally-localized Wannier states.

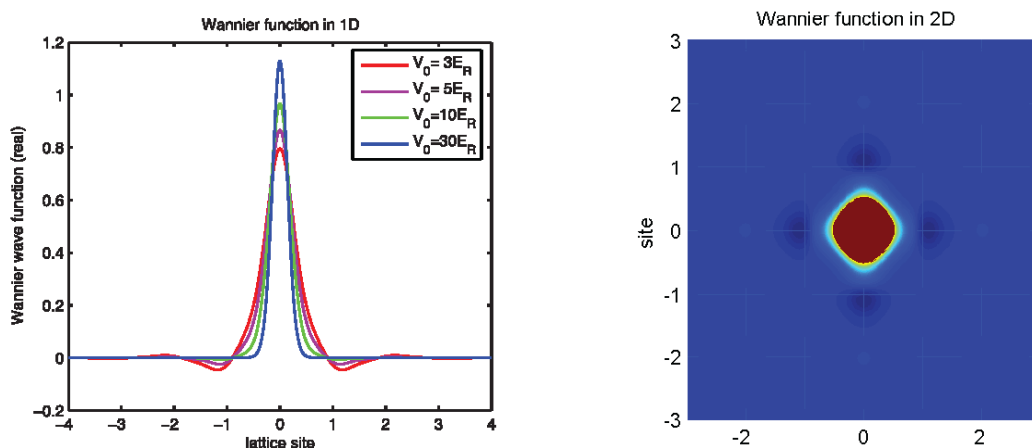


Figure 3-3: The Wannier states in the lowest band. The left figure plots the Wannier states in a one-dimensional lattice for various lattice depths, whereas the right figure plots the Wannier state in a two-dimensional square lattice with equal strength  $V_0 = 10E_R$ . Both figures show that Wannier states have secondary maxima at the nearest-neighbors, which provide tunneling between them.

In Fig. 3-3, we plot the Wannier states in one-dimensional and two-dimensional lattices. Each of them is mainly localized in a single lattice site, and has a small overlap with its nearest-neighbors. This overlap is responsible for the amplitude of nearest-neighbor tunneling.

Second quantization of the single-particle Hamiltonian in the Wannier basis gives

$$H_{0L} = \sum_{\sigma} \int dr \psi_{\sigma}^{\dagger}(r) [-\hbar^2 \nabla^2 / 2m + V_L(r)] \psi_{\sigma}(r) \quad (3.12)$$

$$= \sum_{\mathbf{k}, n, \sigma} \epsilon_{\mathbf{k}, n} c_{\mathbf{k}n\sigma}^{\dagger} c_{\mathbf{k}n\sigma} = \sum_{i, n, \sigma} \epsilon_{n0} c_{in\sigma}^{\dagger} c_{in\sigma} - \sum_{n\sigma} \sum_{ij} t_{ij}^n c_{in\sigma}^{\dagger} c_{jn\sigma} \quad (3.13)$$

with the tunneling amplitude and onsite single-particle energies given by

$$t_{ij}^n = - \int dr w_n^*(r - R_i) [-\hbar^2 \nabla^2 / 2m + V_L(r)] w_n(r - R_j) = - \sum_{\mathbf{k}} e^{i\mathbf{k} \cdot (\mathbf{R}_i - \mathbf{R}_j)} \epsilon_{\mathbf{k}, n} \quad (3.14)$$

$$\epsilon_{n0} = \sum_{\mathbf{k}} \epsilon_{\mathbf{k}, n} \quad (3.15)$$

There are a few comments to be made about this derivation. First of all, because the Wannier states are superposition of Bloch states in the same band, the Hamiltonian does not couple Wannier states in different bands and thus there is no interband tunneling. Furthermore, for separable optical lattices in higher dimensions, for example a cubic lattice, tunneling is non-vanishing only along the principle axes. In other words, there is no tunneling along diagonal directions.

For deep lattices, Wannier states are well localized and their amplitude goes very small after a couple of lattice constants. Deep lattices also exhibit large band gaps, and low-temperature quantum gases usually only populate the lowest band. Therefore, we will only keep the nearest-neighbor tunneling in the lowest-band. The single-particle Hamiltonian in the single-band Wannier states simply reads

$$H_{0L} = \sum_{i, \sigma} \epsilon_0 c_{i\sigma}^{\dagger} c_{i\sigma} - \sum_{\sigma} \sum_{\langle ij \rangle} t c_{i\sigma}^{\dagger} c_{j\sigma} \quad (3.16)$$

where  $\langle ij \rangle$  includes all nearest-neighbors  $i$  and  $j$ , and the nearest-neighbor tunneling amplitude in the lowest band is

$$t = - \int dr w_1^*(r - R_i) [-\hbar^2 \nabla^2 / 2m + V_L(r)] w_1(r - R_j) = - \sum_{\mathbf{k}} e^{i\mathbf{k} \cdot (\mathbf{R}_i - \mathbf{R}_j)} \epsilon_{\mathbf{k}, 1} \quad (3.17)$$

### 3.2.3 Lattice calibration via Kapitza-Dirac diffraction

The depth of an optical lattice in principle can be calculated based on the power and waist of the beam. Nonetheless, there are often practical imperfections from the overlap and polarization, and the atoms themselves are always the best probe of the lattice depth.

The depths of optical lattices are routinely calibrated in our lab via Kapitza-Dirac diffraction. During the experiment, a very short pulse of optical lattice is applied to a condensate, and then after a few milliseconds of time-of-flight, the diffraction pattern is recorded to analyze the strength of the optical lattice potential.

When the short pulse is diabatically switched on, the initial zero-momentum state is projected onto the zero-quasimomentum states in each band of the lattice, which evolve at different energies during the pulse. The zero-quasimomentum state at each band has different contributions from  $\pm 2\hbar k_L$ ,  $\pm 4\hbar k_L$ , and higher momentum components. As time evolves, these states in different bands become in and out of phase, and this results in oscillations in the diffraction pattern.

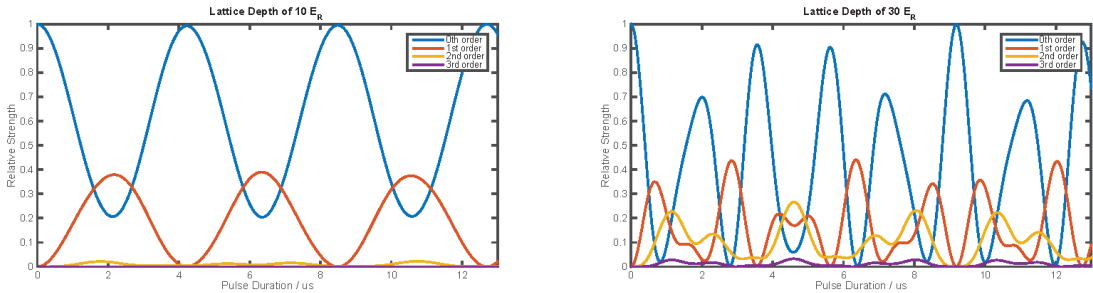


Figure 3-4: Kapitza-Dirac diffraction for a shallow lattice at  $10E_R$  and a deep lattice at  $30E_R$ . The time evolution of the relative strength of the diffraction peaks are shown for 532 nm lattices.

Fig. 3-4 shows different time-evolution of the diffraction patterns for a shallow lattice and a deep lattice. For shallow lattices, only the ground and first excited band are populated, and the diffraction pattern shows oscillations at the band gap frequency. For deep lattices, more momentum states are excited, the time-dependence becomes more complicated, and experimental data are usually more difficult to fit.

In practice, the number of visible peaks in the Kapitza-Dirac diffraction gives a reliable rough estimate of the lattice depth. Precision calibration is usually performed first with a shallow lattice by extracting the oscillation period, and then the depth of a deep lattice is extrapolated by scaling the optical power. For example, Fig. 3-5 shows an experimental calibration of our 532 nm lattice. An oscillation at about  $4 \mu\text{s}$  in the diffraction pattern gives an estimate of  $10E_R$  in green, corresponding to the left plot in Fig. 3-4. Careful calibration is done by fitting the diffraction pattern as a function of time and matching the time evolution at a certain lattice depth.

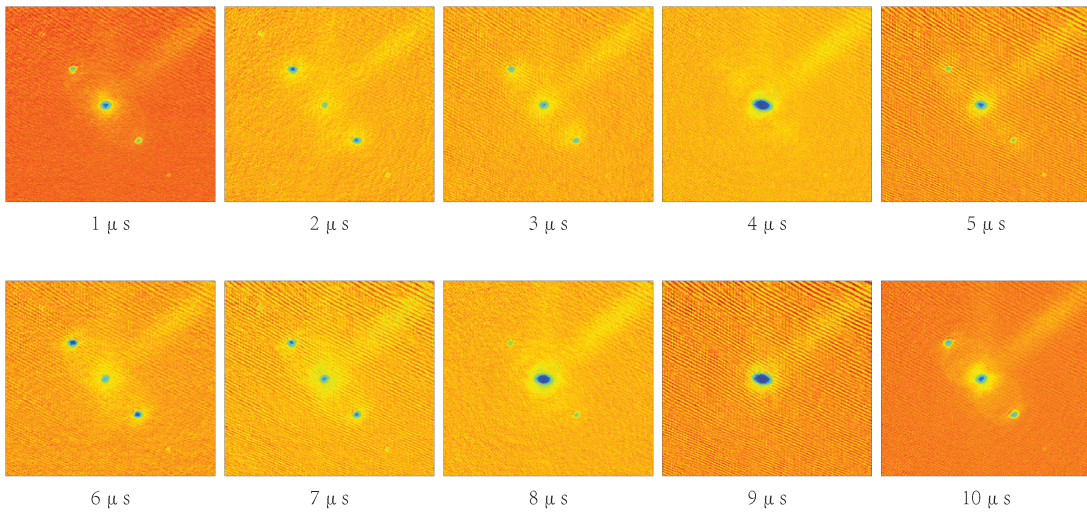


Figure 3-5: Kapitza-Dirac diffraction for various pulse durations in a 532 nm optical lattice. An oscillation period around  $4 \mu\text{s}$  indicates a depth of 10 green recoils.

### 3.3 Superfluid to Mott-Insulator Quantum Phase Transition

#### 3.3.1 Mean-field theory for a Bose-Hubbard model

##### Short-range interactions in quantum gases

Now let's turn to the many-particle Hamiltonian. In quantum gas experiments with low density and low temperature, the inter-particle distance and lattice spacing are

usually much larger than the hardcore radius of the inter-atomic potential. In this limit, the short-range details of this potential could be ignored, and inter-particle interaction is characterized by a single parameter, the  $s$ -wave scattering length  $a_s$ . In most cases, an effective pseudo-potential captures most part of the effects of the short-range interaction between atoms,

$$V_{int}(\mathbf{r} - \mathbf{r}') = g\delta(\mathbf{r} - \mathbf{r}') \quad (3.18)$$

with parameter  $g$  defined as  $g \equiv 4\pi\hbar^2 a_s/m$ . A more stringent form of this contact pseudo-potential contains a regularization operator  $\frac{\partial}{\partial r}r$ , which can be left out as long as the wavefunction is slowly varying at short range.

The  $s$ -wave scattering length depends only on the details of inter-atomic potential, and is fixed once the internal atomic structure is given. However, if couplings exist between the collision channels and bound state channels of this potential, one could apply a magnetic field to shift the potentials of two channels with different magnetic moment with respect to each other. Resonant scattering behavior would occur when the two channels are near degeneracy. This phenomenon is called magnetic Feshbach resonance, and was first observed in [29]. Unfortunately, most BEC systems suffer from strong inelastic collision losses near a Feshbach resonance, which limits the atomic density and lifetime. In contrast, strongly interacting fermions are generally longer-lived due to their different quantum statistics, and examples include broad Feshbach resonances found in  $^6\text{Li}$  and  $^{40}\text{K}$ . Feshbach resonance is a useful technique to change atomic interaction in quantum gas experiments, whenever it is available.

## The Bose-Hubbard model

Second quantization of the atomic interaction in the Wannier basis goes as follows

$$\begin{aligned} H_{int} &= g \sum_{\sigma, \sigma'} \int d\mathbf{r} \psi_{\sigma}^{\dagger}(r) \psi_{\sigma'}^{\dagger}(r) \psi_{\sigma'}(r) \psi_{\sigma}(r) \\ &= \sum_{\sigma, \sigma'} \sum_{\mathbf{R}_1 \mathbf{R}_2 \mathbf{R}_3 \mathbf{R}_4} \sum_{\nu_1 \nu_2 \nu_3 \nu_4} \frac{U_{\mathbf{R}_1 \mathbf{R}_2 \mathbf{R}_3 \mathbf{R}_4}^{\nu_1 \nu_2 \nu_3 \nu_4}}{2} c_{\mathbf{R}_1 \nu_1 \sigma}^{\dagger} c_{\mathbf{R}_2 \nu_2 \sigma'}^{\dagger} c_{\mathbf{R}_3 \nu_3 \sigma'} c_{\mathbf{R}_4 \nu_4 \sigma} \end{aligned} \quad (3.19)$$

where the interaction strength is a product of the Wannier state overlap,

$$U_{\mathbf{R}_1\mathbf{R}_2\mathbf{R}_3\mathbf{R}_4}^{\nu_1\nu_2\nu_3\nu_4} = \frac{4\pi\hbar^2 a_s}{m} \int d\mathbf{r} w_{\nu_1}^*(\mathbf{r} - \mathbf{R}_1) w_{\nu_2}^*(\mathbf{r} - \mathbf{R}_2) w_{\nu_3}(\mathbf{r} - \mathbf{R}_3) w_{\nu_4}(\mathbf{r} - \mathbf{R}_4) \quad (3.20)$$

Again, a few simplifications can be applied here. First of all, since Wannier states are localized, the dominant contribution corresponds to the on-site interaction when more than one particle occupy the same lattice site. Furthermore, for deep lattices, higher bands are separated from the lowest one and can be neglected. This leaves us only the on-site interaction in the lowest band,

$$H_{int} = \sum_{\mathbf{R}_i} \sum_{\sigma, \sigma'} \frac{U_0}{2} c_{\mathbf{R}_i\sigma}^\dagger c_{\mathbf{R}_i\sigma'}^\dagger c_{\mathbf{R}_i\sigma'} c_{\mathbf{R}_i\sigma} \quad (3.21)$$

where on-site interaction is

$$U_0 = \frac{4\pi\hbar^2 a_s}{m} \int d\mathbf{r} |w_1(\mathbf{r} - \mathbf{R}_i)|^4 \quad (3.22)$$

Together with the single-particle Hamiltonian, we have derived the general form of a single-band Hubbard model,

$$H = \sum_{i,\sigma} \epsilon_0 c_{i\sigma}^\dagger c_{i\sigma} - \sum_{\sigma} \sum_{\langle ij \rangle} t c_{i\sigma}^\dagger c_{j\sigma} + \sum_{\sigma, \sigma'} \sum_i \frac{U_0}{2} c_{i\sigma}^\dagger c_{i\sigma'}^\dagger c_{i\sigma'} c_{i\sigma} \quad (3.23)$$

For a single-component bosonic system, this is known as the Bose-Hubbard model (setting the energy offset to zero)

$$H = - \sum_{\langle ij \rangle} t c_i^\dagger c_j + \sum_i \frac{U_0}{2} c_i^\dagger c_i^\dagger c_i c_i = -t \sum_{\langle ij \rangle} c_i^\dagger c_j + \frac{U_0}{2} \sum_i n_i (n_i - 1) \quad (3.24)$$

The two parameters in this model, the nearest-neighbor tunneling  $t$  and on-site interaction  $U$ , are numerically calculated for an equal-strength three-dimensional cubic lattice as a function of lattice depths  $V_0/E_R$  in Fig. 3-6.

The kinetic and interaction terms favor quantum states with very different characters. When the kinetic energy dominates, that is  $t \gg U$ , the system minimizes its

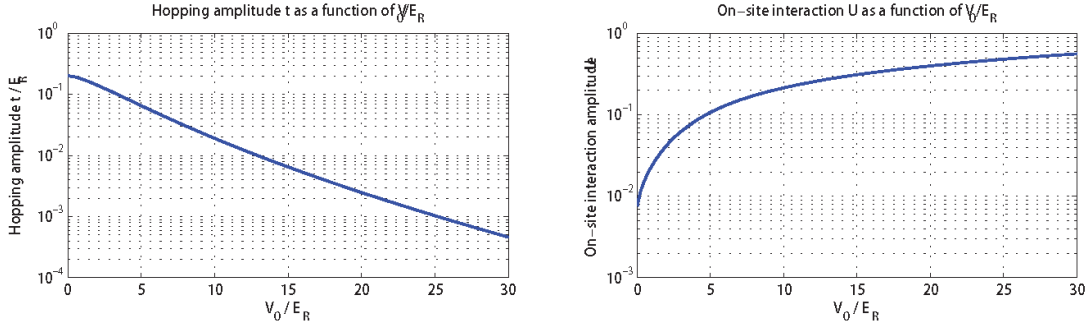


Figure 3-6: Tunneling amplitude  $t$  and on-site interaction  $U$ , as a function of lattice depth  $V_0$ , for a three-dimensional cubic lattice. Tunneling amplitude  $t$  is plotted in units of  $E_R$ , and on-site interaction  $U$  is in units of  $100E_R a_s/d$ , with  $a_s$  the scattering length and  $d$  the lattice spacing. As we increase the lattice depth, tunneling  $t$  decreases because of the reduced overlap between neighboring sites, and interaction  $U$  slightly increases because of the squeezing of localized Wannier states.

energy by having particles delocalize and be at zero momentum. The ground state is a superfluid that can be written as

$$|\Psi_{SF}\rangle_{U/t \rightarrow 0} = \left(\frac{1}{M} \sum_{i=1}^M a_i^\dagger\right)^N |0\rangle \quad (3.25)$$

where  $M$  is the total number of lattice sites,  $N$  is the total number of particles, and local creation operator  $a_i^\dagger |n\rangle = |n+1\rangle$  at  $i$ th site. In a grand canonical ensemble, it is a coherent state at each site with an average density  $n = N/M$ , and occupation shows Poissonian statistics.

When the on-site interaction dominates, that is  $U \gg t$ , the system minimizes its energy by having particles uniformly distribute and suppress particle-hole excitation. The ground state is a Mott insulator, which consists of a product of Fock states with the same number of particles on each site,

$$|\Psi_{MI}\rangle_{t/U \rightarrow 0} = \prod_{i=1}^M (a_i^\dagger)^n |0\rangle \quad (3.26)$$

A quantum phase transition from a superfluid to a Mott insulator occurs when the ratio  $t/U$  is tuned across the critical value in the Bose-Hubbard model. This is

usually done experimentally by varying the lattice depth because of the convenience.

### Mean-field theory for Bose-Hubbard model

Let's start with the single-component Bose-Hubbard model in a grand canonical ensemble,

$$H = - \sum_{\langle ij \rangle} t_{ij} c_i^\dagger c_j + \frac{U_0}{2} \sum_i n_i (n_i - 1) - \mu \sum_i n_i \quad (3.27)$$

A mean-field theory is formulated by replacing operators by their expected values. In this case, they are the expected values of creation and annihilation operator of the neighboring sites acting as an effective field.

In this mean-field approach, the tunneling term can be decomposed as

$$c_i^\dagger c_j \rightarrow \text{const} + \langle c_i^\dagger \rangle c_j + c_i^\dagger \langle c_j \rangle + \text{quantum fluctuations} \quad (3.28)$$

then the effective Hamiltonian can be written as

$$H_{eff}^i = -\lambda_i c_i^\dagger - \lambda_i^* c_i + \frac{U_0}{2} n(n-1) - \mu n \quad (3.29)$$

This mean field, or sometimes referred as the “Weiss field”, is characterized by parameter  $\lambda_i$ . It is no longer a quantum operator but a constant, and it is evaluated by taking the average of expected values of nearest-neighbor tunneling

$$\lambda_i = \sum_j t_{ij} \langle c_j \rangle \quad (3.30)$$

For a homogeneous and isotropic Bosonic system, all nearest-neighbor couplings have equal strength. This means that the “Weiss field” is proportional to the total number of nearest-neighbors, or the connectivity  $z$ ,

$$\lambda = z t \langle c \rangle \quad (3.31)$$

In the mean-field theory, we assume different lattice sites are coupled only via

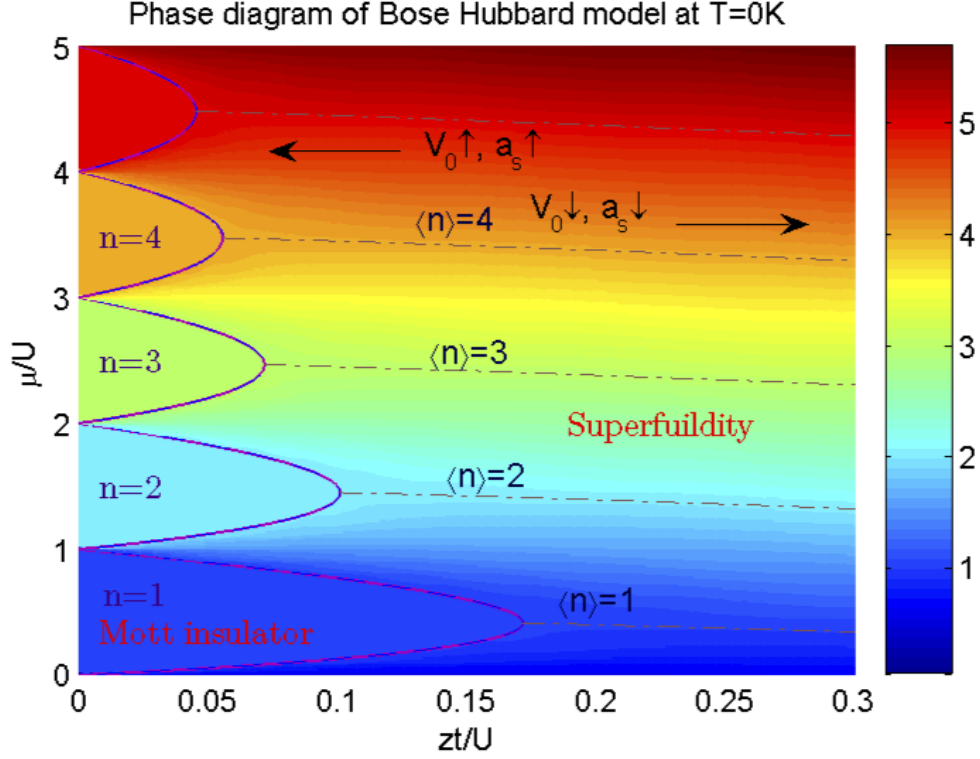


Figure 3-7: Phase diagram of the Bose-Hubbard model at zero temperature is plotted as a function of chemical potential  $\mu/U$  and normalized tunneling  $zt/U$ . The predicted phase transition is shown in solid purple line for a first-order perturbation theory, and in dashed blue line for numerical simulation. The dotted-dashed gray lines show the trajectory for a gas with various integer fillings in the superfluid phase. The critical ratio of  $(U/zt)_c \simeq 5.83, 9.90$  and  $13.93$ , for the filling number  $n = 1, 2$  and  $3$ , respectively, and it asymptotically reaches  $4n$  when  $n$  is large [30].

this effective field, and quantum fluctuations and short-range correlations can be neglected. This effectively reduces the Bose-Hubbard model into a local problem at each site with self-consistent requirement. One could use the Fock states  $|0\rangle, |1\rangle, |2\rangle$ , etc., as the basis, the effective Hamiltonian in the mean-field theory is written as

$$H_{\text{eff}} = H - \mu N = \begin{pmatrix} 0 & -zt\langle c \rangle & & & \\ -zt\langle c \rangle & -\mu & -\sqrt{2}zt\langle c \rangle & & \\ & -\sqrt{2}zt\langle c \rangle & U - 2\mu & -\sqrt{3}zt\langle c \rangle & \\ & & -\sqrt{3}zt\langle c \rangle & 3U - 3\mu & \dots \\ & & & \dots & \dots \end{pmatrix} \quad (3.32)$$

To solve this problem, one first diagonalizes the Hamiltonian and finds the ground state, which is a superposition of Fock states. This calculated ground state is then used to evaluate the expected value  $\langle c \rangle$ , and subsequently the Weiss field  $z'$ . Iterate this procedure until  $z$  converges, that's when the self-consistent condition is satisfied.

The Weiss field  $\lambda$  is also an order-parameter to characterize the quantum phase transition from a superfluid to a Mott insulator. It is non-vanishing in the superfluid phase, and zero in the Mott insulator phase. The mean-field predictions of the Bose-Hubbard model phase diagram are summarized in Fig. 3-7.

### Density distribution in an inhomogeneous system

Optical lattice experiments are usually carried out in a finite-size and inhomogeneous setting. For example, there are often residual harmonic confinements associated with the lattice beams, or from additional dipole traps.

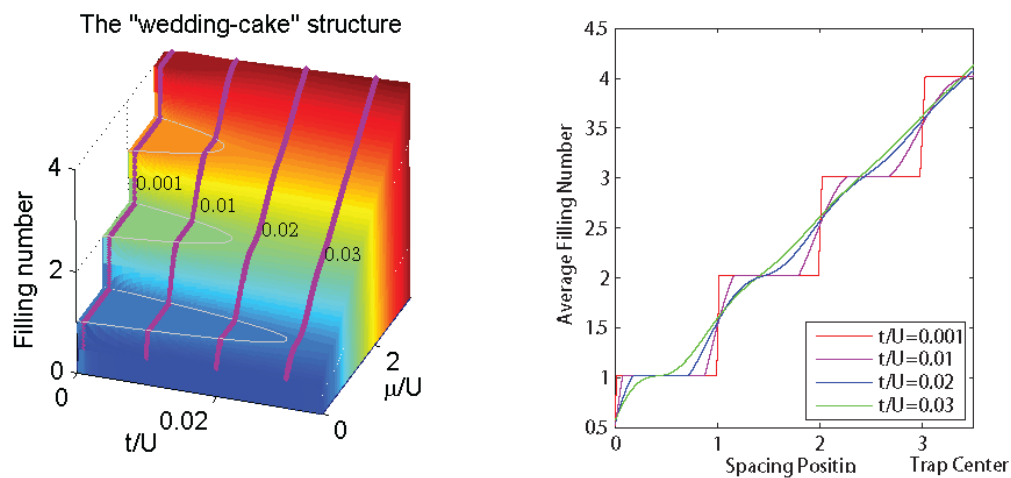


Figure 3-8: Left: Phase diagram of the Bose-Hubbard model in a three-dimensional lattice. An incompressible Mott insulator is found inside each lobe with integer filling. Right: Atomic density distribution plotted as a function of  $t/U$  in a harmonic trap. The density distribution is obtained by taking the cross section at fixed  $t/U$  from the left phase diagram.

Local density approximation (LDA) is valid when these additional potentials are slowly-varying in space compared with the lattice potential. Therefore, locally the

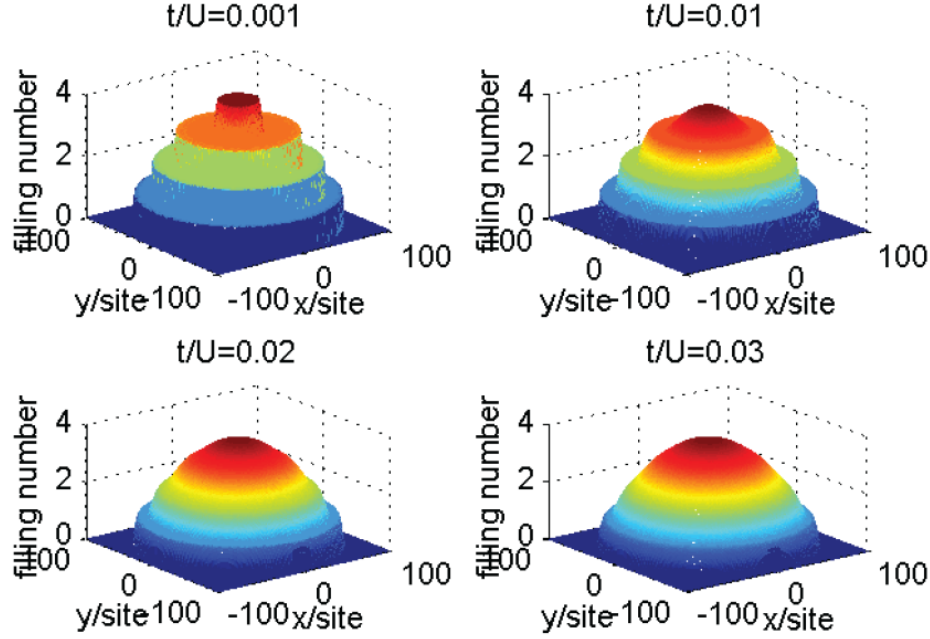


Figure 3-9: The density distribution of the Bose-Hubbard model in a harmonic trap. The “wedding cake” structure results from the incompressibility in the Mott insulator. Four density profiles are simulated with  $6.0 \times 10^4$  atoms in a  $200 \times 200$  two-dimensional lattice, with parameter  $t/U = 0.001, 0.01, 0.02$  and  $0.03$ , respectively, covering the phase transition from a Mott insulator to a superfluid.

atomic cloud can be regarded as a homogeneous system, with a local chemical potential

$$\mu(\mathbf{r}) = \mu_0 - V_T = \mu_0 - m\omega_0^2 r^2 / 2 \quad (3.33)$$

With the local density approximation, one can extract the density profile in a trap from a cross section in the phase diagram shown in Fig. 3-8, as the local chemical potential is higher in the trap center and lower near the edge. Depending on  $t/U$ , the density profile shows dramatic difference across the phase transition. When  $t/U$  is large and the superfluid phase prevails, the density profile is smoothly-varying, similar to a weakly interacting Bose gas in the trap with a modified effective mass. When  $t/U$  is very small and the Mott insulator phase dominates, the density profile

shows flat Mott plateaus with integer filling, and sharp edges between these plateaus.

The density distribution of a Mott insulator with discretized plateaus is sometimes referred as the “wedding-cake” structure, illustrated in Fig. 3-9. It is a clear signature of the Mott insulator, and has been experimentally detected via high-resolution in-situ imaging [16, 17]. The Mott insulator also features a finite energy gap and exponentially-vanishing compressibility, and was previously observed in [15, 31].

### **3.3.2 Observation of the superfluid to Mott insulator transition**

Quantum phase transition from a superfluid to a Mott insulator is one of the recent highlights in quantum simulation with ultra-cold atoms. It was first reported from the Munich group in 2002 [15], and still regarded as a solid starting point for optical lattice experiments. For this reason, we have characterized our new apparatus by observing this quantum phase transition and measuring the lifetime of the Mott insulator, and demonstrated the capability of simulating new interesting Hamiltonians and exotic quantum states in our optical lattice system.

#### **Detecting the phase transition in the interference pattern**

A loss of coherence in the time-of-flight interference pattern for a Mott insulator, as demonstrated in the very first experiment [15], is a clear and robust signal of the phase transition.

To drive the system from a superfluid to a Mott insulator, one typically could either reduce the tunneling by ramping up the lattice, or increase the on-site interaction via Feshbach resonance. The latter option is not available for us, due to the lack of broad Feshbach resonance in  $^{23}\text{Na}$ , and the limited condensate lifetime caused by strong inelastic collisions near a Feshbach resonance [29].

In this experiment, after a pure condensate is prepared in the optical dipole trap, a three-dimensional lattice is adiabatically ramped up to its final depth in 100 *ms*. Afterwards, the lattice and dipole trap are simultaneously turned off, and an absorption

image of the cloud is taken after 10  $ms$  free expansion in the time of flight.

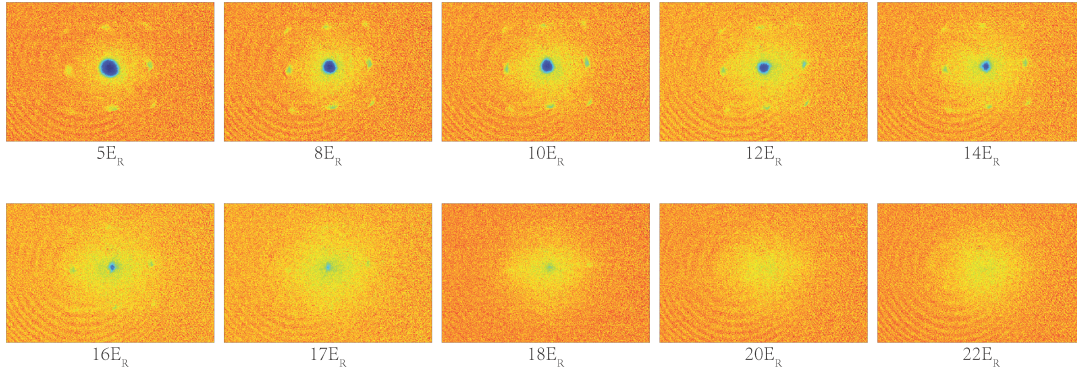


Figure 3-10: Experimental observation of a superfluid to a Mott insulator quantum phase transition. An optical lattice is adiabatically ramped up to its final depth in 100  $ms$ , then simultaneously turned off with the dipole trap to release the gas for free expansion. The sharp peaks in the expanded cloud indicate superfluid coherence across the sample in shallow lattices, and they disappear as the sample goes across the phase transition into a Mott insulator.

In Fig. 3-10, we've shown the time-of-flight image of the condensate after being released from the optical lattice with variable depths. The sharp peaks in the expanded cloud correspond to the  $\pm 2k_L$  components of the ground state with quasi-momentum  $q = 0$ , indicating a global coherence and a uniform phase across the sample. These interference peaks disappear in deep lattices, as the sample goes across the phase transition into a Mott insulator and loses the global coherence.

### Measuring the Mott insulator lifetime

To demonstrate that the loss of coherence is in fact due to the Mott insulator phase transition, rather than heating of the sample caused by the deeper lattice, and to characterize the technical heating in our apparatus, we perform a lifetime measurement of the sample in the Mott insulator phase. The experimental sequence is that, we start with a superfluid, ramp it into a Mott insulator and hold it for a variable amount of time, and then ramp it back to a superfluid to measure the residual coherence.

The results are shown in Fig. 3-11, from where we see the coherence of the sample almost disappears after 150  $ms$  hold in the Mott insulator at  $22E_R$ . This measured

lifetime is mostly limited by three-body collision loss, and reducing the atomic density should significantly improve the lifetime of the Mott insulator to be around a second, suitable for studying super-exchange physics in optical lattices in the future.

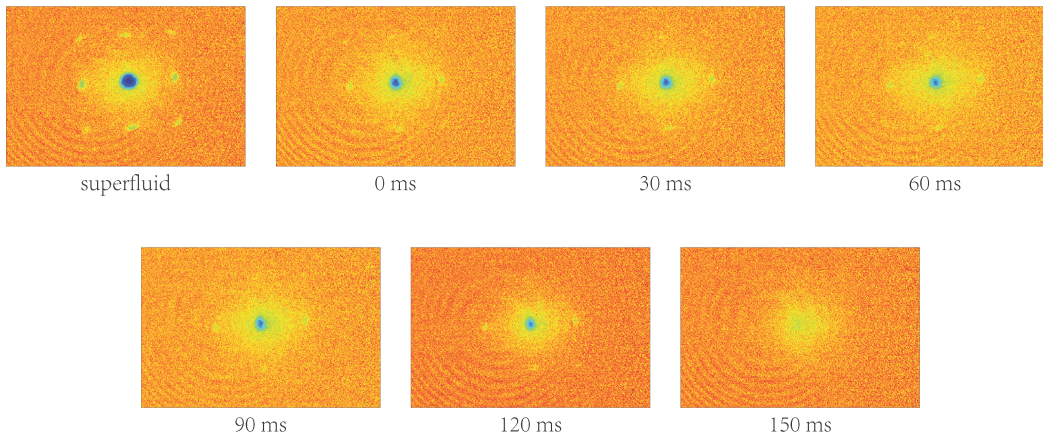


Figure 3-11: The lifetime of a Mott insulator at  $22E_R$ . A superfluid is first prepared in a lattice at  $8E_R$ , which is then ramped up to  $22E_R$  in  $100\text{ ms}$  and held for a variable time, and finally ramped back down to  $8E_R$  in  $20\text{ ms}$ . The loss of the coherence as we increase the hold duration in the Mott insulator occurs as a result of heating, typically from three-body collisions or mechanical vibrations of the optics.

### 3.4 Tilted Lattices and Bloch Oscillations

When a uniform gradient potential is applied to the condensate in an optical lattice, the atoms experience a constant force and undergo Bloch oscillations. This tilt creates an energy offset  $\Delta$  between every neighboring sites, providing another energy scale besides tunneling  $t$  and on-site interaction  $U$ . Tilted optical lattices is an ideal platform to study the dynamics of interacting particles in Bloch oscillations, or to implement Raman-assisted tunneling and realize synthetic gauge fields for quantum gases in optical lattices [25].

### 3.4.1 Bloch oscillation

Atoms in a tilted lattice have their quasi-momentum increase linearly until they are resonantly reflected at the edge of the Brillouin zone. Bloch oscillations can be directly observed from the time evolution of the momentum distribution in time-of-flight, or from the periodic center-of-mass motion in position space.

For small tilts, the semiclassical equations for the Bloch oscillation are

$$\dot{k} = \hbar F \tag{3.34}$$

$$\dot{r} = \frac{\partial E_k}{\partial k} \tag{3.35}$$

where  $k$  is the quasi-momentum in the lattice. In the tight-binding limit and with a constant external force, the center-of-mass motion is

$$x - x_0 = \frac{2Jd}{F} \cos[(k_0 + Ft)d] \tag{3.36}$$

For strong tilts, the Hamiltonian with nearest-neighbor tunneling is diagonalized by the following Wannier-Stark states,

$$|\phi(m)\rangle = \sum_n K_{n-m} \left(\frac{2J}{\Delta}\right) w(x - x_n) \tag{3.37}$$

where the  $K_i$  are the Bessel functions. The Wannier-Stark states are localized at each site, when the tilt  $\Delta$  is much larger compared to the bandwidth  $J$ . Bloch oscillations in this regime can be understood from the ladder of accumulated phases along the lattice, which are linearly increasing in time and equally spaced in space.

Bloch oscillations are experimentally observed in time-of-flight images, shown in Fig. 3-12. In this measurement, a strong magnetic field gradient is suddenly switched on by rapidly turning off one of the magnetic coils running in Helmholtz configuration. Bloch oscillations up to four cycles are recorded, before the sample heats up and loses the coherence. The measured oscillation period at  $T \simeq 0.5 \text{ ms}$  gives an estimate of the tilt at  $\Delta \simeq \hbar \times 2 \text{ kHz}$ . However, the tilt strength seems to vary in time, possibly

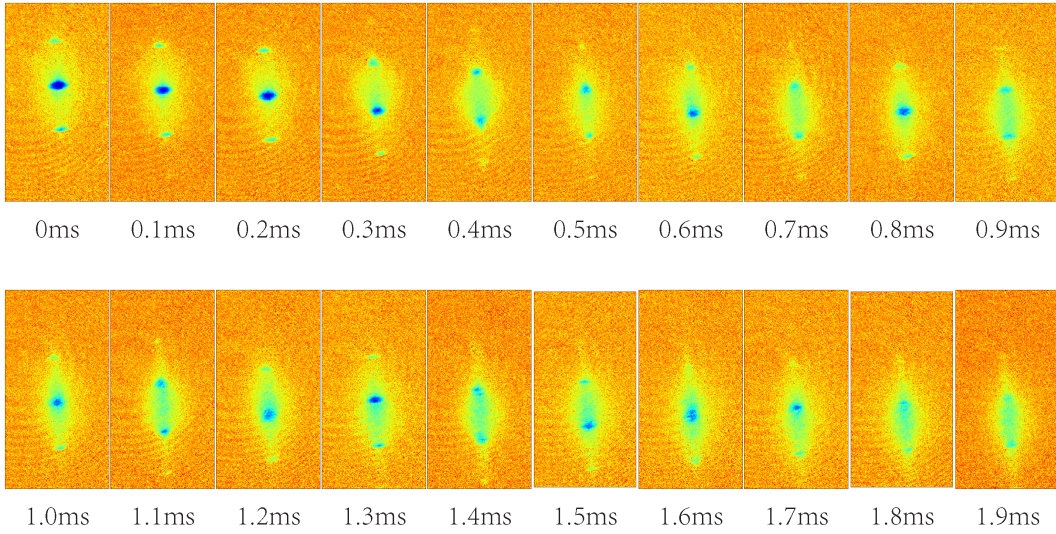


Figure 3-12: Bloch oscillations in a three-dimensional optical lattice, with  $20E_R$  along the tilt direction and  $5E_R$  in the transverse directions. A tilt potential of  $\Delta \simeq h \times 2$  kHz is applied for a variable duration from 0 to 2 *ms*.

due to drifts from the sudden switch-on of the magnetic field gradient.

The technical reason for switching on the tilt by turning off the coils is to reach a maximum switch-on speed. Given the harmonic confinement in a dipole trap, if the tilt is switched on gradually, the atomic cloud simply follows an adiabatic shift to new equilibrium in the trap. However, the large inductance of the coils means that the rate of change of the magnetic field gradient is proportional to the voltage across the coils. By turning the coils off, rather than on, it is possible to generate a huge transient voltage across the coils and switch on the tilt faster, without the need of building a capacitor circuit to boost the switch-on speed.

### 3.4.2 Dynamical instability

In the presence of interactions, Bloch oscillations can be damped due to a dynamical instability that occurs for states above a certain critical value of the quasi-momentum. The damping process goes as follows: for two particles at quasi-momentum  $q$ , a two-body collision results in one particle at  $q + \Delta k$  and the other at  $q - \Delta k$ , which conserves the quasi-momentum but may release excessive energy. The excessive energy can be

transferred into the transverse directions in the case of a one-dimensional lattice where the transverse directions have a free-particle dispersion relation. However, in the case of a three-dimensional lattice where the transverse directions are strongly confined and have flat bands, the excessive energy has no place to go and therefore the losses are strongly suppressed.

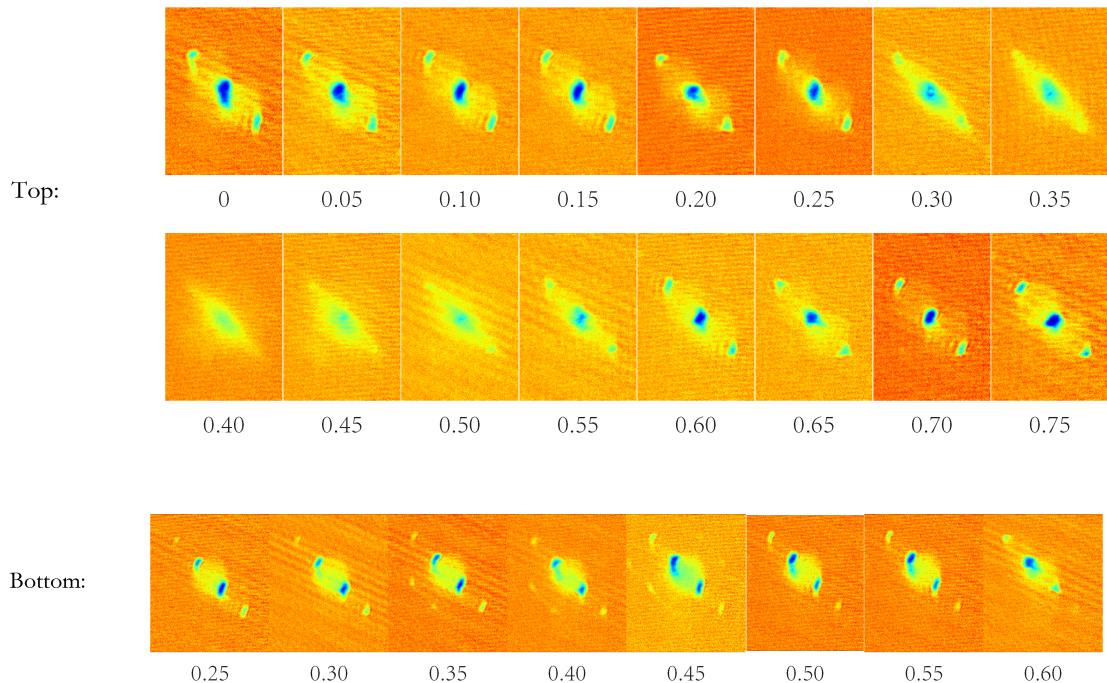


Figure 3-13: Experimental observation of dynamical instability. Top: condensates at a variable quasi-momentum are prepared by accelerating the lattice, held for 2 ms, and then ramped back to zero quasi-momentum before being released from the trap. Bottom: condensates at a variable quasi-momentum are prepared by accelerating the lattice, and immediately released from the trap to measure the momentum distribution. Image captions in this figure are in arbitrary units proportional to the value of the quasi-momentum during the hold on the top. Quasi-momentum states near the edge of the Brillouin zone (from 0.35 to 0.5 in the figure) show rapid heating and loss of coherence. This could be explained by dynamical instability.

When the dispersion relation is concave upward, the energy that is lost from the particle at  $q - \Delta k$  is not enough to excite the other particle at  $q + \Delta k$ . These quasi-momentum states, such as free particles or quasi-momentum states near  $q = 0$  in an optical lattice, are therefore stable against two-body collisions. However, the

dispersion relation becomes convex upward above the inflection point. In this regime, two-body collisions are allowed as the final states under energy conservation become available, and the sample undergoes rapid dephasing and heating.

We study dynamical instability in an alternate experimental configuration, where we create a moving lattice with a constant acceleration and the fictitious force in the moving frame drives the atoms undergo Bloch oscillations. A pair of non-retroreflected Raman beams are used to create this moving lattice, and the velocity of the moving lattice is a product of the wavelength and the frequency difference between the two beams. A constant acceleration of the moving lattice is generated by applying a linear frequency ramp in one of the Raman lattice arms.

This method has the disadvantage that the cloud can move out of the trap or the field of view in a matter of milliseconds, because the imaging system and transverse confinement exist in the stationary lab frame. However, it has a distinct advantage that the tilt can be easily stopped, restarted, or reversed, and can be programmed in arbitrary waveforms. As a result, compared with the magnetic field gradient, the tilt in an accelerated lattice is more controllable and uniform in time, although the time window for experimental observation is limited to a few cycles of Bloch oscillations.

In Fig. 3-13, we hold the condensate at a variable quasi-momentum to observe the onset of the dynamical instability. The sample is first prepared at a target quasi-momentum by accelerating the optical lattice, held for 2 *ms*, and then ramped back to zero quasi-momentum before release from the trap. Quasi-momentum states near the edge of the Brillouin zone have shown rapid heating and loss of coherence, consistent with the theory of dynamical instability.

To our surprise, further experiments have shown a decay of the cloud down to the ground state at zero quasi-momentum, even though dynamical instability could not occur in these states. These measurements, shown in Fig. 3-14, were carried out in a stationary lattice with magnetic field gradient tilts, where we first turn off one of the bias coils to initiate the Bloch oscillation, and subsequently turn off the second coil in the pair to ‘freeze’ the quasi-momentum. The decay of these finite-momentum states occurs at a timescale much faster than the nearest-neighbor tunneling, and the cloud

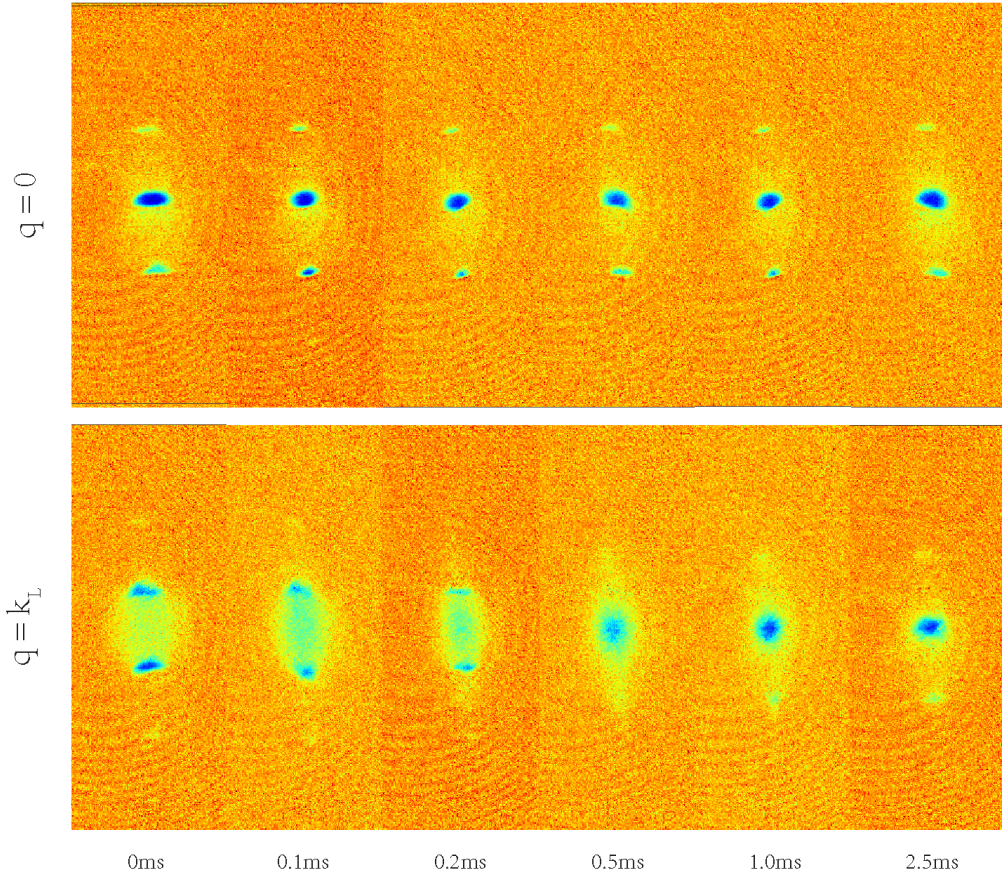


Figure 3-14: Rapid decay of quasi-momentum states near the edge of the Brillouin zone. A tilt pulse is applied to prepare the condensate at the edge of the Brillouin zone. This tilt is then switched off, and time-of-flight images are taken after a variable hold up to  $2.5 \text{ ms}$ . Compared with the ground state at  $q = 0$ , quasi-momentum state at  $q = k_L$  shows rapid decay into the ground state, which could not be explained by simple two-body collisions alone.

always relaxes into the zero-quasi-momentum state. A complete understanding of the underlying mechanism for this decay is still unknown: our experimental observations could not be fully explained by two-body collisions alone, and suggest many-body effects in this process.



# Chapter 4

## Quantum Simulation in Superlattices

### 4.1 Introduction

In this chapter, we will present the experimental implementation of a new scheme using pseudo-spins in a superlattice to simulate spin-orbit coupling physics with ultracold atoms. This system is ideal to prepare and study the stripe phase which simultaneously breaks the gauge symmetry and translational symmetry, and will potentially allow us to explore exotic topological states of matter.

In contrast to the spin-orbit coupling in atomic physics which describes the interactions between the orbital and spin angular momentum of an electron  $L \cdot S$ , and in part gives rise to the fine structure splitting in the atomic structure, the spin-orbit coupling in condensed matter systems couples particle momentum with its spin  $k \cdot \sigma$  and modifies the band structure. Two-dimensional spin-orbit couplings play a crucial role in spin-Hall materials, topological insulators and topological superfluids [32, 33].

To simulate spin-orbit coupling with ultracold atoms, we need to couple two spin states with a momentum transfer. For simplicity, let's consider the one-dimensional problem and the spin states have the free-particle dispersion relation. After a spatial and a temporal unitary transformation, the effective spin-orbit coupling Hamiltonian to be simulated is written as

$$H_0 = \frac{\hbar^2(k + k_L/2 \cdot \sigma_z)^2}{2m} + K\sigma_x + \delta_0\sigma_z \quad (4.1)$$

where  $K\sigma_x$  is the spin-orbit coupling term, and  $\delta_0\sigma_z$  is the Zeeman term.

The single particle band structure of this Hamiltonian is shown in Fig. 4-1. As we turn on the spin-orbit coupling, the eigenstate will be a superposition of opposite spins with shifted momentum. When spin-orbit coupling is weak, there are two degenerate ground states. Depending on the miscibility of the system, particles can stay miscible and form density stripes or phase separate [39]. In contrast, when spin-orbit coupling is very strong, only a unique ground state is available.

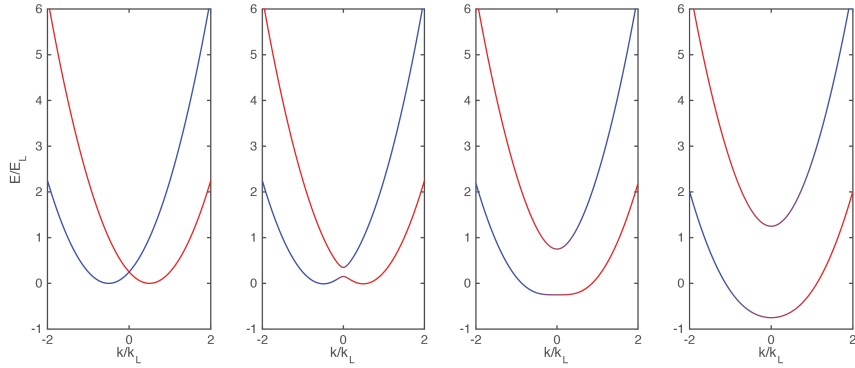


Figure 4-1: The single particle band structure of the spin-orbit coupling Hamiltonian. The spin-orbit coupling strength increases from left to right, and the colors represent the two spin components.

Previously in the pioneering experiment in Ian Spielman’s group, hyperfine states of  $^{87}\text{Rb}$  were used to simulate a one-dimensional spin-orbit coupling Hamiltonian [34]. In this experiment, the single particle spin-orbit coupling band structure was studied. Later, similar techniques were used in fermionic systems to create spin-orbit coupled Fermi gases [35, 36].

However, there are two major limitations with the hyperfine state scheme. First of all, to drive a two-photon transition between hyperfine states, near-resonant light needs to be used. This severely limits the lifetime of the system. Second, for the bare interactions between hyperfine states,  $g_{\uparrow\downarrow} \simeq g_{\uparrow\uparrow}, g_{\downarrow\downarrow}$ , and the system prefers to stay immiscible. This results in a small window for the stripe phase in the phase diagram

and weak density stripes, making the experimental detection very difficult.

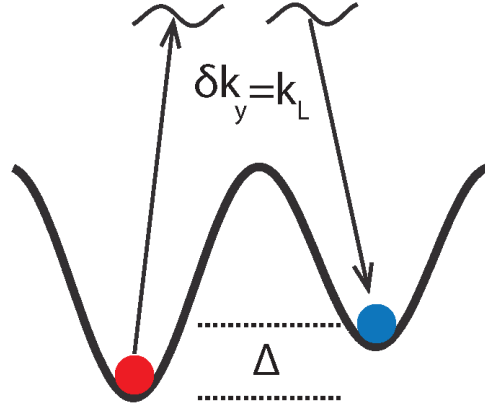


Figure 4-2: A new scheme to simulate spin-orbit coupling physics. The pseudo-spins in a double well are coupled via a two-photon process to compensate the energy offset and provide momentum transfer. Because no real spin flip is needed, far-detuned laser beams can be used.

To overcome these limitations, we have implemented a new scheme using pseudo-spins in a double well potential to simulate spin-orbit couplings, illustrated in Fig. 4-2. In this scheme, only one hyperfine state is involved and real spin flips are not required, far-detuned laser beams can be used. Furthermore, because of the spatial separation between opposite spin states,  $g_{\uparrow\downarrow} \ll g_{\uparrow\uparrow}, g_{\downarrow\downarrow}$ , the system prefers to stay miscible and therefore is ideal to prepare and study the stripe phase.

In this chapter, we will first describe the experimental techniques to create and control an optical superlattice with 532 nm and 1064 nm laser beams. Then we'll experimentally characterize and calibrate our superlattice system, in particular its phase and band structure. Finally, we'll describe the spin-orbit coupling experiment in detail. First, the theory of spin-orbit coupling in this system is developed, including the exact derivation of the single-particle Hamiltonian, the comparison of the spin-orbit coupling and onsite coupling, and the phase transitions in an interacting spin-orbit coupled system. Then our experimental realization of the spin-orbit coupling Hamiltonian is presented, where we discuss the state preparation techniques, experimental results on detecting the resonant spin-orbit coupling signal and the dynamics in the upper state, as well as proposal to use Bragg scattering to directly probe the stripes.

## 4.2 Experimental Setup and Techniques

In this section, we will describe the experimental techniques for the second-harmonic generation of 532 nm green light, the phase control of the superlattice, as well as the preparation of our Raman beams. Besides the implementation and performance of our chosen scheme, other available solutions and their pros and cons are also discussed.

### 4.2.1 Second-harmonic generation for 532 nm green lattice

#### Laser source selection

Single-mode high-power 1064 nm fiber lasers have been available for quite a while, and have been used for optical lattice experiments at the CUA in the past decade. Based on our experience, the best configuration for building the high-power infra-red system is to dedicate a high-quality single-mode laser as the seed, combined with powerful fiber amplifiers downstream. In this case, one could use a seed laser powerful enough to drive multiple fiber amplifiers when high power is in demand, or have the option to swap seed lasers for diagnosis purposes and special needs, or implement light control such as frequency modulation involving only the low power seed light, instead of the amplified light with full power.

For 532 nm green light, there are mainly two options for us. The first one is to find a turnkey high-power single-mode laser that is commercially available. We have found a few candidates: IPG Photonics offers the GLR-20 which is a 20-Watt single-mode fiber laser, Coherent Inc offers the Verdi V series that can go up to 18 Watts and was claimed to be a single-frequency laser, and Spectra-Physics offers the single-frequency Millennia Edge that has a maximum output of 6 Watts. Some other options include the 18-Watt Sprout from Lighthouse Photonics, and the 25-Watt Millennia eV from Spectra-Physics, but both are multi-mode lasers and thus not suitable for optical lattice experiments.

The other option is to frequency double the 1064 nm light in house, using relatively cost-effective and high-power sources at this wavelength. The advantage of the former solution is the convenience and low maintenance of a turnkey equipment, and possibly

a higher optical power they could provide. On the other hand, one needs to phase lock the IR and green lasers to stabilize the relative frequency against long-term drifts in a superlattice experiment. Furthermore, there are still some concerns about the single-mode quality and linewidth of aforementioned commercial products. In the end, we decided to make our own frequency-doubled green light.

In our system, a 2-Watt Coherent Mephisto laser is used as the seed laser, which is powerful enough to simultaneously drive multiple fiber amplifiers. For fiber amplifiers, we have two 50-Watt units from Nufern, with one dedicated for 1064 nm IR lattices, and the other one for frequency doubling and generating 532 nm green lattices. There is another older 20-Watt 1064 nm laser from IPG Photonics, which has an integrated seed. This laser has been used mostly for optical dipole traps, due to concerns on its single-modeness.

### **Second-harmonic generation for green light**

Single-frequency continuous-wave 532 nm light can be generated via second-harmonic-generation (SHG) of a high-power 1064 nm light. With the full output from a 50-Watt Nufern fiber amplifier, one could generate about 15 Watts of 532 nm in a single pass frequency doubling through a nonlinear crystal [37].

HC Photonics in Taiwan provided us the nonlinear crystals. There are two types of these crystals: PPMSLT is periodically-poled MgO (1 mol.%) dope SLT, and PPMCLT is periodically-poled MgO (1 mol.%) dope CLT. From the specifications, PPMSLT has a higher damage threshold and a slightly higher second-harmonic conversion efficiency, but unfortunately HC Photonics could no longer find vendors to consistently supply them quality wafers, and may have to discontinue this product line soon. We have received one PPMSLT crystal from their last batch, and have permanently set it up in our second-harmonic generation for the superlattice experiment. There are several PPMCLT crystals for backup, in case the current PPMSLT crystal is damaged or has degraded.

We have selected the single-pass frequency doubling scheme, because of the convenience in setting it up, as well as the sufficient output that it could generate for our

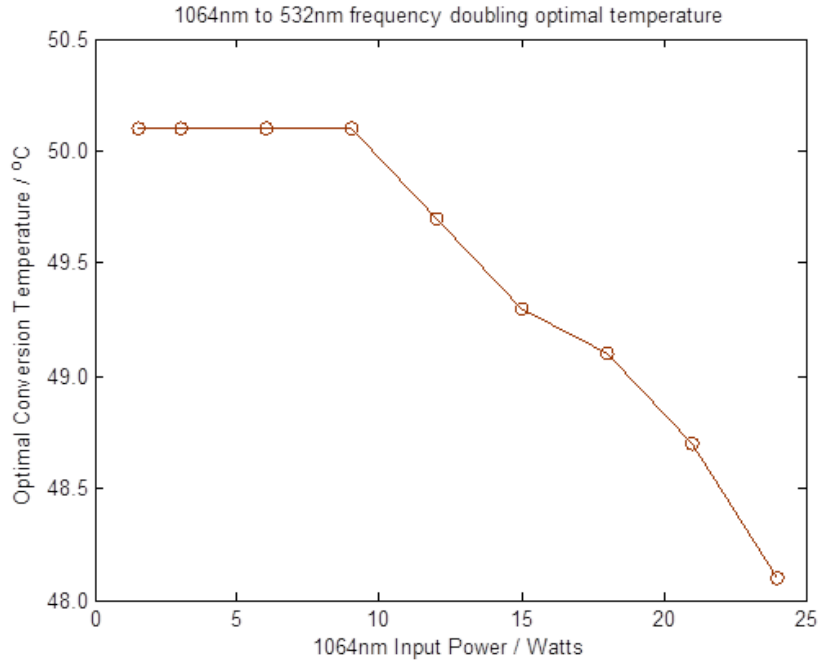


Figure 4-3: The optimal crystal temperature set point for second-harmonic-generation of 1064 nm light. When we increase the fundamental power, weak absorption from the beam creates local heating inside the crystal. This thermal effect can be compensated by reducing the set point of oven temperature, indicating there is a small temperature gradient between the sensor and the core of the crystal.

application. The SHG efficiency is highly sensitive to the phase-matching conditions, therefore the focus and beam waist of the fundamental beam are carefully chosen and well tweaked. The crystal needs to be maintained in a temperature-stabilized environment for the optimal performance. Therefore, we've mounted it in an commercial oven from HC Photonics as well. Although somewhat expensive, it is well-built and does stabilize the ambient temperature for the crystal.

Even with the oven temperature stabilized, we still have seen several-degree drop in the optimal oven temperature for second-harmonic conversion, as we increase the fundamental power from a few Watts to 30 Watts, shown in Fig. 4-3. This observation could be explained by heating from weak absorption of the fundamental light inside the crystal, and also indicates that there is a small temperature gradient between the sensor and the core of the crystal.

With the oven temperature retuned and optimized at each fundamental power, the

conversion efficiency for our 532 nm second-harmonic generation is measured in Fig. 4-4. With the fundamental beam at 25 Watts, we could get more than 6 Watts of 532 nm light, sufficient for our superlattice experiment. The characteristics and performances of the second-harmonic-generation of 1064 nm light in other configurations can be found in [37] for more details.

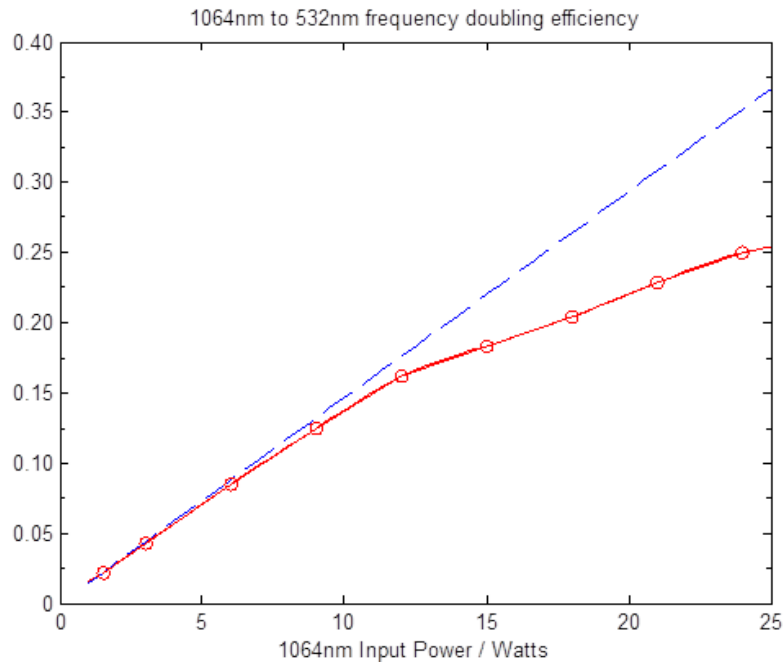


Figure 4-4: The conversion efficiency of second-harmonic-generation of 1064 nm light. The SHG efficiency is measured as a function of the fundamental 1064 nm power. The measured conversion efficiency starts to deviate from theoretic prediction above 15-Watt fundamental power. This reported conversion efficiency has taken into account the thermal effect in Fig. 4-3, as it was measured after tuning the optimal temperature at each fundamental power.

### 4.2.2 Controlling the phase of the superlattice

The phase of the superlattice, namely the relative position of the green and IR lattice, needs to be experimentally controlled to change the superlattice between all possible configurations. The major considerations for the phase control are the full range, the maximum speed, the long-term drifts, and the possibility of changing it dynamically during the experimental sequence.

	$n_{532}$	$n_{1064}$	$\Delta n$
BK7	1.5195	1.5066	0.013
Fused Silica	1.4607	1.4496	0.011
Sapphire	1.7718	1.7545	0.017
ZnSe	2.6754	2.4823	0.19
CaF <sub>2</sub>	1.4354	1.4285	0.007
MgF <sub>2</sub>	1.3789	1.3733	0.006

Table 4.1: The indices of refraction for 532 nm and 1064 nm light in various types of glass. The dispersion between green and IR light is around one percent for these glass except ZnSe. Overall, BK7 and fused silica are most suitable for our phase plate.

We have mainly considered three options for the phase control. They are rotating a dispersive glass plate on a galvo mount, sweeping the frequency of one lattice beam using an acousto-optic modulator (AOM), and changing the refractive index for one lattice beam using an electro-optic modulator (EOM). We'll discuss the pros and cons of each method in the following, meanwhile we've implemented the first two schemes in our experiment.

### Method 1: Glass Plate Phase Shifter on a Galvo

One way to control the phase of the superlattice is to use a piece of dispersive glass. By rotating the glass plate and adding different path lengths to the two wavelengths, we create a relative position shift of the two lattices at the cloud.

The index of refraction in a medium depends on the wavelength of the light, and it usually decreases for longer wavelength. This dispersive effect is about a few percent over the visible spectrum for most transparent materials. For example, for dry air at 15 °C, one atmosphere and with 450 ppm CO<sub>2</sub>, the index of refraction is 1.0002782 for 532 nm and is 1.0002740 for 1064 nm. For glass such as BK7, the index of refraction is 1.5195 for 532 nm and is 1.5066 for 1064 nm. In table 4.1, we have listed the indices of refraction for 532 nm and 1064 nm in common optical glasses.

Among these glasses, ZnSe has the strongest dispersion, but the transmission is low for visible and near-infrared light. Uncoated CaF<sub>2</sub> and MgF<sub>2</sub> glass have fairly low reflection of a few percent, but their dispersions are relatively weak. Overall, standard

BK7 and fused silica (high optical damage threshold) are the favorable options, and a layer of anti-reflection coating for 532nm and 1064nm can be applied on both surfaces of the phase plate.

Edmund Optics offers fused silica windows of thickness between 3 mm and 5 mm with various diameters. We've been using the 3 mm glass plate in our experiments, because of its light weight for fast switching. An estimated rotation about 2 degrees at 30-degree incident angle gives 266 nm shift of IR and green lattices, which corresponds to a full period of the superlattice potential.

The rotation of the glass plate needs to be computer-controlled by the Cicero Word Generator, so that the phase ramp can be synchronized in the experimental sequence. The maximum speed and repeatability of this mechanical phase control, as well as the sensitivity to electronic noise, such as radio-frequency or microwave radiations, require careful considerations. All of these aspects can be tested independently using a position sensing detector (e.g., Thorlabs PDQ80A), before integrating it into the experiment.

There are two options for mechanically controlling the glass plate. One way is to choose a piezo-based device. We find the Agilis piezo-driven rotation stage AG-PR100 from Newport that features 360-degree continuous rotation and ultra-high adjustment sensitivity. It was tested to be reasonably fast, but it has shown clear hysteresis, and the bigger headache is that they do not offer a convenient interface to Cicero. Therefore, it is not suitable for our experiment.

The other approach is to use a galvanometer scanning system. The galvanometer has two core components: an actuator that drives the load, and a position detector that monitors the load position for fast tuning and stabilization in a closed loop system. There are two types of position detectors in a galvanometer. In the traditional dielectric capacitive design, a radio frequency source is driving two variable capacitors, and the resulting rectified differential currents measure the position of the galvo actuator and load. In recent years, there has been a new design based on optical position detection. A light source illuminates parts of four photocells, and a moving butterfly-like shape between the light source and the receivers casts more or less shadow onto the pairs of

the receiver cells. As a result, the currents read out the relative position of the galvo actuator and load.

In our first attempt, we used the galvo GVS011 from Thorlabs, which seemed to be of the dielectric capacitive design. It shakes rapidly and loses its initial position during the microwave evaporation phase, and needs to be reset after every shot. On the other hand, a galvo based on optical position detection is far less sensitive to microwave and should solve this problem for our experiments. The vendors for the galvos that we have looked at include Nutfield Technology, Cambridge Technology and Thorlabs. Nutfield and Cambridge Technology have more in-depth knowledge and experience about galvo design and applications. Specifically, Nutfield offers galvos that “significantly reduce temperature based gain and offset drift and is greatly immune from radio frequency interference”.

Up to now, we have been using the galvo system Thorlabs GVS001 for the superlattice experiments, because of its short lead time and lower cost. After careful tuning of the closed loop, it can shift the superlattice phase over  $2\pi$  within one millisecond. It still picks up some microwave, and may undergo a random shift equivalent to about 10 percent of the superlattice period during the microwave evaporation, but it is able to settle back to its initial position within a deviation equivalent to one percent of the superlattice period by the end of evaporation when the microwave is turned off. This one-percent level phase uncertainty is comparable to phase drifts from other sources, such as the ambient temperature and pressure fluctuations, therefore is acceptable in terms of control precision. Overall, the one-millisecond maximum speed, one-percent precision in repeatability and the convenient interface of this galvo have met our needs for the static and slow dynamical control of the superlattice phase.

## **Method 2: AOM Frequency Shifter**

The phase of the superlattice can also be controlled by shifting the light frequency. The reason is, a one part per million shift in the frequency changes the lattice spacing by one part per million as well. This small difference might be hard to notice locally, but a finite position shift can be built up for the lattice after a distance, since a node

of the standing wave is always locked at the retro-reflection mirror. We estimate the required frequency shift to control our superlattice in the following.

The superlattice potential in the general case is

$$U(x) = -\frac{V_R}{2} \cos(2k_R x + 2\pi\phi_R) - \frac{V_G}{2} \cos(2k_G x + 2\pi\phi_G) \quad (4.2)$$

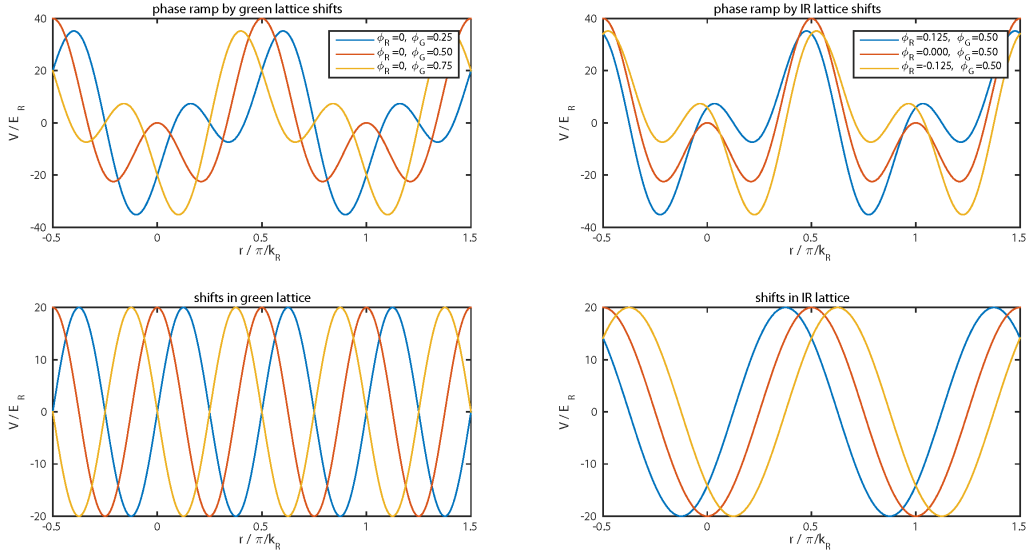


Figure 4-5: The phase control of the superlattice via AOM frequency shifter. When the frequency of one lattice beam is swept, its lattice spacing is slightly modified, but with a node fixed at the retro-mirror. This results in an effective shift in the relative position between the two lattices. The case of shifting green lattice is plotted on the left, while the case of shifting IR lattice is plotted on the right. Although the absolute shift in the relative position is the same for the two cases, shifting IR lattice requires a smaller frequency change, and also keeps the atomic wavefunction more stationary, therefore it is the favorable option.

Let's aim to shift the superlattice phase by a half of the period, which corresponds to changing from symmetric double-wells to asymmetric double-wells. As illustrated in Fig. 4-5, this is translated into a relative motion of 133 nm between the two lattices, which is half of the green lattice spacing,  $\Delta\phi_G = 0.5$  or  $\Delta N_G = 1/2$ , and a quarter of the IR lattice spacing,  $\Delta\phi_R = 0.25$ , or  $\Delta N_R = 1/4$ . It is intuitive for a sanity check, since the superlattice potential is identical if either green lattice or IR lattice moves by 266 nm, the green lattice spacing.

The number of nodes in the standing wave between the retro-reflection mirror and the cloud is

$$N = \frac{l}{\lambda/2} \quad (4.3)$$

in our experiment,  $l \simeq 500$  mm is the distance from the retro-mirror to the cloud.

It is easy to find out all relative changes are equal

$$\frac{\Delta N}{N} = -\frac{\Delta \lambda}{\lambda} = \frac{\Delta f}{f} \quad (4.4)$$

If we are shifting the green lattice,

$$N_G = \frac{500 \text{ mm}}{266 \text{ nm}} \sim 2 \times 10^6 \quad (4.5)$$

the relative frequency shift for the green lattice needs to be

$$\frac{\Delta f_G}{f_G} = \frac{\Delta N_G}{N_G} = \frac{1/2}{2 \times 10^6} = 1/4 \times 10^{-6} \quad (4.6)$$

we know the frequency of 532 nm light is

$$f_G = \frac{3 \times 10^8 \text{ m/s}}{532 \text{ nm}} = 5.6 \times 10^{14} \text{ Hz} \quad (4.7)$$

therefore, the absolute frequency shift for the green lattice needs to be

$$\Delta f_G = 1/4 \times 10^{-6} \times 5.6 \times 10^{14} \text{ Hz} = 140 \text{ MHz} \quad (4.8)$$

On the other hand, if we are shifting the IR lattice,

$$\frac{\Delta N_R}{N_R} = \frac{1/4}{N_G/2} = \frac{\Delta N_G}{N_G} \quad (4.9)$$

the absolute frequency shift for the IR lattice needs to be

$$\Delta f_R \propto f_R = \Delta f_G/2 = 70 \text{ MHz} \quad (4.10)$$

which is half of the frequency needed for shifting green lattice, and feasible by using an AOM in the double-pass configuration. Shifting the IR lattice has the additional advantage that the atomic wavefunction is more stationary during the sweep, which reduces heating and other side effects.

In short, controlling the superlattice phase by changing the frequency of IR lattice is a favorable choice, when speed is the priority and the phase only needs to be tuned within half of a period.

### **Method 3: EOM Phase Shifter**

The third way to control the superlattice phase is to use an electro-optic modulator. Depending on the type and orientation of the nonlinear crystal, as well as the direction of the applied electric field, the refractive index of an electro-optic crystal will depend on the polarization of the light. Based on this result, one could make the green and IR lattices in orthogonal polarizations, and use the electro-optic modulator to shift the phase of only one beam.

This scheme can be in practice very fast, and may allow us to shift the superlattice phase over several periods. However, standard electro-optic modulator devices usually have a small aperture of 2 mm in diameter, which require us to shrink the beam size. Furthermore, for high power beams at small beam waist, optical damage becomes an issue. For the EOMs that we've looked at, at their maximum aperture and for a beam at the laser power required for our experiments, the intensity of the beam will be fairly close to the specified optical damage threshold for these devices. There are other EOM devices which offer larger apertures. However, they are rather expensive, have longer lead time, require very high voltage drivers, and we are still unsure about the overall phase shift from the crystal expansion and the residual phase shift for the other polarization beams. In the end, we decide not to pursue this scheme.

### **Estimated phase drifts from the changes in ambient condition**

The phase of the superlattice is determined by the path length difference of the green and IR lattices from the retro-reflection mirror to the atomic cloud. This path length

is subject to changes in the ambient conditions such as temperature and air pressure. In this section, we will make estimates for these effects.

First, let's consider the path length in the air. The refractive index of air is linear in its density,

$$n(P, T, \lambda) \simeq 1 + c_\lambda \times \frac{P}{P_0} \times \frac{T_0}{T} \quad (4.11)$$

where  $c_\lambda$  is the linear coefficient that depends on the wavelength of the light. The difference in the refractive index for 532 nm and 1064 nm light is

$$\Delta n_{air} \simeq 4 \times 10^{-6} \times \frac{P}{P_0} \times \frac{T_0}{T} \quad (4.12)$$

Let's assume the maximum relative changes for room temperature and air pressure are both about 1%. If the atomic cloud is half a meter away from the retro-reflection mirror as in our experiment, the effective phase drift of the superlattice is

$$\Delta\phi_{air}/2\pi = \frac{L \times \Delta n_{air}}{\lambda_{532}/2} \times \text{relative change} \quad (4.13)$$

$$= \frac{0.5 \times 4 \times 10^{-6}}{0.266 \times 10^{-6}} \times 1\% \quad (4.14)$$

$$\simeq 10\% \quad (4.15)$$

which is not completely negligible.

For a temperature stabilized environment, such as in the enclosure system that we have, and in a day with steady weather, the superlattice phase should be stable for a full day of experiment running, as demonstrated in the superlattice phase calibration section later. However, because these drifts accumulate over time, we cannot expect the superlattice phase to be stable more than a week. In practice, we have not seen severe drifts in the superlattice phase in our experiments. In case the drifts from air temperature and pressure become a problem, it can be reduced by shortening the distance between the retro-reflection mirror and the chamber.

Finally, let's consider drifts from thermal effects on the glass plate and viewports. The thermal expansion coefficient is about  $10 \times 10^{-6} K^{-1}$  in standard glasses. The

phase drift of the superlattice due to thermal expansions in glass is

$$\Delta\phi_{glass}/2\pi = \frac{\alpha D \times \Delta T \times \Delta n_{glass}}{\lambda_{532}/2} \quad (4.16)$$

$$= \frac{10 \times 10^{-6} \times 10^{-2} \times 1 \times 0.013}{0.266 \times 10^{-6}} \quad (4.17)$$

$$\simeq 0.5\% \quad (4.18)$$

which is small and negligible.

### 4.2.3 Considerations for the Raman beams

Raman beams are used to drive the spin-orbit coupling between the double wells. In our experiment, one beam of the Raman pair is along the lattice direction to guarantee a non-vanishing coupling matrix element, due to the fact that eigenstates are always orthogonal! The other beam of the Raman pair is perpendicular to the lattice, which provides the transverse momentum kick.

There are a few special considerations for the Raman beam preparation. First of all, the Raman beams are split after the same optical fiber on the experimental table. The motivation is to minimize relative frequency noise of the two beams, because any fluctuation in the path length inside the fiber is now common mode. Second, each of the Raman beams is going through a double-pass AOM for switching on/off and intensity stabilization. This is intended to minimize the pointing shifts while scanning the Raman frequency. Lastly, to be able to look at the frequency spectrum and make sure our Raman coupling is narrow and at signal frequency, we have built up a beat note monitor between the Raman beams for diagnosis.

Initially, our Raman beams were set up for the synthetic gauge fields in optical lattices experiment, as one beam was along the vertical direction, in which a strong and uniform tilt would be created, and the other was horizontal to provide transverse momentum kick and consequent vector potential. Later after we turned to the spin-orbit coupling experiment in superlattices, this vertical Raman beam has been moved to the horizontal plane for mechanical stability and detection convenience.

For the experiments that have been carried out in this thesis, Raman beams of 1064 nm light and in orthogonal directions are used. The choice of Raman beams is not restricted to this particular configuration at all, as long as they are far detuned from the atomic transition, have the correct frequency offset, and provide a non-vanishing coupling matrix element. As we will see later, in certain situations, a different Raman configuration (both in wavelength and geometry) could come in handy for the state preparation and experimental detection.

#### **4.2.4 Experimental layout**

To give the reader a graphic view about the geometry and layout of the optical setup in our superlattice experiment, a schematic drawing looking from the top is shown in Fig. 4-6,

The green and IR beams are combined along one of the 45-degree axes, and then simultaneously retro-reflected to make the superlattice. A glass plate is inserted into the retro-path to control the phase of the superlattice. A pair of IR beams with a small frequency offset are used for the Raman coupling, with one along the superlattice and the other perpendicular to it.

Another way to see the geometry of beams in action is to look at the corresponding diffraction patterns. This is illustrated in Fig. 4-7, as a fun aspect of the experiment.

### **4.3 Experimental Characterization and Calibration of a Superlattice**

In this section, we will experimentally characterize the superlattice, including testing our experimental control of the superlattice phase, and probing the band structure via amplitude modulation (AM) and two-photon Raman process (Raman).

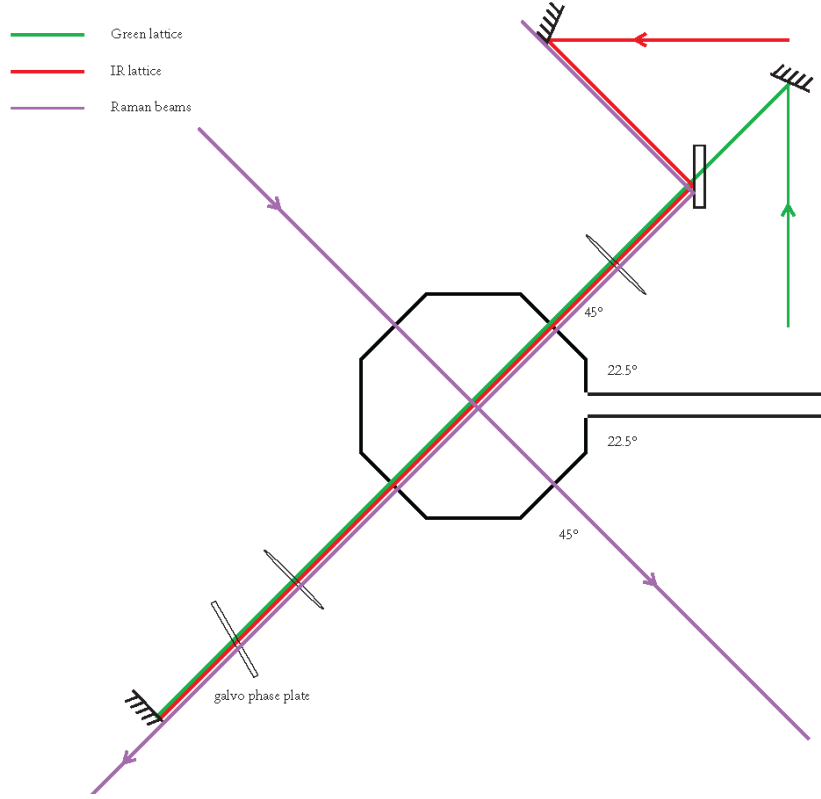


Figure 4-6: Experimental schematics of the superlattice experiment viewing from the top. The green beam is sent collinearly with the IR beam through the atomic cloud, and then both are retro-reflected to create a superlattice. A glass plate is mounted on a galvo in the retro-path to control the superlattice phase. One of the Raman beams is sent along with the superlattice, and the other is perpendicular to the superlattice, both without retro-reflection.

### 4.3.1 Superlattice band structure

The potential of a one-dimensional superlattice can be written as

$$U(x) = -\frac{V_R}{2} \cos(2k_R x) - \frac{V_G}{2} \cos(2k_G x + \phi_0) \quad (4.19)$$

where  $k_R$ ,  $k_G$  are the wavenumbers of 1064 nm and 532 nm light, and  $V_R$ ,  $V_G$  are the corresponding lattice depths.

The natural units for the physical quantities of interest in a superlattice are listed in table 4.2. Please note that  $k_L = \pi/d$  is also the size of the Brillouin zone in a 1064 nm lattice.

With all physical quantities in their natural units, the single-particle Hamiltonian

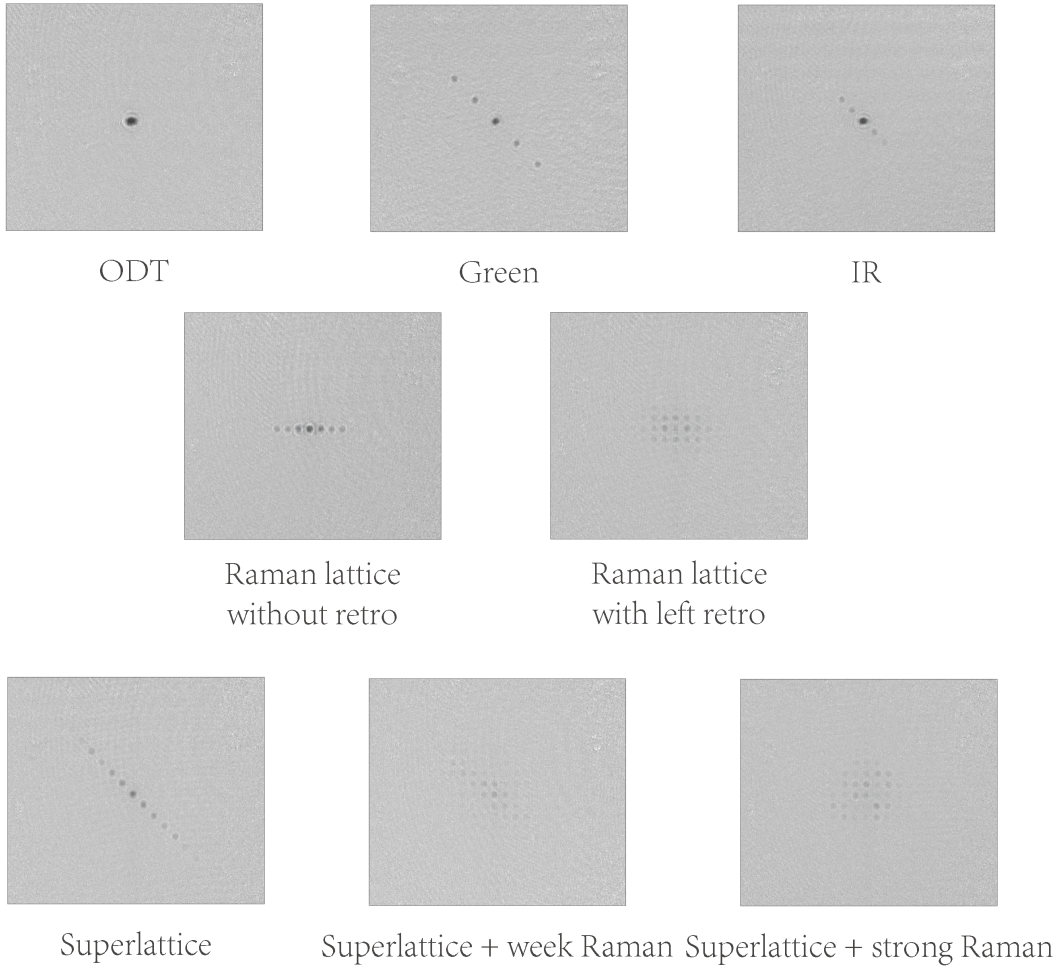


Figure 4-7: The diffraction patterns for relevant beams in the superlattice experiment. These images are taken by looking at the cloud from the bottom. To stay consistent with the schematics in Fig. 4-6, these images need to be flipped vertically due to the mirrors in the imaging path.

in the superlattice is simply

$$H_0 = -\nabla^2 - \frac{V_R}{2} \cos(2x) - \frac{V_G}{2} \cos(4x + \phi) \quad (4.20)$$

The band structure calculation for a superlattice is a straightforward extension of the solid-state textbook problem that we've derived earlier in section 3.2.1. The only difference is that, in addition to the IR component in  $\cos(2k_L x)$  which couples states with momentum transfer  $\pm 2k_L$ , there is also a green component  $\cos(4k_L x + \phi)$  which couples states with momentum transfer  $\pm 4k_L$ .

Physical Quantity	Unit	Meaning
Momentum	$k_L = k_R = 2\pi/\lambda_R$	1064 nm wavenumber
Energy	$E_L = E_R = \frac{\hbar^2 k_L^2}{2m}$	1064 nm recoil energy
Distance	$d/\pi = 1/k_L$	1064 nm lattice spacing

Table 4.2: The natural units of the physical quantities in a 532/1064 nm superlattice.

The superlattice band structure as a function of the phases is shown in Fig. 4-8. In the case of very deep symmetric double wells, the lowest two bands correspond to the symmetric and anti-symmetric states, and they are splitted by the tunneling  $J$  between the double wells. As the phase is tuned away from the symmetric point, an energy offset is created between the left and right wells, and the lowest two bands are separated, roughly speaking, by this offset  $\Delta$ .

Quasi-momentum states of each band in a superlattice can be calculated as well. For example, quasi-momentum states at  $q = k_L$  in the lowest three bands are shown in Fig. 4-9. Please notice that for a superlattice without IR component, there is no gap opened at  $q = k_L$ , therefore the lowest three bands in a green lattice shown on the top right correspond to the 1st, 3rd and 5th lowest band in the other superlattice configurations.

They are the final states when we couple the ground state into higher bands via a Raman process, and the Raman beams provide a momentum transfer  $k_L$  along the superlattice as in our experiment. The momentum distribution of the final state can be measured in the time-of-flight images and is used to identify the band index of the final state.

### 4.3.2 Calibration and dynamical control of the superlattice phase

To have the full control of the superlattice in our experiments, we need to calibrate and dial in the superlattice phase anywhere between 0 and  $2\pi$ . In addition, it would very helpful to be able to dynamically change the phase during the experimental sequence. Finally, the superlattice phase needs to be stable against long-term ambient drifts.

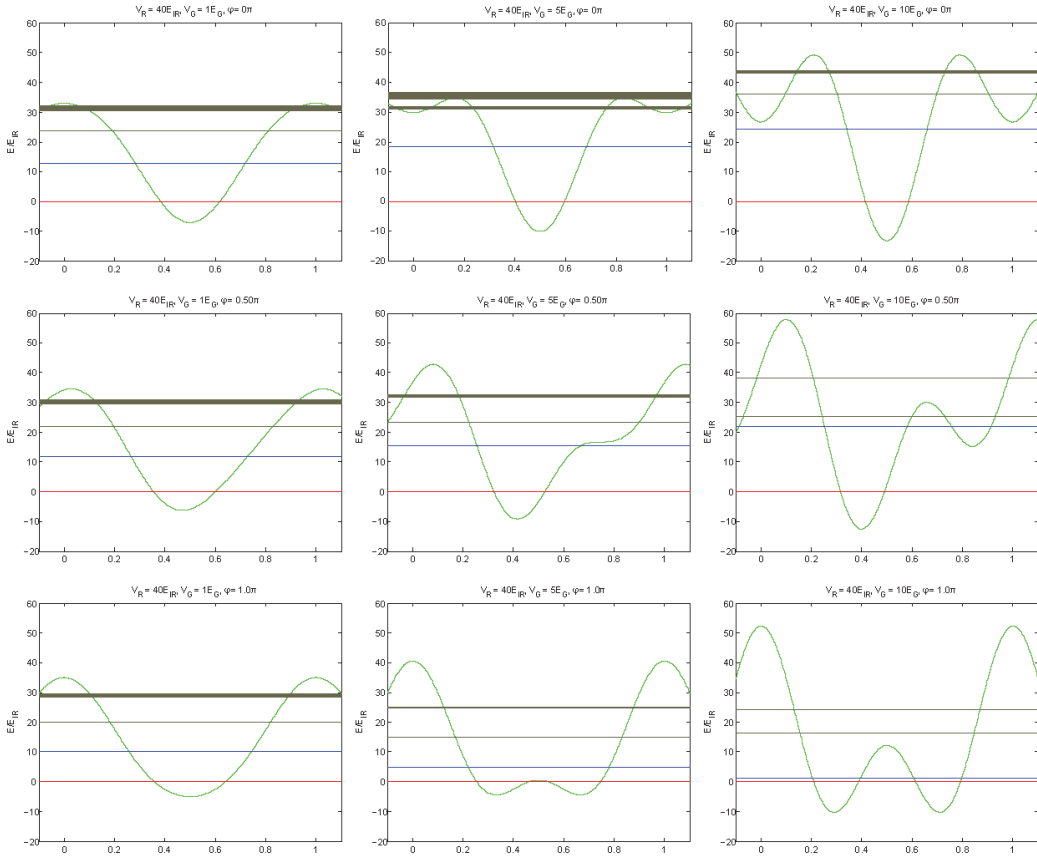


Figure 4-8: The band structure of the superlattice under various conditions, with the lowest two bands shown in red and blue. The relative phase  $\phi$  between the IR and green lattices are 0 for the top row,  $\pi/2$  for the middle row and  $\pi$  for the bottom row. The green lattice becomes deeper from left to right, while the IR lattice depth is kept constant. The symmetric point of the superlattice corresponds to the bottom row.

We will discuss all of these aspects in the following.

### Superlattice phase calibration

The phase of the superlattice can be read out in the time-of-flight image. When the phase is at a symmetric point, the superlattice is an array of symmetric double wells, and the first-order peaks will disappear due to destructive interference in the double-well structure factor. The other phases of the superlattice can be linearly interpolated from the nearest symmetric points, using either the glass plate angle set point or the AOM frequency.

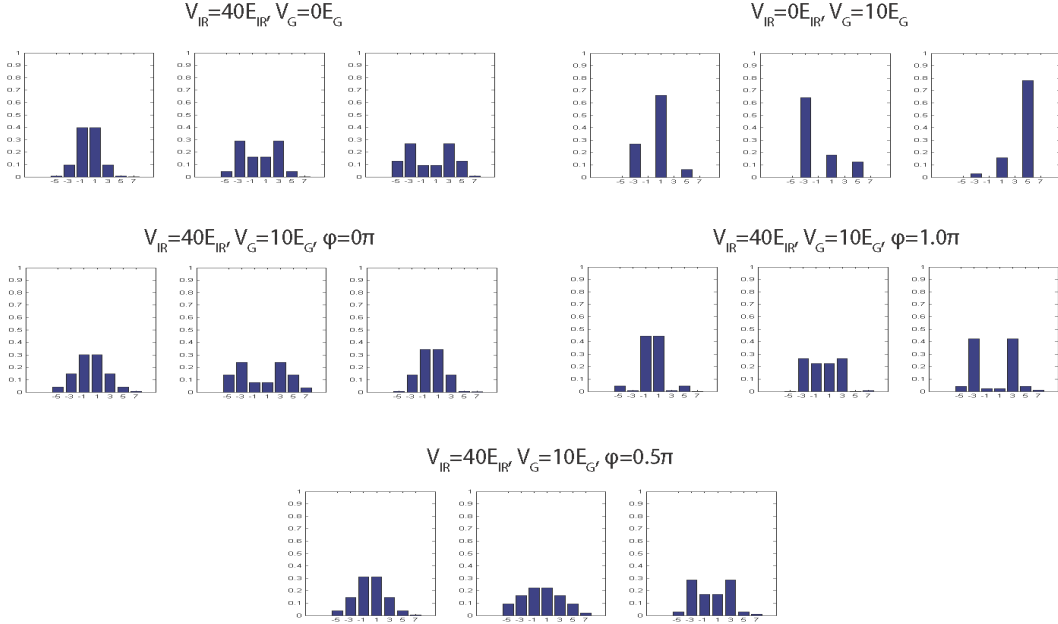


Figure 4-9: The momentum components of quasi-momentum states at  $p = +k_L$  for the lowest three bands in a superlattice. The units on the horizontal axis are the IR wavenumber  $k_L$ . This figure also predicts the time-of-flight images of the final states in Fig. 4-16, when we couple the ground state into higher bands via a Raman process.

The time-of-flight images can be taken by adiabatically ramping up a superlattice, or by applying a superlattice pulse and then looking at the diffraction in time-of-flight. We find that in practice the second method usually has better contrast and robustness, possibly because of a much shorter interaction time (a few  $\mu s$ ).

A typical superlattice phase calibration series is shown in Fig. 4-10. The superlattice is symmetric when first-order peaks are minimal in the time-of-flight diffraction.

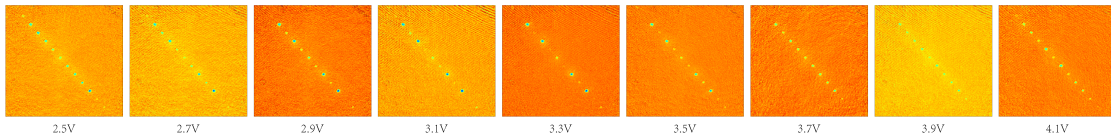


Figure 4-10: Calibration of the superlattice phase via diffraction in time-of-flight. The image captions are the set points for the glass plate, which is linear in the superlattice phase. The symmetric point in the superlattice phase shows minimal first-order peaks, which is at 3.3V in this series.

## Load BEC into a superlattice

A pure condensate can be loaded into a superlattice by ramping up the green and IR lattices simultaneously to reach the desired values. When both lattice beams are well-aligned, we are able to load the condensate into a superlattice with various presetted phases in 100 *ms* without noticeable heating, shown Fig. 4-11. When the lattice beams are slightly misaligned from the dipole trap (especially for the repulsive green lattice beam), the sample may experience sloshing motion in the trap. In this case, a slower ramp-up in a few hundred milliseconds can prevent the sample from heating up, and sometimes additional confinement may be necessary to keep the cloud in the trap.

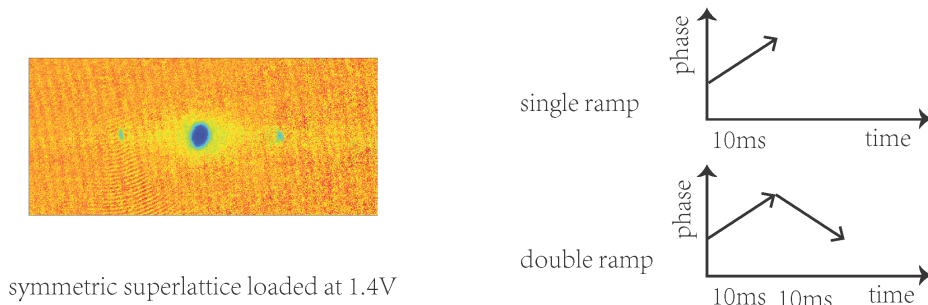


Figure 4-11: Experimental sequence for the dynamical control on superlattice phase. Left: a condensate is loaded into a symmetric superlattice with a static phase. Right: The experimental sequence for a single ramp and a double ramp in the slow dynamical phase control experiment.

## Slow dynamical phase control using glass plate

To test our dynamical control of the superlattice phase using a glass plate, we first load a condensate into a symmetric superlattice, and then change its phase in either a single ramp or a double ramp with the galvo rotation, illustrated in Fig. 4-11. These phase ramps are done in tens of milliseconds, which is slow compared to the estimated inter-well tunneling about kilohertz, and enough to keep the condensate in the ground state. Time-of-flight images after the one-way ramp show the corresponding ground state

in a tilted double-wells, and round-trip images confirm that the process is adiabatic and without severe heating.

It's important to point out that, as we rotate the glass plate to change the phase, the superlattice itself has an overall motion of hundreds of lattice constant, dragging the condensate along. This effect may require even slower speed in the phase ramp to maintain adiabaticity. Therefore, even though the galvo has the capability of rotating our plate within a millisecond, the glass plate phase shifter scheme is limited for only static and slow dynamical control of the superlattice phase.

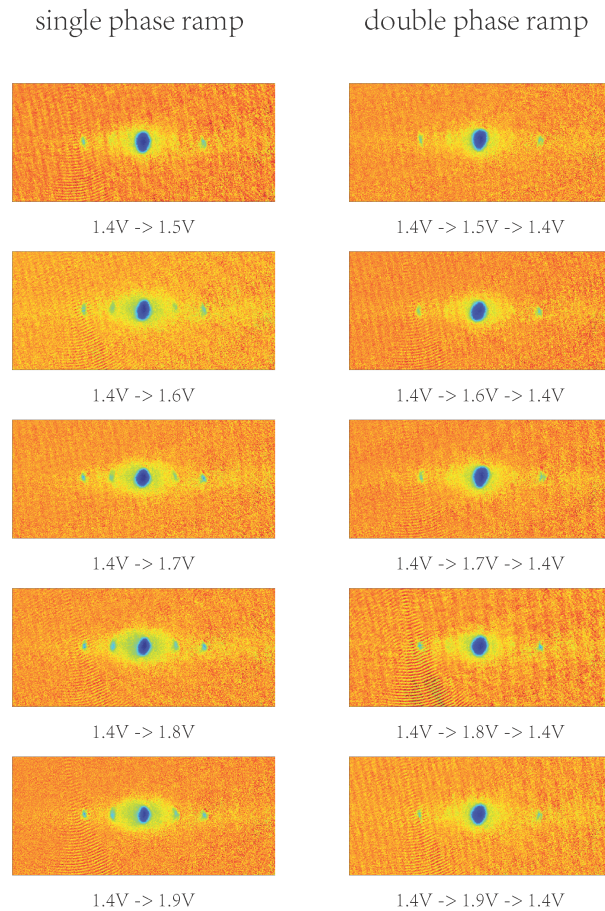


Figure 4-12: The dynamical control of the superlattice phase using a glass plate. The time-of-flight images are shown on the left after a one-way phase ramp, and on the right after a round-trip phase ramp in the superlattice. These phase ramps are slow enough so that the condensate remains in the ground state of the superlattice.

## Fast dynamical phase control using AOM

The superlattice phase can also be tuned by changing one of the lattice frequencies, which can go as fast as a microsecond, and doesn't come with the unwanted motion of the superlattice. As discussed in earlier sections, changing IR frequency is favorable compared to green, because it requires a smaller frequency shift, and keeps the atomic wavefunction more stationary. By suddenly switching the IR frequency, we freeze the atomic population in each well between two superlattice phases, critical for the 50/50 sample preparation in the spin-orbit coupling experiment.

In our experiment, a double-passed AOM is used to shift the frequency of the seed light for the Nufern fiber amplifier. In this way, we only need to shift the frequency with a low power beam, and the double-pass scheme maintains the fiber coupling efficiency. The RF frequency and power for this AOM need to be carefully chosen so that the power of the seed light into the amplifier stays constant before and after the frequency switch, otherwise the fiber amplifier may complain and shut down itself from a built-in safety feature. Experimentally, we have observed a shift of the phase symmetric point by  $0.7V$  in the galvo set point when we shift the IR frequency by 40 MHz, consistent with our estimates in section 4.2.2.

## Long-term superlattice phase drifts

One could characterize the long-term phase drifts by measuring the superlattice symmetric point over time. In Fig. 4-13, we've located a symmetric point by the time-of-flight diffraction, and monitored its position over half a day with a half-hour interval.

In the earlier calibration, the period of the superlattice phase between neighboring symmetric configurations is measured to be at  $2.6 \pm 0.2 V$  in the unit of glass plate set point. Long-term drifts of the superlattice phase is measured to be within 10 percent of the full period over six consecutive hours. This upper bound is mainly limited by the measurement error bar of locating the symmetric phase. In practice, we have not experienced severe phase drifts in the superlattice, although as a routine we'll check and calibrate the superlattice phase everytime we start the experiment.

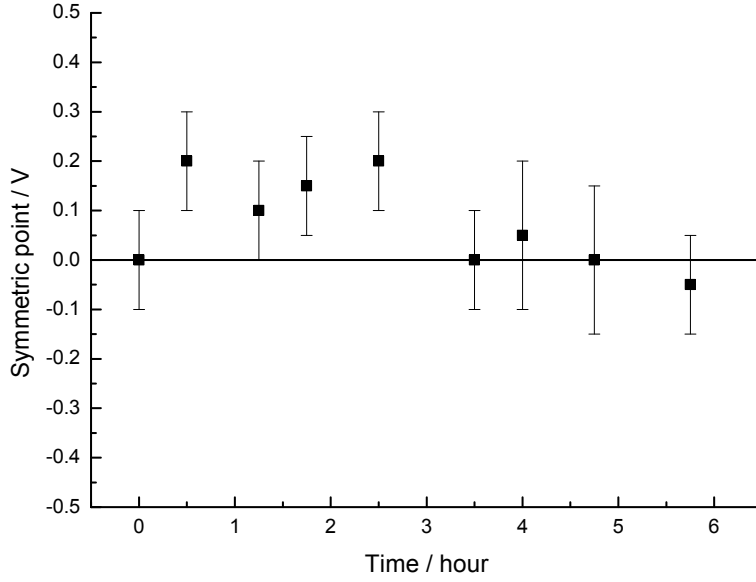


Figure 4-13: The measurement of the long-term drifts in the superlattice phase. The symmetric point of the superlattice phase was monitored over six consecutive hours. The long-term drifts in the superlattice phase are estimated to be within 10%, mainly limited by our phase measurement error bar.

### 4.3.3 Interband population transfer and band mapping

The band structure of the superlattice can be probed by coupling the condensate from the ground state into higher bands. Understanding the band structure is essential for lattice diagnosis, the study of orbit physics and excited state dynamics, and sample preparation for quantum simulation with pseudospin states in superlattices as well. In this section, we'll develop the techniques for transferring atoms into higher bands, as well as for measuring the population in each band afterwards.

Population transfer into higher bands is achieved by amplitude modulating the lattice, or by switching on a pair of Raman beams through the two-photon process. Amplitude modulation preserves the quasi-momentum of the initial state, while Raman coupling may shift the quasi-momentum depending on the wavelength and beam geometry. In our experiment with orthogonal 1064 nm beams, the Raman coupling shifts quasi-momentum by  $k_L$ , and also provides a momentum transfer of  $k_L$  perpendicular to the lattice, illustrated in Fig. 4-15.

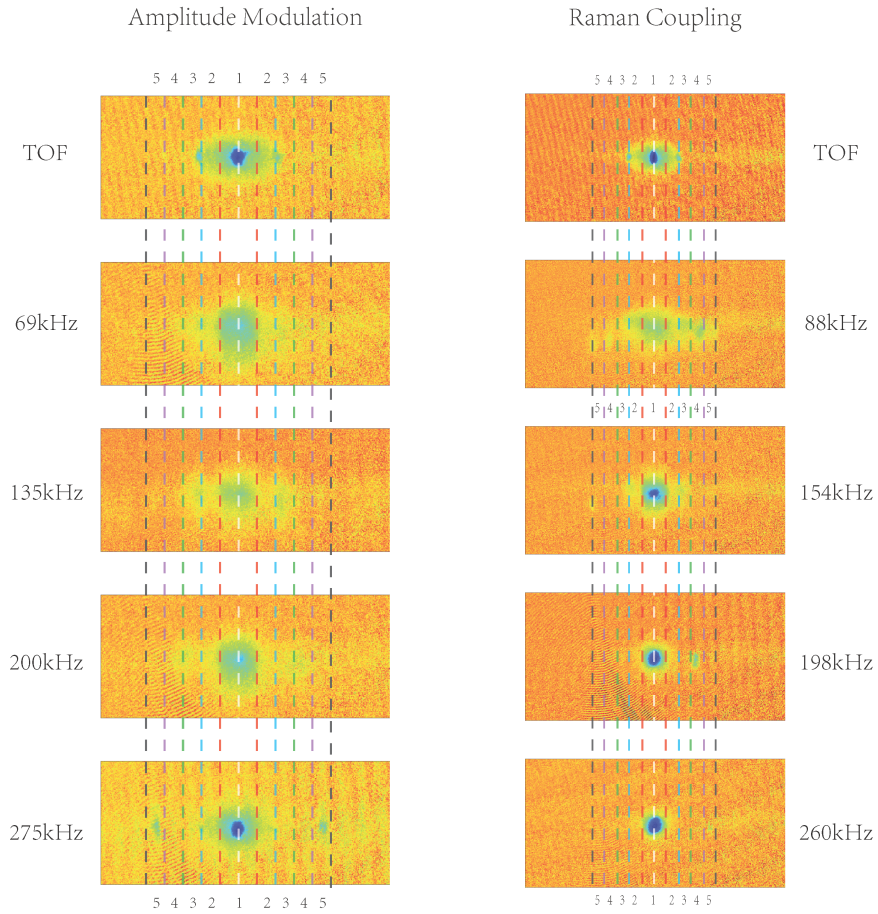


Figure 4-14: Interband coupling in a 1064 nm lattice via amplitude modulation and Raman process. Population in each band is individually read out with band mapping, as the bands are resolved with spatially separated Brillouin zones in the time-of-flight images. The image captions are the corresponding resonance frequencies.

Population in different bands could be directly read out by ramping down the lattice and subsequently taking the time-of-flight image, a technique commonly known as band mapping. During this slow ramp, quasi-momentum states in different bands are mapped into the corresponding real-momentum states in the free-particle dispersion relation in an adiabatic connection process, and population in each band shows up in individual Brillouin zone spatially separated in the time-of-flight image. Population in higher bands transferred via Raman coupling can also be identified in time-of-flight without band mapping, as they are spatially shifted from the ground state due to the perpendicular momentum transfer, and show different momentum distribution. We

will demonstrate both methods in the following.

For amplitude modulation, we are modulating the RF power of the AOM. The modulation depth is usually around 30% to balance the strong coupling and excessive heating, and the duration is about 100 milliseconds. For Raman coupling, its coupling strength is proportional to the depth of the moving Raman lattice, which is usually chosen to be a few lattice recoils, and the pulse duration is less than a millisecond.

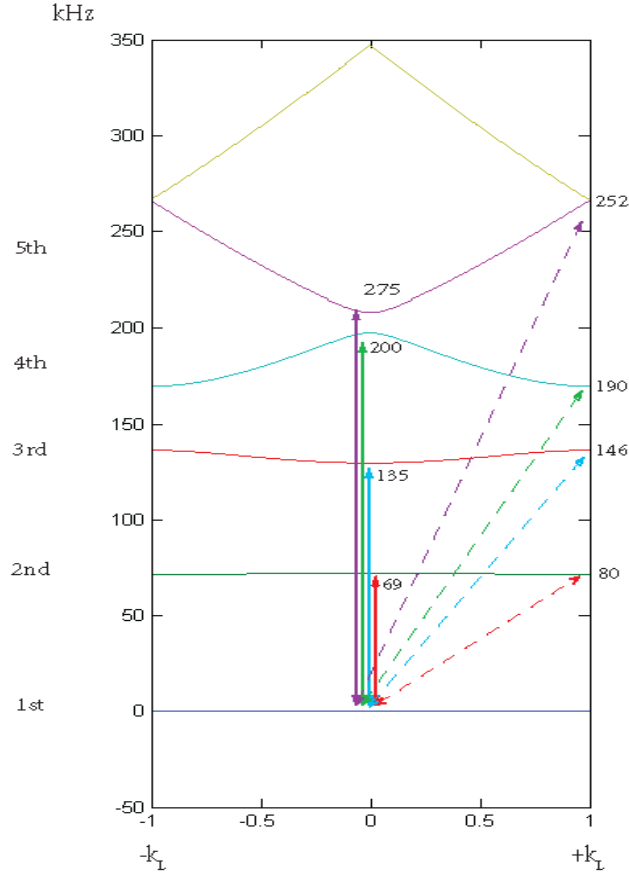


Figure 4-15: Interband coupling resonances and the corresponding band structure in a 1064 nm lattice. The solid lines show the AM resonances, while the dotted lines show the Raman resonances. The Raman resonance frequencies have been subtracted by a recoil energy  $E_L = 7.6$  kHz for the transverse momentum transfer. Within experimental precision, these measured resonances are in agreement with the band structure of an IR lattice of  $27E_L$ , calibrated independently via Kapitza-Dirac diffraction, except for the AM resonance of the 5th band.

In band mapping, the lattices are simultaneously slowly ramped down. In practice, we find out that the maximum speed of this ramp so that the condensate could still

follow the adiabatic passage is around  $0.5\text{ ms}$  for the green lattice, and around  $2\text{ ms}$  for the IR lattice. A ramp-down faster than that might result in partial projection onto the higher bands and create a false signal in the band mapping detection. The time-of-flight images of a condensate in the ground state are used to calibrate the size of the Brillouin zone in band mapping.

First, we've tested the population transfer and band mapping in a  $1064\text{ nm}$  lattice, shown in Fig. 4-14. Population transfers up to the 5th band have been identified, and the resonance frequencies are consistent with the case of a lattice depth of  $27 E_L$ , after taking into account the additional recoil energy due to the perpendicular momentum transfer, illustrated in Fig. 4-15. This inferred lattice depth is in agreement with our independent calibration using Kapitza-Dirac diffraction.

There are a few findings and comments regarding this experiment. First of all, in theory, amplitude modulation only couples the ground state into higher bands with the same parity, which in our notation are the odd bands in Fig. 4-15. The fact that we seem to see coupling into even bands might be due to deviations from the ideal case, or simply heating from the modulation. Second, we find that AM coupling is usually broader than  $5\text{ kHz}$ , while Raman coupling is about a couple of kilohertz wide. Third, Raman couplings usually transfer population with much less heating compared to AM couplings. Finally, the lifetime of higher band population is about  $10\text{ ms}$  in the  $1064\text{ nm}$  lattice, as the atoms collide and rapidly decay into the ground state.

The band of the final state in the Raman coupling scheme can also be identified in the time-of-flight images. As shown in Fig. 4-16, the Raman transferred population in the higher bands is shifted in the transverse direction, and has shown distinguishable momentum distributions. This separation in time-of-flight on lattice bands is possible only with the assistance of perpendicular Raman momentum transfer. Time-of-flight detection relies on analyzing the relative strength of the momentum peaks, therefore it is less direct and robust compared to the band mapping scheme. However, it doesn't require additional time for the slow ramp as in band mapping, and is useful when the lifetime of the final state is limited.

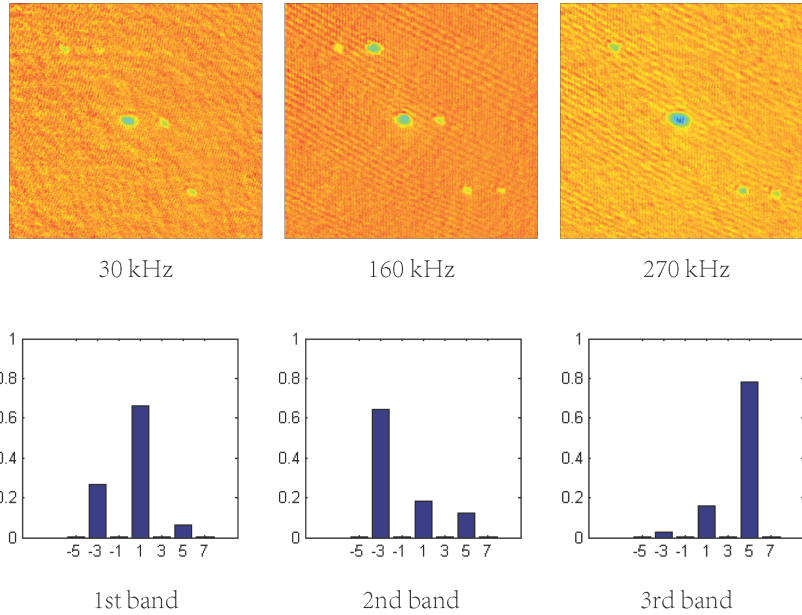


Figure 4-16: Raman coupling into higher bands with time-of-flight images in a green lattice. The final states of the Raman coupling are offset to the upper-right diagonally because of the perpendicular momentum transfer. In this experiment, we demonstrated the distinguishable momentum distributions of quasi-momentum states at  $q = k_L$  for the lowest three bands in a green lattice. The measured resonance frequencies indicate the lattice depth around  $10E_G$ .

## 4.4 Theory of Spin-Orbit Coupling in a Superlattice

In this chapter, we will develop the theory for a spin-orbit coupled condensate in the superlattice. First, we will discuss the Raman couplings in superlattices, and derive the single-particle Hamiltonian with spin-orbit coupling in this system. Then we will compare the relative strength of the spin-orbit coupling which couples states between the wells, and onsite coupling with couples states within the same well. The desirable experimental parameters are also estimated. Finally, we discuss the phase transition from the miscible stripe phase to the immiscible separated phase for the interacting spin-orbit coupled system.

### 4.4.1 Single-particle spin-orbit coupling Hamiltonian

In this section, we derive the Raman coupling contributions for a double-well system. We will focus on only the single-particle physics in this section.

#### Raman couplings in a double-well system

First of all, let's consider the general case where we apply a pair of Raman beams in the superlattice, and discuss the possible coupling processes.

In the tight-binding approximation, the basis functions are the localized Wannier states labelled as  $|i_m, k\rangle$ , where  $i$  can be left  $a$  or right  $b$  in the double well, representing our pseudospin-1/2 states,  $m$  is the superlattice double-well unit-cell index, and  $k$  is the transverse momentum. If the coupling between double-wells can be neglected for now and only a single double-well is considered, index  $m$  is omitted.

The two-photon Raman field can be written as  $\Omega e^{ik_x x + ik_y y} e^{-i\delta t}$ . The spatial phase component  $e^{ik_y y}$  provides the transverse momentum kick  $k_y$ , while component  $e^{ik_x x}$  is critical to maintain a non-vanishing matrix element for nearest-neighbor couplings. As the Wannier states are localized and vanishing after a few lattice sites, all other couplings are negligible except the onsite and nearest-neighbor couplings,

$$H_{\text{Raman}} = \Gamma e^{-i\delta t} |a_m, k + k_L\rangle \langle a_m, k| + i\Gamma e^{-i\delta t} |b_m, k + k_L\rangle \langle b_m, k| \quad (4.21)$$

$$+ K e^{-i\delta t} |b_m, k + k_L\rangle \langle a_m, k| + h.c. \quad (4.22)$$

where  $\Gamma$  is the strength of coupling between states in the same well, as we will call it the ‘‘onsite coupling’’; while  $K$  is the strength of coupling between states in different wells, as we will call it the ‘‘spin-orbit coupling’’.  $K$  is complex in this notation, the phase is  $3\pi/4$ , from the propagating phase of the Raman coupling,

In the case where an energy offset  $\Delta$  is applied between the double wells to make well-defined pseudospins, first-order perturbation theory gives the onsite coupling strength  $\Gamma \simeq \Omega$ , and the spin-orbit coupling strength  $K \simeq J\Omega/\Delta$ .

If we start with a coherent equal superposition in the double-well  $|a, 0\rangle + e^{-i\Delta t} |b, 0\rangle$ , and then slowly ramp up the Raman beams, this state will be adiabatically connected

to the following state (in the perturbative limit),

$$|S\rangle = |a, 0\rangle + e^{-i\Delta t} |b, 0\rangle \quad (4.23)$$

$$+ \frac{\Gamma}{\delta - E_L} e^{-i\delta t} |a, k_L\rangle - \frac{\Gamma^*}{\delta + E_L} e^{+i\delta t} |a, -k_L\rangle \quad (4.24)$$

$$+ \frac{i\Gamma}{\delta - E_L} e^{-i(\Delta+\delta)t} |b, k_L\rangle + \frac{i\Gamma^*}{\delta + E_L} e^{+i(\delta-\Delta)t} |b, -k_L\rangle \quad (4.25)$$

$$+ \frac{K^*}{\Delta + \delta - E_L} e^{-i(\Delta+\delta)t} |a, k_L\rangle + \frac{K^*}{\Delta - \delta - E_L} e^{+i(\delta-\Delta)t} |a, -k_L\rangle \quad (4.26)$$

$$+ \frac{K}{-\Delta + \delta - E_L} e^{-i\delta t} |b, k_L\rangle - \frac{K}{\Delta + \delta + E_L} e^{+i\delta t} |b, -k_L\rangle \quad (4.27)$$

where Eq. 4.24 and 4.25 are the onsite coupling contributions, and Eq. 4.26 and 4.27 are the spin-orbit couplings and their counter-rotating terms.

When the Raman detuning  $\delta$  is set to be equal to the double well offset  $\Delta$ ,

$$|S\rangle = |a, 0\rangle - \frac{K^*}{E_L} |a, -k_L\rangle + e^{-i\Delta t} |b, 0\rangle - \frac{K}{E_L} e^{-i\Delta t} |b, k_L\rangle \quad (4.28)$$

$$+ \frac{\Gamma}{\Delta - E_L} e^{-i\Delta t} |a, k_L\rangle - \frac{\Gamma^*}{\Delta + E_L} e^{+i\Delta t} |a, -k_L\rangle \quad (4.29)$$

$$+ \frac{i\Gamma}{\Delta - E_L} e^{-2i\Delta t} |b, k_L\rangle + \frac{i\Gamma^*}{\Delta + E_L} |b, -k_L\rangle \quad (4.30)$$

$$+ \frac{K^*}{2\Delta - E_L} e^{-2i\Delta t} |a, k_L\rangle - \frac{K}{2\Delta + E_L} e^{+i\Delta t} |b, -k_L\rangle \quad (4.31)$$

In this equation, Eq. 4.28 is the spin-orbit coupling state, which shows the stationary stripe phase. Eq. 4.29 and 4.30 are the onsite coupling states in each well, which give a time-dependent density modulation moving with the Raman beams. The last terms in Eq. 4.31 are the counter-rotating contributions from the spin-orbit coupling.

As we will see, our experiment is usually done in the regime where  $\Delta$  is about an order of magnitude bigger than the recoil energy  $E_L$ , therefore the effects from the counter-rotating terms are negligible. The strength and effects of the onsite couplings will be discussed in section 4.4.2.

## Single-particle spin-orbit coupling Hamiltonian

When the Raman detuning  $\delta$  is very close to double-well offset  $\Delta$ , one can make the rotating-wave approximation, and neglect the onsite couplings. The Hamiltonian of the spin-orbit coupled spin-1/2 system in the lab frame is

$$H_0 = \begin{pmatrix} \frac{\hbar^2 k^2}{2m} & K^* e^{-ik_L y + i\delta t} \\ K e^{ik_L y - i\delta t} & \frac{\hbar^2 k^2}{2m} + \hbar\Delta \end{pmatrix} \quad (4.32)$$

after applying a temporal and spatial unitary transformation, the effective Hamiltonian in the transverse direction is

$$H_{\text{eff}} = \frac{\hbar^2 (k + k_L/2 \cdot \sigma_z)^2}{2m} + K\sigma_x + \delta_0\sigma_z \quad (4.33)$$

where  $\delta_0 = \delta - \Delta$  is the offset of the pseudospin-1/2 in the new frame.

## Effects of the couplings between double-wells

In the last two sections, we've only considered the Raman couplings within a double-well, as the normal tunnelings are strongly suppressed by the energy offset. In this section, we'll discuss the effects of the Raman couplings between neighboring double-wells, as well as the resonant normal tunnelings between wells of the same kind.

Firstly, the resonant tunneling between wells of the same kind in the neighboring double-wells, which is expected to be small, is maintaining the relative phases between double-wells and therefore the global coherence. This is critical for both the time-of-flight interference detection and the Bragg scattering detection. As we'll see in the experimental section, the upper-well states, which correspond to the second band, have the ground state at quasi-momentum  $q = k_L$ , rather than  $q = 0$ . This insight, which in retrospect totally makes sense, came initially as a little surprise, and would completely change the expected signals in our detection for the spin-orbit coupling.

Therefore, when we prepare a coherent superposition with equal population in the

double-wells, the initial ground state can be written as

$$|S_m\rangle = |a_m, 0\rangle + (-1)^m e^{-i\Delta t} |b_m, 0\rangle \quad (4.34)$$

Secondly, let's also consider the propagating phase of Raman couplings, as well as the effects of the Raman couplings between double-wells. The latter is written as

$$H_{\text{Raman}} = \sum_m (-1)^m [K_2 e^{-i\delta t} |b_{m-1}, k + k_L\rangle \langle a_m, k| + h.c.] \quad (4.35)$$

where  $K_2$  is the coupling strength between states in neighboring wells but from different unit cells. Again, this coupling strength is approximately  $K_2 \simeq J'\Omega/\Delta$ , and  $J'$  is the normal tunneling corresponding to the barrier between neighboring double-wells, which could be much higher than the barrier within a double-well. Therefore, in most experimental configurations where the IR lattice is not very weak,  $K_2$  is much weaker than  $K$ .

If one carefully counts the phases of the Raman couplings, and keep the spin-orbit coupling between double-wells, the full ground state that is adiabatically connected to our initial state, in the presence of Raman couplings at balanced spin-orbit coupling condition  $\delta = \Delta$ , is

$$|S'_m\rangle = |a_m, 0\rangle + (-1)^m e^{-i\Delta t} |b_m, 0\rangle \quad (4.36)$$

$$- \frac{K^*}{E_L} |a_m, -k_L\rangle - (-1)^m \frac{K}{E_L} e^{-i\Delta t} |b_m, k_L\rangle \quad (4.37)$$

$$+ \frac{K_2^*}{E_L} |a_m, -k_L\rangle + (-1)^m \frac{K_2}{E_L} e^{-i\Delta t} |b_m, k_L\rangle \quad (4.38)$$

$$+ \frac{\Gamma}{\Delta - E_L} (-1)^m e^{-i\Delta t} |a_m, k_L\rangle - \frac{\Gamma^*}{\Delta + E_L} (-1)^m e^{+i\Delta t} |a_m, -k_L\rangle \quad (4.39)$$

$$+ \frac{i\Gamma}{\Delta - E_L} e^{-2i\Delta t} |b_m, k_L\rangle + \frac{i\Gamma^*}{\Delta + E_L} |b_m, -k_L\rangle \quad (4.40)$$

where  $K$  and  $K_2$  are complex if we assume  $\Gamma$  is real in this notation, and have phase of  $\pi/4$  and  $-\pi/4$  in approximation. This complete wavefunction contains the stationary stripes from the spin-orbit coupling as well as the moving density modulation from the

onsite couplings, and is also used to make predictions in the time-of-flight interference measurement.

#### 4.4.2 Spin-orbit coupling and onsite couplings

In this section, we'll discuss the relative strength of spin-orbit coupling and the onsite couplings. The optimal parameters for creating the spin-orbit coupling for experimental detection are also proposed.

First of all, the onsite coupling couples the  $|a, 0\rangle$  and  $|a, \pm k_L\rangle$  states,

$$H_{\text{OC}} = \begin{bmatrix} 0 & \Omega \\ \Omega & \pm\delta + E_R \end{bmatrix}$$

In this case, we have approximated the Rabi frequency as  $\Gamma \simeq \Omega$ . If Raman detuning  $\delta$  is much greater than  $\Omega$ , the onsite coupling in first-order perturbation theory is

$$|a, 0\rangle \pm \frac{\Omega}{\delta} |a, \pm k_L\rangle \quad (4.41)$$

In our experiment, we choose the Raman detuning  $\delta \approx \Delta \sim 50$  kHz, and the Rabi frequency in this case is roughly the Raman lattice depth, which we assume to be around 15 kHz, the amplitude of the onsite component is about 30%, and the corresponding population is around 10 percent.

In contrast, the spin-orbit coupling couples the  $|a, 0\rangle$  and  $|b, \pm k_L\rangle$  states,

$$H_{\text{SOC}} = \begin{bmatrix} 0 & \frac{J}{\Delta}\Omega \\ \frac{J}{\Delta}\Omega & E_R + \Delta - \delta \end{bmatrix}$$

the Rabi frequency in this case is  $J\Omega/\Delta$  due to wavefunction overlap between left and right wells.  $J$  is the normal tunneling rate mainly determined by the barrier between left and right wells, and is about a few kilohertz. Let's say we use a maximum value of  $J$  to boost the spin-orbit coupling signal, which corresponds to a green barrier of

$3E_G \sim 100$  kHz, still large enough to separate the left and right wells,

$$\frac{J}{\Delta}\Omega \sim \frac{3 \text{ kHz} \times 15 \text{ kHz}}{50 \text{ kHz}} \sim 1 \text{ kHz} \quad (4.42)$$

When we set the Raman detuning at the double-well offset  $\delta = \Delta$  for the balanced spin-orbit coupling and the stationary stripes, the spin-orbit coupling in the first-order perturbation theory is

$$|a, 0\rangle - \frac{J\Omega}{\Delta E_R} |b, k_L\rangle \quad (4.43)$$

therefore, the spin-orbit component is about 12% in amplitude and less than a couple of percent in population.

In short, although the Raman-assisted tunneling does provide a finite spin-orbit coupling in the double-wells, it also comes with an unwanted onsite coupling component that is a few times stronger than the spin-orbit coupling in the balanced case.

To demonstrate the Raman-assisted spin-orbit coupling, one could tune the coupling close to the resonance. The lower-to-upper transition has a resonance frequency at  $\delta = \Delta + E_R$ , while the upper-to-lower transition has a resonance frequency at  $\delta = \Delta - E_R$ , therefore we expect to see a significant increase on one side of the Raman-coupled final-state population when the Raman detuning is near one of the resonances. This is what we have seen in experiment that, as we scan the Raman detuning, one side of the Raman-coupled components shows a resonance feature about 1 kHz wide, while the other side does not. However, the stationary stripe phase requires the balanced spin-orbit coupling at  $\delta = \Delta$ . In this regard, a sensitive detection is needed to measure the spin-orbit coupling. One way is to implement the Bragg scattering to detect the stationary density modulation, which is the linear cross term in the amplitude. Another possible way is to look at the time-of-flight interference, not only the total population but also the interference between the spin-orbit coupling component and the onsite coupling component. Both methods will be discussed in the experimental detection section.

### 4.4.3 Quantum phase transition of an interacting spin-orbit coupled condensate

In this section, we will consider a spin-orbit coupled condensate with repulsive interactions. The mean-field Hamiltonian in this system can be written as,

$$H = \begin{pmatrix} \psi_a^* & \psi_b^* \end{pmatrix} H_0 \begin{pmatrix} \psi_a \\ \psi_b \end{pmatrix} + \frac{g_{aa}}{2} |\psi_a|^4 + \frac{g_{bb}}{2} |\psi_b|^4 + g_{ab} |\psi_a|^2 |\psi_b|^2 \quad (4.44)$$

where  $H_0$  is the single-particle spin-orbit coupling Hamiltonian as before,

$$H_0 = \frac{\hbar^2 (k + k_L/2 \cdot \sigma_z)^2}{2m} + K \sigma_x + \delta_0 \sigma_z \quad (4.45)$$

The spin-orbit coupling mixes spin states with different momentum components, as a result, it creates a spatial density modulation and costs kinetic energy. Therefore, for a balanced spin-1/2 system, spin-orbit coupling favors an immiscible state where opposite spins are spatially separated. On the other hand, if the repulsive interaction between different spins is much weaker than the intra-spin counterpart,  $g_{ab} \ll g_{aa}, g_{bb}$ , the excessive interaction energy forces the spins to stay miscible. Therefore, depending on the relative strength of the kinetic energy in the stripes, and the asymmetry in the intra-spin and inter-spin interactions, a quantum phase transition from a stripe phase to a separated phase is predicted for an interacting spin-orbit coupled condensate [38, 39], and the relevant quantum phases are illustrated in Fig. 4-17.

Up to today, the stripe phase, which is related to supersolidity in condensed matter, has not been observed in experiment. In the first spin-orbit coupling experiment with  $^{87}\text{Rb}$  [34], the interaction strength  $g_{aa} \simeq g_{bb} = g$ , and the difference  $(g_{ab} - g)/g$  is less than 1%, therefore the window for detecting the stripe phase is very small, as the system prefers to stay in the separated phase.

In our spin-orbit coupled pseudospin system, the interspin interaction is controlled by the overlap between the states from the left and right wells. In the lowest-order approximation,  $g_{ab} \simeq (J/\Delta)^2 g \leq 0.1g$ . There is a huge mismatch between the intraspin

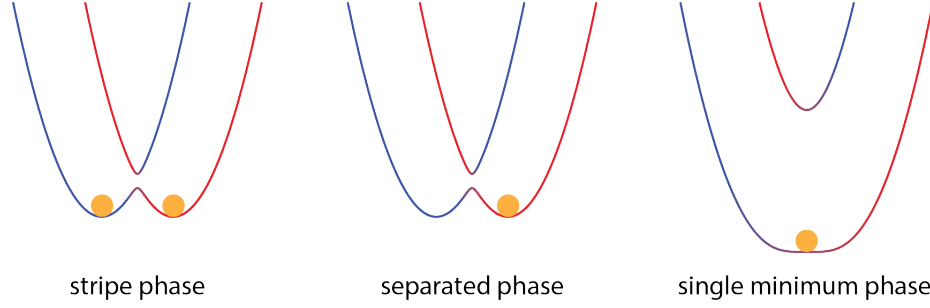


Figure 4-17: Illustration of the quantum phases of an interacting spin-orbit coupled condensate. For the weak couplings, two degenerate minima are created in the single particle dispersion relation. Depending on the interaction, both minima are occupied in the miscible phase with density stripes, or in an immiscible phase, the condensate falls into one of the minima via spontaneous symmetry breaking. For strong couplings, only a single minimum is present in the dispersion relation.

and interspin interactions, and naturally the system prefer to stay in the stripe phase.

Quantitative predictions are made on the phase diagram for an interacting spin-orbit coupled condensate in [39]. For a low density atomic cloud, in which the mean-field energy is less than the recoil of the Raman beams,  $ng < E_L/4$ , as we increase the spin-orbit coupling strength, a first transition from the stripe phase to the separated phase happens at the critical Raman coupling

$$K_c^{1-2} = \frac{E_L}{2} \sqrt{\frac{2\gamma}{1+2\gamma}} \quad (4.46)$$

where  $\gamma = (g - g_{ab})/(g + g_{ab})$  is a dimensionless interaction parameter that measures the asymmetry between interspin and intraspins interactions. In our experiment,  $\gamma \approx 1$  gives the critical Raman coupling of  $K_c^{1-2} \simeq 0.4E_L$ .

When we increase the spin-orbit coupling further, a second phase transition from the separated phase to the single minimum phase happens at

$$K_c^{2-3} = 0.5E_L \quad (4.47)$$

Finally, the phase transition from the stripe phase to the separated phase can be driven by changing the Raman detuning away from the symmetric spin-orbit coupling at  $\delta = \Delta$  as well, although the stripes will be moving in the detuned scenario.

In summary, compared with other spin-orbit coupled systems, the pseudospin-1/2 system in the superlattice has the desirable feature that, the interspin interaction is tunable and could be dramatically different from the intraspin interactions. Therefore, it is an ideal system to prepare and detect the stripe phase.

## 4.5 Experimental Realization of Spin-Orbit Coupling in a Superlattice

### 4.5.1 State preparation in a superlattice

To implement the spin-orbit coupling Hamiltonian and study its phase diagram such as the stripe phase, one needs to prepare the initial quantum state in the double wells. Conceptually, if every step in the preparation is adiabatic, the condensate will remain in the ground state, which is the lower well in an asymmetric double-well. Therefore, some form of the diabatic process, or additional external couplings, are needed in the state preparation for spin-orbit coupling experiment.

#### Fast switching of the superlattice phase

By fast switching the superlattice phase and changing its configuration in a timescale much faster than the double-well tunneling, the atomic wavefunction is frozen in each well. However, special care needs to be taken to make sure that there'll be no residual overall motion of the superlattice so that the atomic wavefunction is kept stationary.

Even with a fairly high barrier, the tunneling rate is still on the order of hundred Hertz between the double-well, which means we need to switch the superlattice phase in less than a millisecond. It is very challenging for mechanical switches like the glass plate. Furthermore, in the glass plate scheme, the relative shift of the two lattices is about just one percent of the overall shift of the superlattice. Assuming the atomic cloud will not be able to follow the overall motion in such a short timescale, it creates dragging and undefined matching of the atomic wavefunction.

In contrast, fast switching of the lattice frequency won't have the same problem.

As discussed earlier, switching the IR frequency keeps the atomic wavefunction more stationary, and it could be done far less than a millisecond. We have been using this scheme to prepare initial states with balanced population, or 100-percent population in the upper-well, in an asymmetric double-well.

### **Sudden switch-on of the offset**

Another way of preparing a balanced population in the asymmetric double-well is to first load the condensate into a green lattice, and subsequently switch on the IR lattice with a proper relative shift that is preset by the glass plate. This is an alternative option when the fast dynamical control of the superlattice phase is not available.

However, as we found out experimentally, this method is quite sensitive to lattice alignment. If the IR lattice is not well-centered, this additional dipole potential also creates sloshing motion and breathing mode excitations, demonstrated later in the experimental section. Better beam alignment would reduce these effects.

On the other hand, these side effects from sudden switch-on of the IR lattice might turn into our favor in the experimental detection phase. Because of the different trap frequencies for the two states in the double well, the sloshing motion of them results in a spatial separation in the time-of-flight images. Therefore, this scheme could be used as a Stern-Gerlach type experiment for an independent readout of the pseudospin-1/2 states.

### **Raman process**

Both of the aforementioned methods prepare the upper-state with a constant phase across the atomic cloud. As we found out later, the upper state in fact has the ground state at  $q = k_L$ , or its wavefunction has alternating phases in the lattices. The above two schemes rely on the assumption that there will not be too much heating created while the atoms relax into the ground state in the upper well, which seems to be the case in our experiment.

Motivated by this observation, another way of preparing the initial state is to use a

direct two-photon process to couple the ground state in the bottom well to the ground state in the upper well. To compare with the Raman-assisted spin-orbit coupling, this Raman-assisted state preparation does not provide the extra momentum transfer in the perpendicular direction. For state preparation, the required momentum transfer of  $k_L$  along the superlattice could be provided by a pair of 1064 nm Raman beams at  $30^\circ$  angle of incidence, or a pair of 532 nm Raman beams at  $14.5^\circ$  angle of incidence. This Raman process without perpendicular momentum transfer could potentially be useful in an interferometric readout of the atomic wavefunction in the double-well as well.

Due to space constraints near the apparatus, we've implemented the first two state preparation schemes, but not yet the last one.

### 4.5.2 Dynamics in the double-wells

The energy offset of  $\Delta$  can be calibrated by measuring the accumulated phase between the A-state (the lower well) and B-state (the upper well) as a function of time in the time-of-flight interference images. In this measurement, a BEC is prepared in a green lattice, and subsequently a weak IR lattice is suddenly switched on with a properly pre-selected superlattice phase to provide the energy offset. After a variable hold, the time-of-flight image is taken to record the interference pattern, shown in Fig. 4-18.

As we see in Fig. 4-18, the population in the time-of-flight images oscillate between the zeroth-order and first-order peaks, corresponding to the case with relative phase of 0 and  $\pi$ . The oscillation frequency in the time-of-flight interference pattern, or the slope of the accumulated phase, is a measure of the energy offset  $\Delta$ . This measurement was performed before the upper-well state relaxed into its ground state at  $q = \pi$ .

If we continue to hold the condensate in this superlattice configuration, interesting dynamics occur. This is better demonstrated from the horizontal imaging, where the A-state and B-state are separated vertically due to a differential force from the slight misalignment of the IR beam. The A-state on the top stayed in the same pattern of  $q = 0$ , whereas the B-state on the bottom developed a different pattern corresponding to a quasi-momentum of  $q = \pi$ , shown in Fig. 4-19.

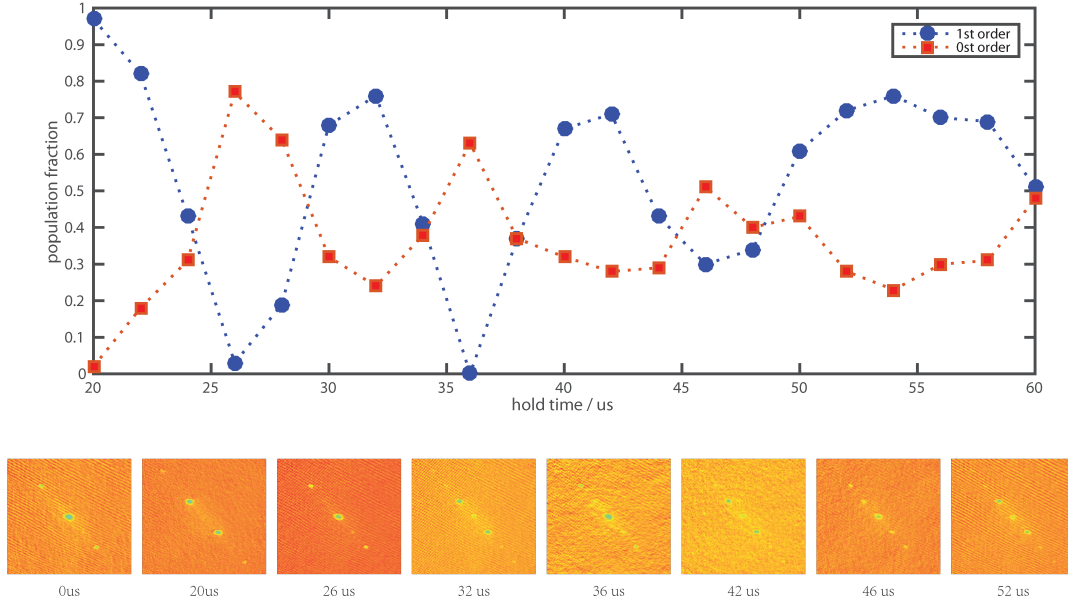


Figure 4-18: The experimental calibration of the offset  $\Delta$ . The relative phase between the left and right wells is accumulated linearly in time, and shows up as the oscillation in the time-of-flight interference. This oscillation calibrates the offset frequency  $\Delta$  in our experiment. This measurement was performed before the upper-well state relaxed into its ground state at  $q = k_L$ .

There are two strong pieces of evidence to support our findings. First of all, the A-state and B-state correspond to the lowest two bands in a superlattice. Therefore, A-state naturally has the ground state at  $q = 0$ , whereas B-state has the ground state at  $q = \pi$ , based on the shape of the band structure. Second, a sloshing motion of the atomic cloud is induced by the sudden switch-on of the IR beam, and A-state would have a faster oscillation in the sloshing motion because of the higher IR intensity and therefore a higher trap frequency in the A-state. This is confirmed in Fig. 4-20, where A state, or the lower state, does show a faster sloshing oscillation. Furthermore, the relaxation process in B-state is an indirect measure of the resonant tunneling between the neighboring upper wells, whereas the tunneling between the A-state and B-state within the same double-well is strongly suppressed by the energy offset, as the relative population stay constant in Fig. 4-20.

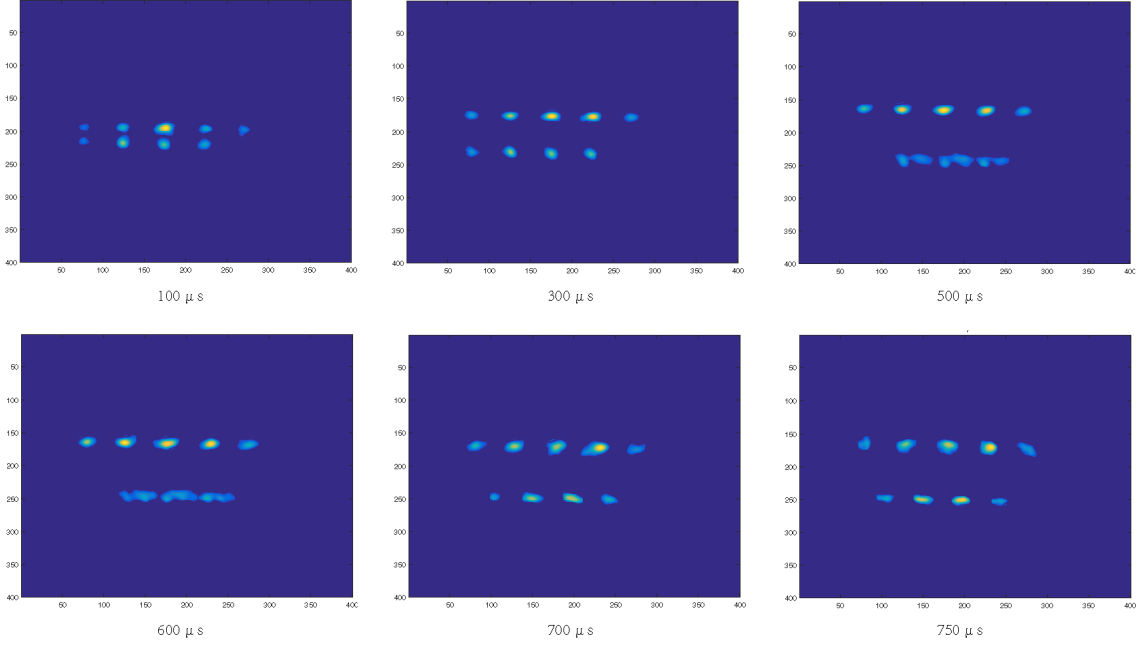


Figure 4-19: The ground states of the lower- and upper-well in the superlattice. The separation in the time-of-flight images is induced by the sloshing motion and different trap frequency for the two states. The initial state is prepared by suddenly switching on an energy offset  $\Delta$ . After  $750 \mu s$ , upper-well relaxes to its ground states at  $q = k_L$ .

### 4.5.3 Detection of the spin-orbit coupling in time-of-flight

#### Structure factor in optical lattices

The interference pattern in the time-of-flight image shows momentum distribution of the atomic cloud. One could also say, it is the measurement of static structure factor of the atomic wavefunction in the trap, and thus can be used to measure the relative strength and phase of the superposed components in the superlattice. In this section, we'll derive the static structure factor for a periodic potential in the general case, and discuss the corresponding interference patterns in a few relevant phase configurations. This general discussion about the static structure factor will show its important in the Bragg scattering section later on as well.

Let's assume that the distribution of interest is  $\psi(\mathbf{r})$ . The momentum distribution measured in a time-of-flight image, or the scatter signal measured in a scattering experiment, is proportional to  $I(\mathbf{q}) \sim S(\mathbf{q}) \equiv |\psi(\mathbf{q})|^2$ , where  $\psi(\mathbf{q}) = \int_V \psi(\mathbf{r}) \exp(-i\mathbf{q}\mathbf{r}) d\mathbf{r}$  is the Fourier transform. This defines the structure factor in the most general context.

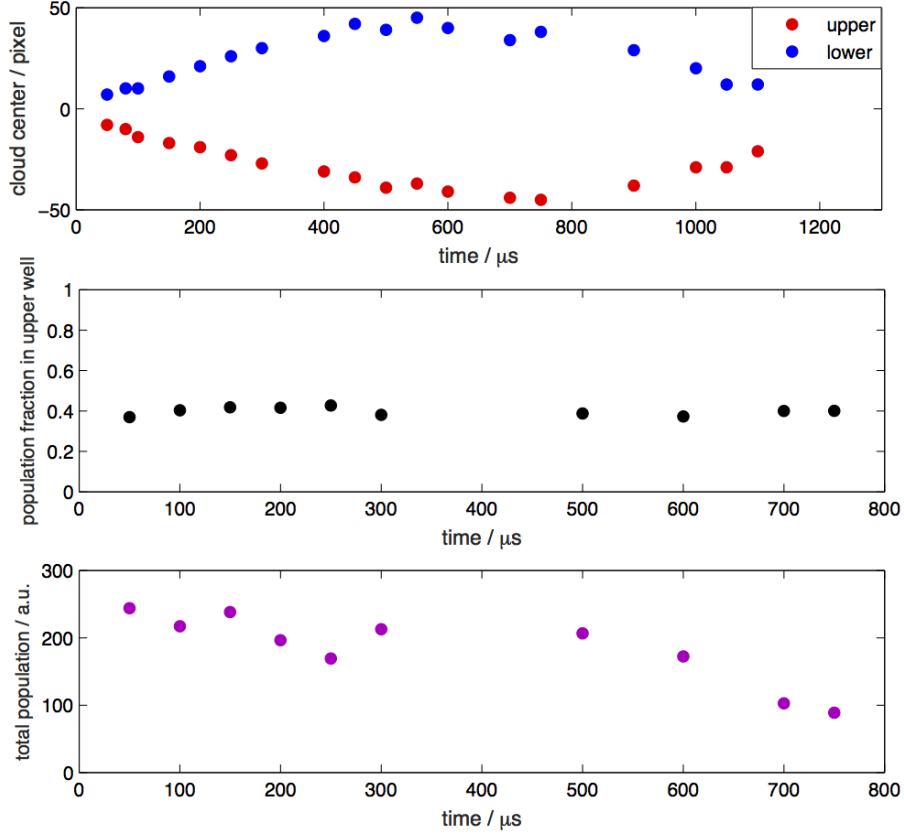


Figure 4-20: The separation of the lowest two bands in the time-of-flight images and the relaxation of the second band into its ground state. The upper-well and lower-well states show oscillations with different trap frequencies. During the relaxation process, the relative population stays constant, which confirms that the tunneling between the double-well is strongly suppressed by the energy offset  $\Delta$ .

To make it clear, the distribution  $\psi(\mathbf{r})$  corresponds to the atomic wavefunction in the time-of-flight interference measurement, while it is actually the atomic density in the Bragg scattering experiment.

If the system of interest is composed of identical constituents, such as unit cells in a lattice, it is convenient to explicitly capture the variation in  $\psi$  by the sum of the contribution from each constituent,

$$\psi(\mathbf{r}) = \sum_{j=1}^N f(\mathbf{r} - \mathbf{R}_j) = \sum_{j=1}^N (f * \delta)(\mathbf{r} - \mathbf{R}_j) \quad (4.48)$$

with  $\mathbf{R}_j$ ,  $j = 1, \dots, N$  the position of each constituent. In the second equality, the field is decomposed as a sum of the convolution product  $*$  of the function  $f$  and Dirac delta functions depending only on the positions. Using the property that the Fourier transform of a convolution product is simply the product of the Fourier transforms of the two factors, we have

$$S(\mathbf{q}) = |\psi(\mathbf{q})|^2 = |f(\mathbf{q})|^2 \times \left| \sum_{j=1}^N e^{-i\mathbf{q}\mathbf{R}_j} \right|^2 \quad (4.49)$$

$$= S(\mathbf{q})_{\text{unit cell}} \times NS(\mathbf{q})_{\text{grating}} \quad (4.50)$$

In short, time-of-flight interference images measure the structure factor of the whole system, which is a product of the structure factor of a grating and the structure factor of each unit cell.

For a one-dimensional superlattice, the structure factor of the grating with grating constant  $a$  (also the size of the unit cell) is

$$S(\mathbf{q})_{\text{grating}} = \frac{1}{N} \left| \sum_{j=1}^N e^{-i\mathbf{q}\mathbf{R}_j} \right|^2 = \frac{1}{N} \left| \frac{1 - e^{-iNqa}}{1 - e^{-iqa}} \right|^2 = \frac{1}{N} \left[ \frac{\sin(Nqa/2)}{\sin(qa/2)} \right]^2 \quad (4.51)$$

The reciprocal lattice has a spacing  $2\pi/a$ , the intensity of the maxima increases with the number of particles as  $S(q = 2n\pi/a) = N$ , and the peak width decreases as  $1/N$ . In the large  $N$  limit, the peaks become infinitely sharp Dirac delta functions,

$$\lim_{N \rightarrow \infty} S(\mathbf{q})_{\text{grating}} = \sum_n \delta(q - 2n\pi/a) \quad (4.52)$$

which is a Dirac comb as a infinite series of Dirac delta functions spaced at intervals of  $2\pi/a$ .

Now let's consider the structure factor in the unit cell  $S(\mathbf{q})_{\text{unit cell}}$ . As before, one could decompose the unit cell structure factor into a product of the structure factor of each constituent, or the single-slit structure factor, and the multi-slit structure factor

based on the arrangement of the constituents in each unit cell,

$$S(\mathbf{q})_{\text{unit cell}} = S(\mathbf{q})_{\text{single slit}} \times S(\mathbf{q})_{\text{multi slit}} \quad (4.53)$$

the single slit in the case of our superlattice corresponds to the Wannier state in each well. For simplicity, the single-slit structure factor is chosen to be a Gaussian profile centered at  $q = 0$  with a proper width for the following discussion in this section.

In the following, we'll apply the general results to a few special cases for the spin-orbit coupling experiment in a superlattice. The natural length unit in this system is the superlattice period  $d = \lambda_{1064}/2$ , and the corresponding momentum unit is  $2\pi/d$ . We label  $k$  as the transverse momentum perpendicular to the superlattice, and  $q$  as the quasi-momentum along the superlattice.

### Case 1. $k = 0$ for 50/50 population

In the first case, we consider the interference between a 50/50 population with transverse momentum  $k = 0$  in the double wells. This is relevant for the double-well offset calibration, when the relative phase between left and right population is accumulated linearly as a function of time, before the upper-state population relax into  $q = k_L$ .

In this case, the structure factor in a unit cell is simply in a double-slit form,

$$S(q)_{\text{multi slit}} = S(q)_{\text{double slit}} = |1 + e^{i(\phi - qb)}|^2 = 2[1 + \cos(\phi - qb)] \quad (4.54)$$

where  $\phi$  is the relative phase between the right and left wells. The double-slit structure factor is a sinusoidal function with the period  $2\pi/b$ . In this case, the grating constant or the size of the unit cell is  $a = d$ , and the double-slit spacing is  $b = d/2$ .

The predicted time-of-flight images as a function of the relative phase  $\phi$  are shown in Fig. 4-21. As time evolves, we expect to see oscillations between the centered  $\phi = 0$  pattern and the symmetric  $\phi = \pi$  pattern at the frequency of offset  $\Delta$ .

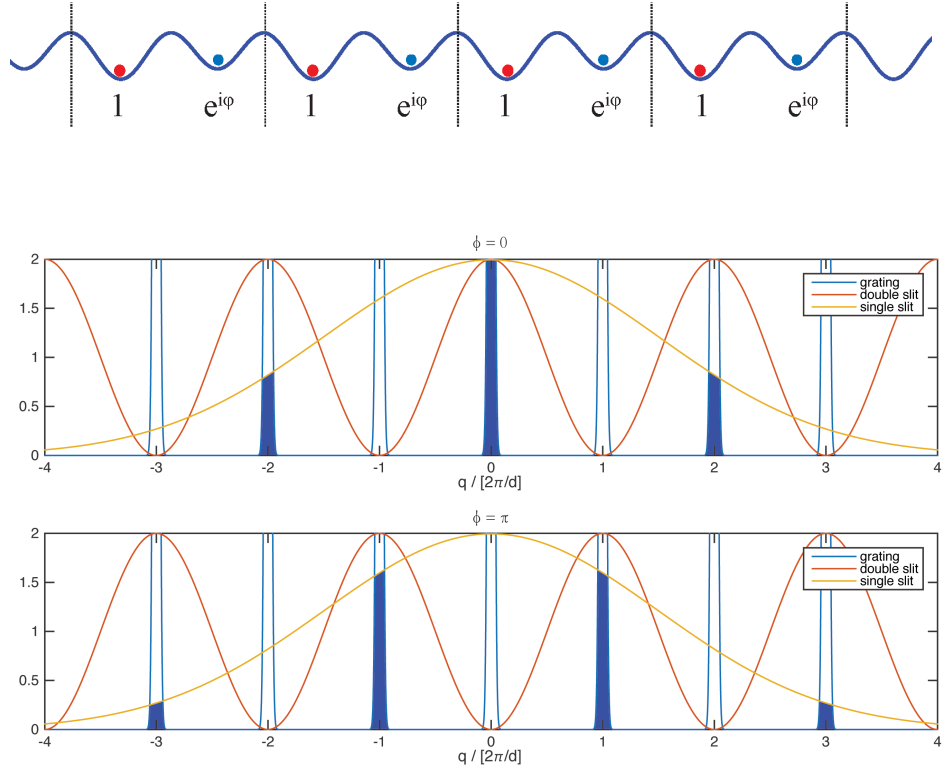


Figure 4-21: Case 1: The relative phases and the corresponding interference pattern of the  $k = 0$  component for 50/50 population. The relative phase is linearly accumulated in time, therefore the time-of-flight interference will show oscillations at the frequency  $\Delta$ .

### Case 2. $k = \pm k_L$ for 100/0 population with only OC or SOC

The second case applies when we have only on-site coupling or spin-orbit coupling in a 100/0 population in the superlattice. The propagating phase of the Raman coupling is imprinted onto the atomic wavefunction to create an alternating phase.

In this case, the size of the unit cell is  $a = 2d$ , the double-slit spacing is  $b = d$ , and the relative phase in the double-slit structure factor is fixed at  $\phi = \pi$ . Therefore, we expect to see a stationary pattern of  $\phi = \pi$  in time.

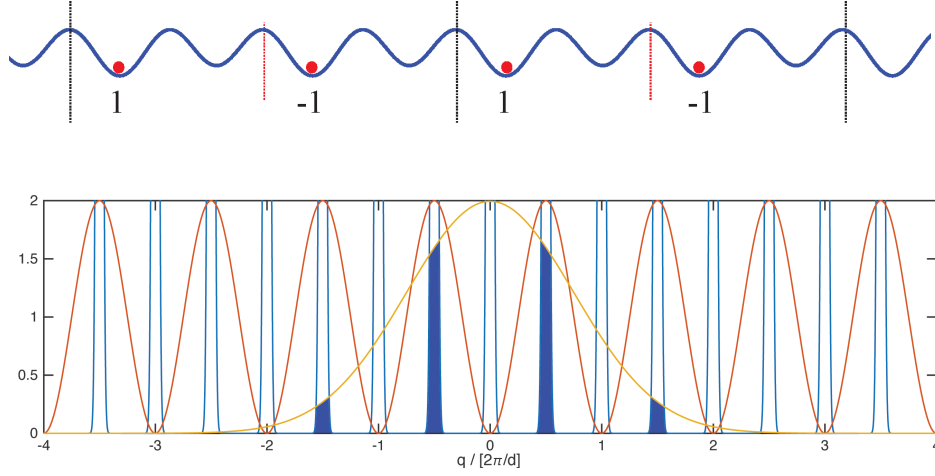


Figure 4-22: Case 2: The relative phases and the corresponding interference pattern of the  $k = \pm k_L$  component for 100/0 population with only the OC or SOC component. The relative phase is locked by the propagation of the Raman coupling, and therefore the time-of-flight interference will be stationary in time.

### Case 3. $k = \pm k_L$ for 100/0 population with both OC and SOC

The third case applies when we have both the on-site coupling and spin-orbit coupling in a 100/0 population in the superlattice. In this case, besides the structure factors considered above, there is an additional double-slit structure factor for the double-well with spacing  $b = d/2$ , due to the interference between the onsite component and the spin-orbit component.

The relative phase between these two comes from the propagating phase of the Raman coupling, and also depends on the sign of the two-photon detuning  $\delta - \Delta \pm E_R$ . When the Raman frequency of  $\Delta$  is increased across the resonance, the relative phase between them (the right respect to the left) goes from  $-\pi/4$  to  $3\pi/4$ , while the spin-orbit coupled component has a resonant strength. Therefore, we expect to see a dispersive signature in the population difference between the left and right peaks.

The predicted time-of-flight images as a function of the relative phase  $\phi$  are shown in Fig. 4-23, assuming on-site coupling and spin-orbit coupling have equal strengths.

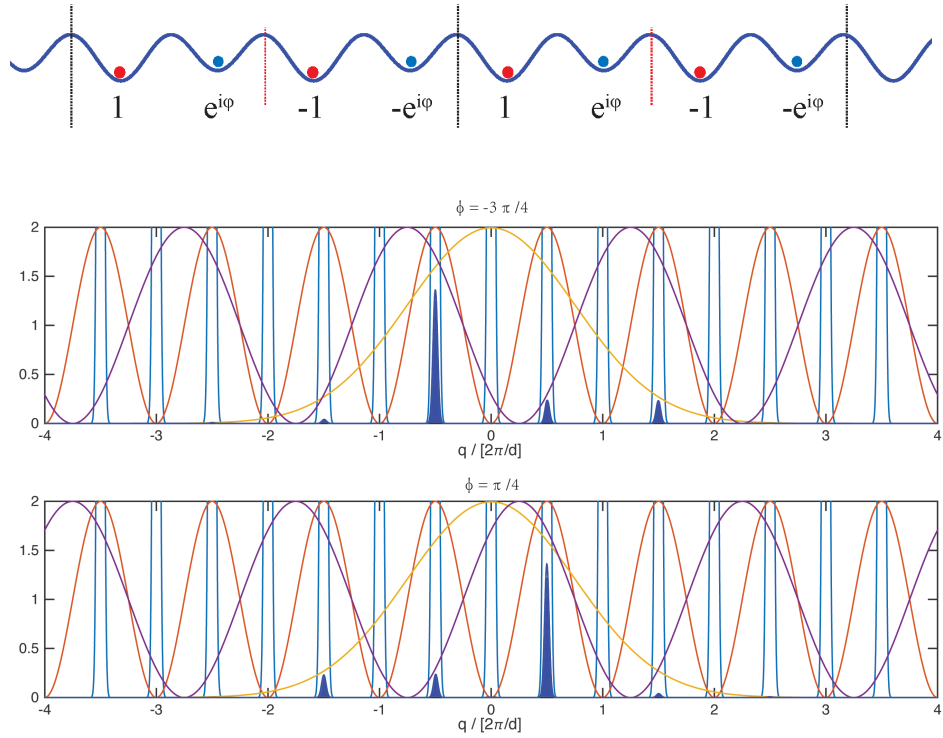


Figure 4-23: Case 3: The relative phases and the corresponding interference pattern of the  $k = \pm k_L$  component for 100/0 population with both the OC and SOC component. The relative phase is finite from the propagation of the Raman coupling, and flips its sign when across the SOC resonance, and therefore the time-of-flight interference will show asymmetry and a dispersive signature in the difference between the plus/minus first-order peaks.

#### Case 4. No interference between quasi-momentum $q = 0$ and $q = k_L$ states

Let's consider the last situation, where we have a condensate in the left wells at quasi-momentum  $q = 0$ , which has a constant phase in each well, and a condensate in the right wells at quasi-momentum  $q = k_L$  which has a relative phase of  $\phi$  with alternating sign. This is motivated by our experimental observation that the upper well, or the second band in the superlattice, has the ground state at  $q = k_L$ , rather than  $q = 0$ .

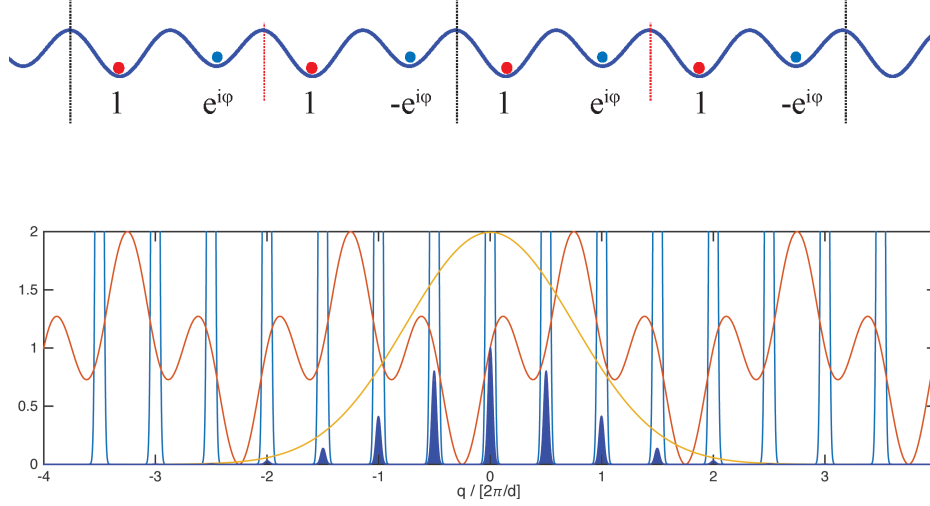


Figure 4-24: Case 4: There is no interference between quasi-momentum  $q = 0$  and  $q = k_L$  states. The total interference pattern is just the sum of the individual patterns.

The multi-slit structure factor in the unit cell in this case is

$$S(q)_{\text{multi slit}} = \left| 1 + e^{i(\phi+qd/2)} + e^{iqd} - e^{i(\phi+3qd/2)} \right|^2 \quad (4.55)$$

$$= 2 + 4 \sin(qd/2)^2 + 2 \cos(qd) + 4[\sin(\phi) + \sin(\phi + qd)] \sin(qd/2) \quad (4.56)$$

$$= 4 + 4 \sin(\phi + qd/2) \sin(qd) \quad (4.57)$$

Although the multi-slit structure factor shows dependence on  $\phi$ , the grating structure factor is non-vanishing only when at  $q = \pi n/d$ , where the multi-slit structure factor is a constant of  $S(q = \pi n/d)_{\text{multi slit}} = 4$ . Therefore, there is no interference in  $\phi$ , and we are not able to extract the value of it from the time-of-flight interference images, as the final interference pattern is just the sum of the individual patterns.

Another easier way to see the result without explicit calculation is that, particles with different momentum simply do not interfere. This is simple and straightforward, since we are measuring the momentum-distribution in the time-of-flight images.

To take the point one step further, we claim that all the onsite coupling and spin-orbit coupling from the left wells do not interfere with couplings from the right wells. This conclusion could be made by noticing that the same Raman coupling shifts the

left-well state and right-well state by the same amount in momentum, and therefore they still do not interfere, or by carefully checking the relevant phases. As a result, the cases that we've discussed in this section have covered all the scenarios that we'll see in our experiment.

#### 4.5.4 Experimental observation of resonant spin-orbit coupling

In this section, we present the experimental data on detecting the spin-orbit coupling signal across the resonance. The experimental results presented here will be focused on a sample with 100 percent population loaded into the A-state.

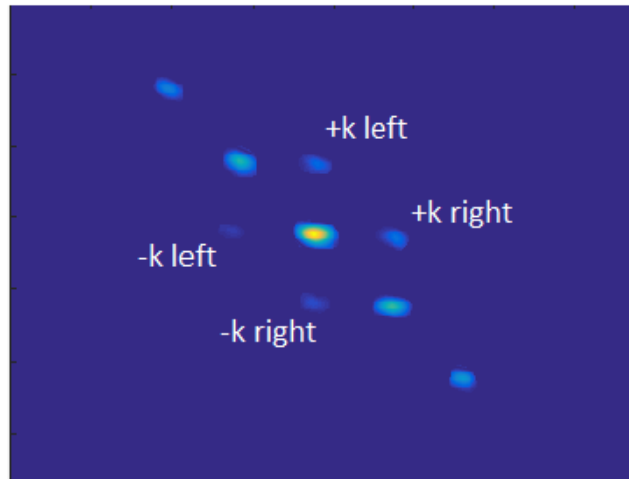


Figure 4-25: A typical time-of-flight image in the spin-orbit coupling experiment, and the notation used in our data analysis. The relevant peaks are explained in the text.

First of all, a typical time-of-flight image in this configuration is shown in Fig. 4-25. The time-of-flight pattern for the A-state with  $q = 0$  shows up in the middle. After the Raman coupling, there is a  $+k$  component separated from the main component, and it has contributions from both on-site coupling and spin-orbit coupling. Similarly, there is a  $-k$  component which corresponds to the counter-rotating terms in the Raman process, and it is usually weaker than the  $+k$  component. In the following discussion, we are mainly looking at the  $+k$  component.

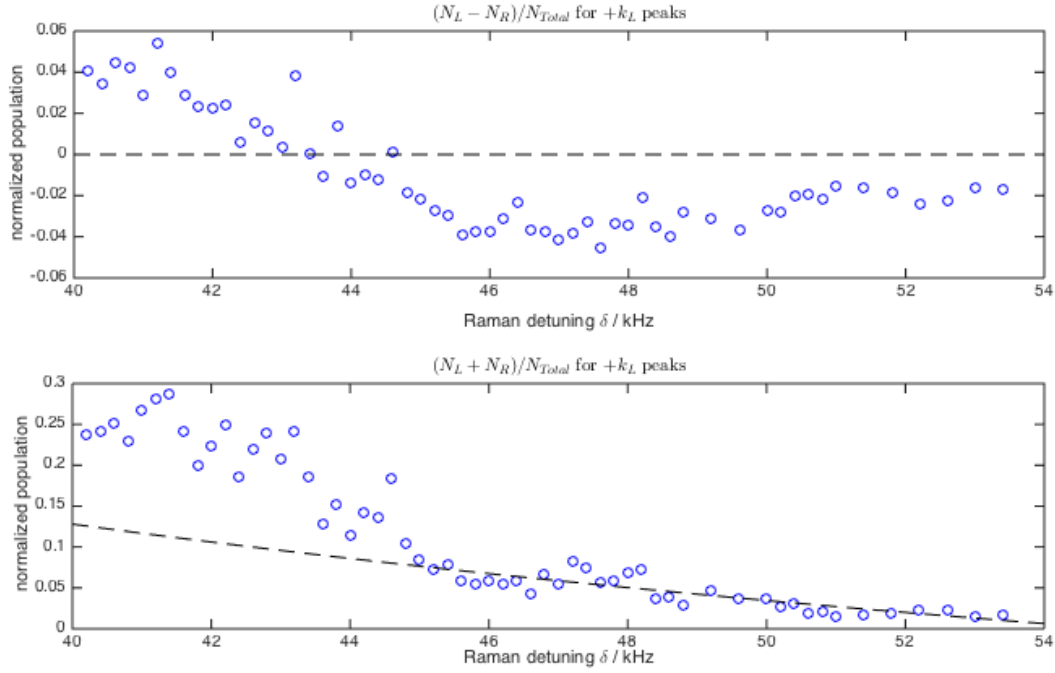


Figure 4-26: The experimental detection of spin-orbit coupling near resonance. The top plot shows the difference between the left and right peaks, where a clear dispersive signal was observed. The dashed line is the zero crossing to guide the reader’s eyes. The bottom plot shows the total of the left and right peaks where a bump showed up around 43 kHz, which could be explained by the enhanced spin-orbit coupling near the resonance. The dashed curve is a  $1/\Delta^2$  fit from the tail for the on-site coupling.

Both  $+k$  and  $-k$  components show  $q = \pi$  time-of-flight pattern in Fig. 4-25. This is the result of interference from the alternating phase in the final state imprinted by the propagating Raman coupling. From the momentum picture, the initial state is the A-state with  $q = 0$ . Since the Raman coupling in our experiment also provides a momentum transfer along the superlattice, this results in the final state at  $q = \pi$ .

Since both on-site coupling and spin-orbit coupling have the final state at  $q = \pi$ , they will interfere in the time-of-flight depending on their relative phase. This relative phase comes from the propagation of the Raman coupling, and will change only when the spin-orbit coupling resonance is crossed. With careful count on the relative phase, we expect to see a stronger left peak below the resonance, and a stronger right peak above the resonance.

The experimental data are shown in Fig. 4-26, as the Raman detuning was scanned

across the spin-orbit coupling resonance. As we expected, the difference between the left and right population showed a clear dispersive signature, and it went back to zero away from the resonance. In addition, there was a bump in the total population due to the enhanced spin-orbit coupling near the resonance. The broadened width can be explained by the inhomogeneity of the offset  $\Delta$  across the atomic cloud.

#### 4.5.5 Detection of the spin-orbit coupling in Bragg scattering

For a spin-orbit coupled condensate in the miscible state, different momentum components of the same spin in the superposition interfere and result in density modulation, or the stripe. In our experiment, even though the pseudospins are in fact in the same atomic state, they are spatially separated in the double-wells, and form stripes along the wells perpendicular to the lattice.

The density modulation comes from the interference between different momentum components. Let's consider the general case with a superposition of two momentum states shifted by momentum  $k_L$  and energy  $\omega$ ,

$$f(x) = (a + be^{ik_Lx - i\omega t + i\phi_0})e^{-i\mu t} \quad (4.58)$$

the atomic density is just the norm of the wavefunction,

$$n(x) = (a + be^{ik_Lx - i\omega t + i\phi_0})(a + be^{ik_Lx - i\omega t + i\phi_0})^* \quad (4.59)$$

$$= a^2 + b^2 + 2ab \cos(k_Lx - \omega t + \phi_0) \quad (4.60)$$

In our experiment, the interference between the main component Eq. 4.36 and the spin-orbit coupling component Eq. 4.37 gives the stationary stripes with periodicity of 1064 nm, when  $\delta = \Delta$  and therefore  $\omega = 0$ . It is stationary because the relative phase does not change in time. The stripes are in phase within the double-well, as well as between the neighboring double-wells, as the initial phase  $\phi_0$  is constant throughout the cloud. Therefore, the stripe pattern is orthogonal to the superlattice as shown in Fig. 4-27.

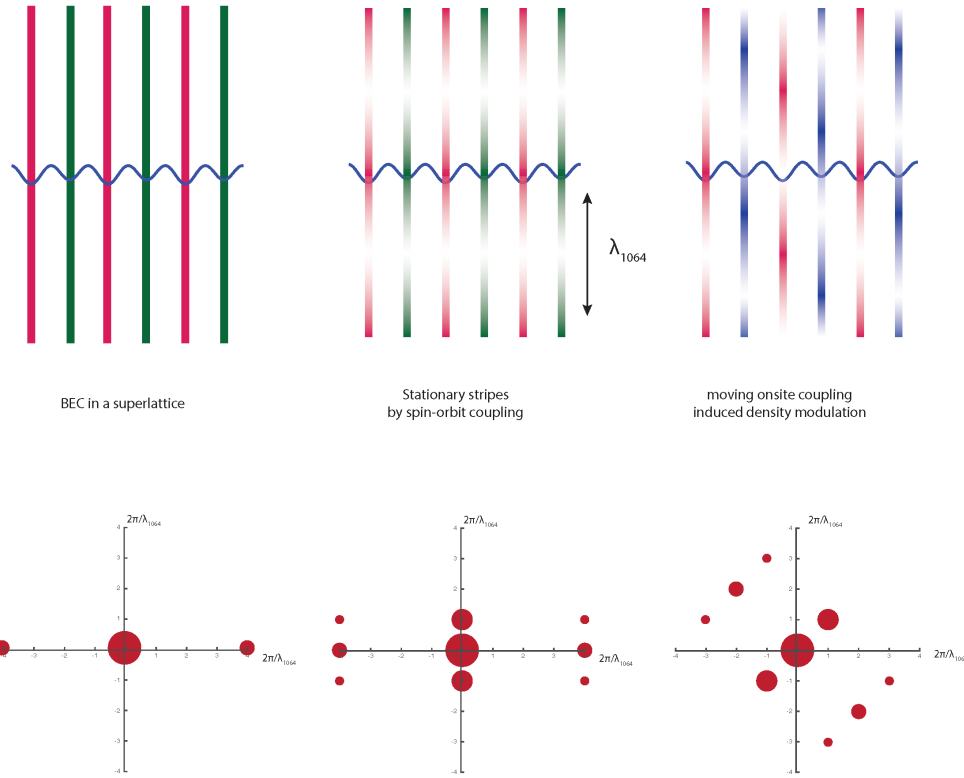


Figure 4-27: The stationary stripes from the spin-orbit coupling, and the moving density modulations from the onsite coupling, and their corresponding structure factors. Notice they have different Bragg planes, and therefore could be detected individually by sending the probe beam from the corresponding Bragg angles. Higher-order Bragg scatterings will vanish, because the sinusoidal density modulation has a single Fourier component.

In contrast, the density modulation created by the onsite coupling, comes from the interference between the main component Eq. 4.36 and the onsite coupling component Eq. 4.39-4.40. These two momentum components have a frequency difference of  $\delta$ , and therefore cause the stripes to move with a speed of  $\delta/k_L \simeq 0.1$  m/s. The initial phase of  $\phi_0$  is alternating due to the propagating phase of the Raman coupling. As a result, the density modulation is at the  $45^\circ$  angle and moving perpendicularly to the lattice, shown in Fig. 4-27 as well.

In fact, an easier way to figure out the stripe pattern is by noticing (again) that it all comes from the momentum difference of the two components that are interfering.

For the onsite coupling, these two are the Raman-coupled and the main component from the same well, which differ by the momentum transfer of  $(k_L, k_L)$  in the Raman process. Whereas for the spin-orbit coupling, these two are the Raman-coupled component from left and the main component from right, or vice versa, and because the two wells have ground states that are shifted in momentum by  $k_L$ , the two components that are interfering differ by momentum of  $(0, k_L)$ . We reach the same conclusion on the stripe patterns in a direct way.

Finally, let's discuss how to detect the density stripes. The time-of-flight detection presented earlier measures the momentum distribution of a cloud, but it does not tell the miscibility of the system. Directly sensitive to the density stripes, Bragg scattering becomes the ideal way of probing the miscible state.

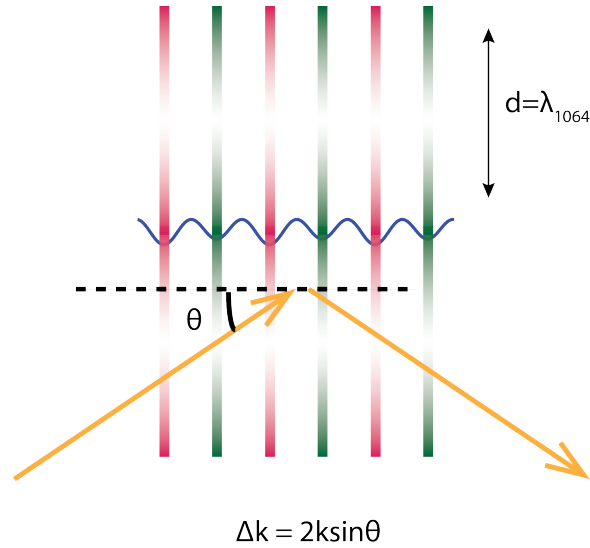


Figure 4-28: The Bragg scattering experiment for detecting the stripe phase. A spin-orbit coupled condensate in the miscible state creates density stripes with periodicity of 1064 nm. A near-resonant light of 589 nm is sent to the atomic cloud at the Bragg angle, illustrated in the figure, for detecting the density stripes.

The constructive interference of the scattered photon follows the Bragg's law,

$$n\lambda = 2d \sin \theta \tag{4.61}$$

where  $\theta$  is the Bragg angle illustrated in Fig. 4-28. The Bragg scattering experiment can also be considered as a way to measure the structure factor of the atomic density,

	1st order	2nd order	3rd order
Bragg angle $\theta$	16.07°	33.61°	56.13°

Table 4.3: The Bragg angles for detecting the stripe phase using 589 nm probe beam. Higher-order Bragg scatterings will vanish, because the sinusoidal density modulation has a single Fourier component.

in which the Bragg photon only gets diffracted with a momentum kick  $\Delta k$  when the structure factor of the atomic density  $S(\Delta k)$  is finite.

To generate a sufficient amount of coherently scattered photons, the near-resonant 589 nm light will be used. The Bragg angles of the lowest three order Bragg scattering have been calculated in Tab. 4.3. However, the higher-order Bragg scatterings vanish in our experiment, because the sinusoidal density modulation has a only single Fourier component.

The moving stripes induced by the onsite coupling can also be detected via Bragg scattering, with a different set of Bragg angles. Due to the motion of these stripes, the scattered Bragg photons will be Doppler-shifted by frequency  $\delta$ . This frequency shift can be detected by beating the scattered beam with the probe beam via a heterodyne detection.



## Chapter 5

# Density Fluctuations in Quantum Degenerate Fermi Gases

Atomic density fluctuation measurements have been carried out as a proof-of-principle experiment in an ideal Fermi gas [40], and these developed techniques are then used to probe many-body physics in strongly interacting Fermi gases [41, 42]. These works have been summarized with details in earlier theses in this lab [7, 8, 43], and published papers are attached in the appendix.



# Chapter 6

## Outlook and Conclusion

This chapter will briefly discuss the extensions of the spin-orbit coupling experiment and future experiment towards direct observation of the stripe phase, as well as other promising directions with the new apparatus. It will also conclude the research work that has been presented in this thesis.

### 6.1 Outlook

In this section, we'll discuss future directions of this experiment, including extensions of the work carried out in this thesis, as well as other interesting and promising topics that can be studied with this system.

#### **Spin-orbit coupling from the B-state**

As we have experimentally observed the resonant spin-orbit coupling signal from the A-state, the next step is to detect the reverse process of resonant spin-orbit coupling from the B-state. Due to the recoils along the transverse direction, the two resonances will be offset by  $2E_L$ .

The fact that A-state and B-state have the ground state with different momentum leads to a favorable situation for our experimental detection: they are orthogonal and do not interfere in the time-of-flight measurement. This means, even though spin up and spin down are in fact in the same atomic hyperfine state in our scheme, we are able

to independently read them out in a single shot. Having detected the resonant spin-orbit coupling from the B-state would complete the study of single particle physics in the spin-orbit coupling Hamiltonian in this system.

### **Direct detection of the stripe phase via Bragg scattering**

From single particle physics to an interacting system, it is very interesting to probe the stripe phase and study the phase transition from the stripe phase into a separated phase. The stripe phase, equivalent of the supersolid phase in condensed matter, has not been directly observed yet in experiment and is of great interest.

The spacing of the stripes in our experiment is on the order of optical wavelength, therefore it is very challenging to resolve them in-situ. Alternatively, Bragg scattering is an ideal tool to directly probe the spatial ordering in the atomic density. Detailed discussions about using Bragg scattering to detect the stripe phase can be found in section 4.5.5.

### **Spin-dependent models in quantum magnetism**

This pseudo-spin system in optical superlattices is also suitable to simulate quantum magnetism and study the magnetic phase transition. Because of different barriers, the resonant tunneling is spin-dependent,  $t_{\uparrow} \neq t_{\downarrow}$ , and due to the spatial separation of the pseudo-spins,  $U_{\uparrow\downarrow} \leq U_{\uparrow\uparrow}, U_{\downarrow\downarrow}$ . This would allow us to simulate spin-dependent models without using spin-dependent lattices of near-resonant light, and does not require a Feshbach resonance since the model parameters can be controlled experimentally by tuning the superlattice.

### **Spin-orbit couplings and gauge fields with fermions**

As we have seen, laser-assisted coupling in a one-dimensional superlattice would allow us to simulate a spin-orbit coupled condensate, and laser-assisted tunneling in a tilted lattice allows us to simulate a condensate under a strong synthetic magnetic field [26]. These techniques can be readily transferred into a fermionic system, such as  ${}^6\text{Li}$  in our experiment. Although specific topics still need to be identified, the emergent Fermi

surface and additional spin degree of freedom in the hyperfine states with Feshbach resonances almost certainly guarantee us new physics waiting to be explored.

## 6.2 Conclusion

Quantum simulation of condensed matter systems using ultracold atomic gases remains one of the most exciting avenues of atomic physics. Towards this goal, a next-generation general-purpose cold atom machine was built and tested to meet the new level of complexity and reliability in optical lattice experiments. A new scheme with long sample lifetime and robust stripe phase to simulate spin-orbit coupling Hamiltonian has been implemented using pseudo-spins in an optical superlattice. These developed platforms and techniques could become relevant in simulating exotic quantum states in topological insulators and topological superfluids in the near future.

I hope this work would allow younger generations in this lab to explore interesting quantum physics towards topological states of matter.



# Appendix A

## Suppression of Density Fluctuations in a Quantum Degenerate Fermi Gas

This appendix contains a reprint of Ref. [40]: Christian Sanner, Edward J. Su, Aviv Keshet, Ralf Gommers, Yong-il Shin, Wujie Huang, and Wolfgang Ketterle, *Suppression of Density Fluctuations in a Quantum Degenerate Fermi Gas*, Phys. Rev. Lett. **105**, 040402 (2010).



## Suppression of Density Fluctuations in a Quantum Degenerate Fermi Gas

Christian Sanner, Edward J. Su, Aviv Keshet, Ralf Gommers, Yong-il Shin, Wujie Huang, and Wolfgang Ketterle

*MIT-Harvard Center for Ultracold Atoms, Research Laboratory of Electronics, and Department of Physics,  
Massachusetts Institute of Technology, Cambridge Massachusetts 02139, USA*

(Received 7 May 2010; published 19 July 2010)

We study density profiles of an ideal Fermi gas and observe Pauli suppression of density fluctuations (atom shot noise) for cold clouds deep in the quantum degenerate regime. Strong suppression is observed for probe volumes containing more than 10 000 atoms. Measuring the level of suppression provides sensitive thermometry at low temperatures. After this method of sensitive noise measurements has been validated with an ideal Fermi gas, it can now be applied to characterize phase transitions in strongly correlated many-body systems.

DOI: 10.1103/PhysRevLett.105.040402

PACS numbers: 03.75.Ss, 05.30.Fk, 67.85.Lm

Systems of fermions obey the Pauli exclusion principle. Processes that would require two fermions to occupy the same quantum state are suppressed. In recent years, several classic experiments have directly observed manifestations of Pauli suppression in Fermi gases. Antibunching and the suppression of noise correlations are a direct consequence of the forbidden double occupancy of a quantum state. Such experiments were carried out for electrons [1–3], neutral atoms [4,5], and neutrons [6]. In principle, such experiments can be done with fermions at any temperature, but in practice low temperatures increase the signal. A second class of (two-body) Pauli suppression effects, the suppression of collisions, requires a temperature low enough such that the de Broglie wavelength of the fermions becomes larger than the range of the interatomic potential and  $p$ -wave collisions freeze-out. Experiments observed the suppression of elastic collisions [7] and of clock shifts in radio frequency spectroscopy [8,9].

Here we report on the observation of Pauli suppression of density fluctuations. This is, like the suppression of collisions between different kinds of fermions [10], a many-body phenomenon which occurs only at even lower temperatures in the quantum degenerate regime, where the Fermi gas is cooled below the Fermi temperature and the low lying quantum states are occupied with probabilities close to 1. In contrast, an ideal Bose gas close to quantum degeneracy shows enhanced fluctuations [11].

The development of a technique to sensitively measure density fluctuations was motivated by the connection between density fluctuations and compressibility through the fluctuation-dissipation theorem. In this Letter, we validate our technique for determining the compressibility by applying it to the ideal Fermi gas. In future work, it could be extended to interesting many-body phases in optical lattices which are distinguished by their incompressibility [12]. These include the band insulator, Mott insulator, and also the antiferromagnet for which spin fluctuations, i.e., fluctuations of the difference in density between the two spin states are suppressed.

Until now, sub-Poissonian number fluctuations of ultracold atoms have been observed only for small clouds of bosons with typically a few hundred atoms [13–16] and directly [17,18] or indirectly [19] for the bosonic Mott insulator in optical lattices. For fermions in optical lattices, the crossover to an incompressible Mott insulator phase was inferred from the fraction of double occupations [20] or the cloud size [21]. Here we report the observation of density fluctuations in a large cloud of fermions, showing sub-Poissonian statistics for atom numbers in excess of 10 000 per probe volume.

The basic concept of the experiment is to repeatedly produce cold gas clouds and then count the number of atoms in a small probe volume within the extended cloud. Many iterations allow us to determine the average atom number  $N$  in the probe volume and its variance  $(\Delta N)^2$ . For independent particles, one expects Poisson statistics, i.e.,  $(\Delta N)^2/\langle N \rangle = 1$ . This is directly obtained from the fluctuation-dissipation theorem  $(\Delta N)^2/\langle N \rangle = nk_B T \kappa_T$ , where  $n$  is the density of the gas, and  $\kappa_T$  the isothermal compressibility. For an ideal classical gas  $\kappa_T = 1/(nk_B T)$ ,

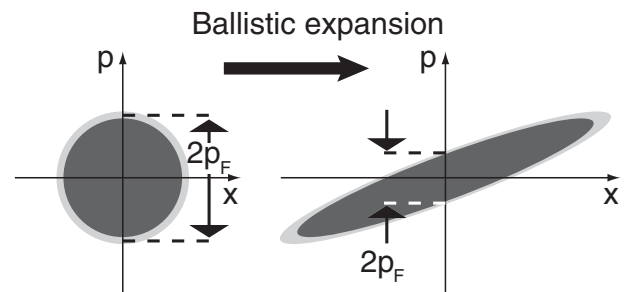


FIG. 1. Phase space diagram of ballistic expansion of a harmonically trapped Fermi gas. Ballistic expansion conserves phase space density and shears the initially occupied spherical area into an ellipse. In the center of the cloud, the local Fermi momentum and the sharpness of the Fermi distribution are scaled by the same factor, keeping the ratio of local temperature to Fermi energy constant. The same is true for all points in the expanded cloud relative to their corresponding unscaled in-trap points.

and one retrieves Poissonian statistics. For an ideal Fermi gas close to zero temperature with Fermi energy  $E_F$ ,  $\kappa_T = 3/(2nE_F)$ , and the variance  $(\Delta N)^2$  is suppressed below Poissonian fluctuations by the Pauli suppression factor  $3k_B T/(2E_F)$ . All number fluctuations are thermal, as indicated by the proportionality of  $(\Delta N)^2$  to the temperature in the fluctuation-dissipation theorem. Only for the ideal classical gas, where the compressibility diverges as  $1/T$ , one obtains Poissonian fluctuations even at zero temperature.

The counting of atoms in a probe volume can be done with trapped atoms, or after ballistic expansion. Ballistic expansion maintains the phase space density and therefore the occupation statistics. Consequently, density fluctuations are exactly rescaled in space by the ballistic expansion factors as shown in Fig. 1 [22,23]. Note that this rescaling is a unique property of the harmonic oscillator potential, so future work on density fluctuations in optical lattices must employ in-trap imaging. For the present work, we chose ballistic expansion. This choice increases the number of fully resolved bins due to optical resolution and depth of field, it allows adjusting the optimum optical density by choosing an appropriate expansion time, and it avoids image artifacts at high magnification.

We first present our main results, and then discuss important aspects of sample preparation, calibration of absorption cross section, data analysis and corrections for photon shot noise. Figure 2(a) shows an absorption image of an expanding cloud of fermionic atoms. The probe volume, in which the number of atoms is counted,

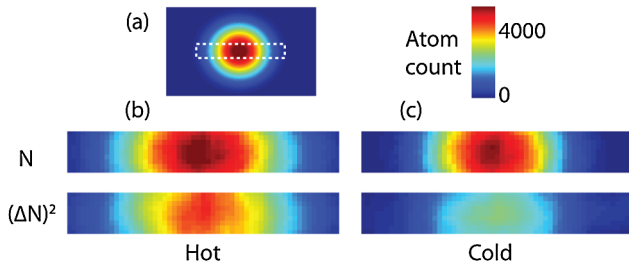


FIG. 2 (color online). Comparison of density images to variance images. For Poissonian fluctuations, the two images at a given temperature should be identical. The variance images were obtained by determining the local density fluctuations from a set of 85 images taken under identical conditions. (a) Two dimensional image of the optical density of an ideal Fermi gas after 7 ms of ballistic expansion. The noise data were taken by limiting the field of view to the dashed region of interest, allowing for faster image acquisition. (b) For the heated sample, variance and density pictures are almost identical, implying only modest deviation from Poissonian statistics. (c) Fermi suppression of density fluctuations deep in the quantum degenerate regime manifests itself through the difference between density and variance picture. Especially in the center of the cloud, there is a large suppression of density fluctuations. The variance images were smoothed over  $6 \times 6$  bins. The width of images (b) and (c) is 2 mm.

chosen to be  $26 \mu\text{m}$  in the transverse directions, and extends through the entire cloud in the direction of the line of sight. The large transverse size avoids averaging of fluctuations due to finite optical resolution. From 85 such images, after careful normalization [24], the variance in the measured atom number is determined as a function of position. After subtracting the photon shot noise contribution, a 2D image of the atom number variance  $(\Delta N)^2$  is obtained. For a Poissonian sample (with no suppression of fluctuations), this image would be identical to an absorption image showing the number of atoms per probe volume. This is close to the situation for the hottest cloud (the temperature was limited by the trap depth), whereas the colder clouds show a distinct suppression of the atom number variance, especially in the center of the cloud where the local  $T/T_F$  is smallest.

In Fig. 3, profiles of the variance are compared to theoretical predictions [25,26]. Density fluctuations at wave vector  $q$  are proportional to the structure factor  $S(q, T)$ . Since our probe volume (transverse size  $26 \mu\text{m}$ ) is much larger than the inverse Fermi wave vector of the expanded cloud ( $1/q_F = 1.1 \mu\text{m}$ ),  $S(q = 0, T)$  has been integrated along the line of sight for comparison with the experimental profiles. Within the local density approximation,  $S(q = 0, T)$  at a given position in the trap is the binomial variance  $n_k(1 - n_k)$  integrated over all momenta, where the occupation probability  $n_k(k, \mu, T)$  is obtained from the Fermi-Dirac distribution with a local chemical potential  $\mu$  determined by the shape of the trap. Figure 4 shows the dependence of the atom number variance on atom number for the hot and cold clouds. A statistical analysis of the data used in the figure is in [24].

The experiments were carried out with typically  $2.5 \times 10^6$   $^6\text{Li}$  atoms per spin state confined in a round crossed dipole trap with radial and axial trap frequencies  $\omega_r = 2\pi \times 160 \text{ s}^{-1}$  and  $\omega_z = 2\pi \times 230 \text{ s}^{-1}$  corresponding to an in-trap Fermi energy of  $E_F = k_B \times 2.15 \mu\text{K}$ . The sam-

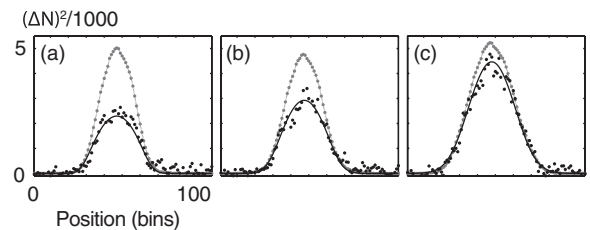


FIG. 3. Comparison of observed variances (black dots) with a theoretical model (black line) and the observed atom number (gray), at three different temperatures (a, b, and c), showing 50, 40, and 15% suppression. Noise thermometry is implemented by fitting the observed fluctuations, resulting in temperatures  $T/T_F$  of  $0.23 \pm .01$ ,  $0.33 \pm .02$ , and  $0.60 \pm .02$ . This is in good agreement with temperatures  $0.21 \pm .01$ ,  $0.31 \pm .01$ , and  $0.6 \pm .1$  obtained by fitting the shape of the expanded cloud [32]. The quoted uncertainties correspond to 1 standard deviation and are purely statistical.

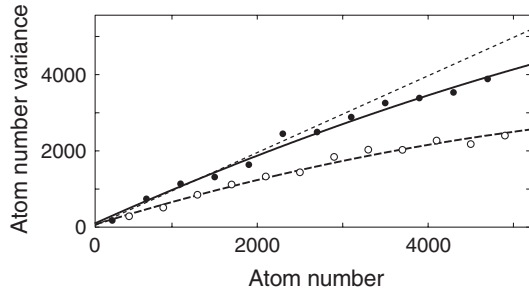


FIG. 4. Atom number variance vs average atom number. For each spatial position, the average atom number per bin and its variance were determined using 85 images. The filled and open circles in the figure are averages of different spatial bin positions with similar average atom number. For a hot cloud at  $T/T_F = 0.6$  (filled circles), the atom number variance is equal to the average atom number (dotted line, full Poissonian noise) in the spatial wings where the atom number is low. The deviation from the linear slope for a cold cloud at  $T/T_F = 0.21$  (open circles) is due to Pauli suppression of density fluctuations. There is also some suppression at the center of the hot cloud, where the atom number is high. The solid and dashed lines are quadratic fits for the hot and cold clouds to guide the eye.

ple was prepared by laser cooling followed by sympathetic cooling with  $^{23}\text{Na}$  in a magnetic trap.  $^6\text{Li}$  atoms in the highest hyperfine state were transferred into the optical trap, and an equal mixture of atoms in the lowest two hyperfine states was produced. The sample was then evaporatively cooled by lowering the optical trapping potential at a magnetic bias field  $B = 320 \pm 5$  G where a scattering length of  $-300$  Bohr radii ensured efficient evaporation. Finally, the magnetic field was increased to  $B = 520 \pm 5$  G, near the zero crossing of the scattering length. Absorption images were taken after 7 ms of ballistic expansion.

We were careful to prepare all samples with similar cloud sizes and central optical densities to ensure that they were imaged with the same effective cross section and resolution. Hotter clouds were prepared by heating the colder cloud using parametric modulation of the trapping potential. For the hottest cloud this was done near 520 G to avoid excessive evaporation losses.

Atomic shot noise dominates over photon shot noise only if each atom absorbs several photons. As a result, the absorption images were taken using the cycling transition to the lowest lying branch of the  $^2P_{3/2}$  manifold. However, the number of absorbed photons that could be tolerated was severely limited by the acceleration of the atoms by the photon recoil, which Doppler shifts the atoms out of resonance. Consequently, the effective absorption cross section depends on the probe laser intensity and duration. To remove the need for nonlinear normalization procedures, we chose a probe laser intensity corresponding to an average of only 6 absorbed photons per atom during a  $4 \mu\text{s}$  exposure. At this intensity, about 12% of the  $^6\text{Li}$  saturation intensity, the measured optical density was 20% lower than its low-intensity value [24]. For each

bin, the atom number variance  $(\Delta N)^2$  is obtained by subtracting the known photon shot noise from the variance in the optical density  $(\Delta \text{OD})^2$  [24]:

$$\frac{\sigma^2}{A^2} (\Delta N)^2 = (\Delta \text{OD})^2 - \frac{1}{\langle N_1 \rangle} - \frac{1}{\langle N_2 \rangle} \quad (1)$$

Here,  $\langle N_1 \rangle \langle N_2 \rangle$  are the average photon numbers per bin of area  $A$  in the image with (without) atoms and  $\sigma$  is the absorption cross section.

The absorption cross section is a crucial quantity in the conversion factor between the optical density and the number of detected atoms. For the cycling transition, the resonant absorption cross section is  $2.14 \times 10^{-13} \text{ m}^2$ . Applying the measured 20% reduction mentioned above leads to a value of  $1.71 \times 10^{-13} \text{ m}^2$ . This is an upper limit to the cross section due to imperfections in polarization and residual line broadening. An independent estimate of the effective cross section of  $1.48 \times 10^{-13} \text{ m}^2$  was obtained by comparing the integrated optical density to the number of fermions necessary to fill up the trap to the chemical potential. The value of the chemical potential was obtained from fits to the ballistic expansion pictures that allowed independent determination of the absolute temperature and the fugacity of the gas. We could not precisely assess the accuracy of this value of the cross section, since we did not fully characterize the effect of a weak residual magnetic field curvature on trapping and on the ballistic expansion. The most accurate value for the effective cross section was determined from the observed atom shot noise itself. The atom shot noise in the wings of the hottest cloud is Poissonian, and this condition determines the absorption cross section. Requiring that the slope of variance of the atom number  $(\Delta N)^2$  vs atom number  $N$  is unity (see Fig. 4) results in a value of  $(1.50 \pm 0.12) \times 10^{-13} \text{ m}^2$  for the effective cross section in good agreement with the two above estimates.

The spatial volume for the atom counting needs to be larger than the optical resolution. For smaller bin sizes (i.e., small counting volumes), the noise is reduced since the finite spatial resolution and depth of field blur the absorption signal. In our setup, the smallest bin size without blurring was determined by the depth of field, since the size of the expanded cloud was larger than the depth of field associated with the diffraction limit of our optical system. We determined the effective optical resolution by binning the absorption data over more and more pixels of the CCD camera, and determining the normalized central variance  $(\Delta N)^2/N$  vs bin size [24]. The normalized variance increased and saturated for bin sizes larger than  $26 \mu\text{m}$  (in the object plane), and this bin size was used in the data analysis. We observe the same suppression ratios for bin sizes as large as  $40 \mu\text{m}$ , corresponding to more than 10 000 atoms per bin.

For a cold fermion cloud, the zero temperature structure factor  $S(q)$  becomes unity for  $q > 2q_F$ . This reflects the

fact that momentum transfer above  $2q_F$  to any particle will not be Pauli suppressed by occupation of the final state. In principle, this can be observed by using bin sizes smaller than the Fermi wavelength, or by Fourier transforming the spatial noise images. For large values of  $q$ , Pauli suppression of density fluctuations should disappear, and the noise should be Poissonian. However, our imaging system loses its contrast before  $q \approx 2q_F$  [24].

Observation of density fluctuations, through the fluctuation-dissipation theorem, determines the product of temperature and compressibility. It provides an absolute thermometer, as demonstrated in Fig. 3 if the compressibility is known or is experimentally determined from the shape of the density profile of the trapped cloud [17,27]. Because variance is proportional to temperature for  $T \ll T_F$ , noise thermometry maintains its sensitivity at very low temperature, in contrast to the standard technique of fitting spatial profiles.

Density fluctuations lead to Rayleigh scattering of light. The differential cross section for scattering light of wave vector  $k$  by an angle  $\theta$  is proportional to the structure factor  $S(q)$ , where  $q = 2k \sin(\theta/2)$  [26]. In this work, we have directly observed the Pauli suppression of density fluctuations and therefore  $S(q) < 1$ , implying suppression of light scattering at small angles (corresponding to values of  $q$  inversely proportional to our bin size). How are the absorption images affected by this suppression? Since the photon recoil was larger than the Fermi momentum of the expanded cloud, large-angle light scattering is not suppressed. For the parameters of our experiment, we estimate that the absorption cross section at the center of a  $T = 0$  Fermi cloud is reduced by only 0.3% due to Pauli blocking [28]. Although we have not directly observed Pauli suppression of light scattering, which has been discussed for over 20 years [28–30], by observing reduced density fluctuations we have seen the underlying mechanism for suppression of light scattering.

In conclusion, we have established a sensitive technique for determining atomic shot noise and observed the suppression of density fluctuations in a quantum degenerate ideal Fermi gas. This technique is promising for thermometry of strongly correlated many-body systems and for observing phase-transitions or cross-overs to incompressible quantum phases.

We acknowledge Joseph Thywissen and Markus Greiner for useful discussions. This work was supported by NSF and the Office of Naval Research, AFOSR (through the MURI program), and under Army Research Office grant no. W911NF-07-1-0493 with funds from the DARPA Optical Lattice Emulator program.

*Note added in proof.*—Results similar to ours are reported in Ref. [31].

- [1] W. D. Oliver, J. Kim, R. C. Liu, and Y. Yamamoto, *Science* **284**, 299 (1999).
- [2] M. Henny *et al.*, *Science* **284**, 296 (1999).
- [3] H. Kiesel, A. Renz, and F. Hasselbach, *Nature (London)* **418**, 392 (2002).
- [4] T. Rom *et al.*, *Nature (London)* **444**, 733 (2006).
- [5] T. Jelte *et al.*, *Nature (London)* **445**, 402 (2007).
- [6] M. Iannuzzi *et al.*, *Phys. Rev. Lett.* **96**, 080402 (2006).
- [7] B. DeMarco *et al.*, *Phys. Rev. Lett.* **82**, 4208 (1999).
- [8] M. W. Zwierlein, Z. Hadzibabic, S. Gupta, and W. Ketterle, *Phys. Rev. Lett.* **91**, 250404 (2003).
- [9] S. Gupta *et al.*, *Science* **300**, 1723 (2003).
- [10] B. DeMarco, S. B. Papp, and D. S. Jin, *Phys. Rev. Lett.* **86**, 5409 (2001).
- [11] J. Estève *et al.*, *Phys. Rev. Lett.* **96**, 130403 (2006).
- [12] Q. Zhou, Y. Kato, N. Kawashima, and N. Trivedi, [arXiv:0901.0606](https://arxiv.org/abs/0901.0606).
- [13] C. S. Chuu *et al.*, *Phys. Rev. Lett.* **95**, 260403 (2005).
- [14] J. Estève *et al.*, *Nature (London)* **455**, 1216 (2008).
- [15] S. Whitlock, C. F. Ockeloen, and R. J. C. Spreeuw, *Phys. Rev. Lett.* **104**, 120402 (2010).
- [16] A. Itah *et al.*, *Phys. Rev. Lett.* **104**, 113001 (2010).
- [17] N. Gemelke, X. Zhang, C. L. Hung, and C. Chin, *Nature (London)* **460**, 995 (2009).
- [18] M. Greiner (unpublished).
- [19] M. Greiner, O. Mandel, T. W. Hänsch, and I. Bloch, *Nature (London)* **419**, 51 (2002).
- [20] R. Jördens *et al.*, *Nature (London)* **455**, 204 (2008).
- [21] U. Schneider *et al.*, *Science* **322**, 1520 (2008).
- [22] S. Gupta, Z. Hadzibabic, J. R. Anglin, and W. Ketterle, *Phys. Rev. Lett.* **92**, 100401 (2004).
- [23] G. M. Bruun and C. W. Clark, *Phys. Rev. A* **61**, 061601(R) (2000).
- [24] See supplementary material at <http://link.aps.org/supplemental/10.1103/PhysRevLett.105.040402> for additional details.
- [25] Y. Castin, in *Proceedings of the International School of Physics Enrico Fermi, Course CLXIV*, edited by M. Inguscio, W. Ketterle, and C. Salomon (IOS, Amsterdam, 2008).
- [26] D. Pines and P. Nozières, *The Theory of Quantum Liquids* (Addison-Wesley, MA, 1988), Vol. 1.
- [27] Q. Zhou and T. L. Ho, [arXiv:0908.3015](https://arxiv.org/abs/0908.3015).
- [28] A. Görlitz, A. P. Chikkatur, and W. Ketterle, *Phys. Rev. A* **63**, 041601(R) (2001).
- [29] K. Helmerson, M. Xiao, and D. E. Pritchard, in *International Quantum Electronics Conference 1990, Book of Abstracts*, econf QTHH4 (1990).
- [30] B. Shuve and J. H. Thywissen, *J. Phys. B* **43**, 015301 (2010). (and references therein)
- [31] T. Mueller *et al.*, *Phys. Rev. Lett.* **105**, 040401 (2010).
- [32] W. Ketterle and M. W. Zwierlein, in *Proceedings of the International School of Physics Enrico Fermi, Course CLXIV*, edited by M. Inguscio, W. Ketterle, and C. Salomon (IOS, Amsterdam, 2008).

# Suppression of Density Fluctuations in a Quantum Degenerate Fermi Gas: Supplementary Information

## EXPERIMENTAL DETAILS

To accurately measure the atom number variance it is necessary to eliminate patterns in the absorption images whose fluctuations increase the observed noise. Weak reflections of the probe beam from the walls of the glass cell and from optical elements in the imaging system can interfere with the probe beam itself, leading to spatial fluctuations in its intensity profile. To reduce interference fringes and ensure uniform illumination, the central area of the probe beam is imaged onto the sample through a 2 mm aperture. Even though the residual fringes are small, there are two significant effects of inhomogeneous illumination which must be addressed.

First, if the time elapsed between the image with atoms and the reference image without atoms is too large, mechanical vibrations of the optics will cause the intensity profile of the probe to change between the two images, creating artifacts in the absorption image. To reduce this effect, we operate our CCD in fast kinetics mode, with a time interval  $\approx 500\mu\text{s}$  between exposures. Since there is no longer enough time for the atoms to exit the frame between images, before taking the reference image we optically pump the atoms from the  $|1\rangle$  state to the  $|6\rangle$  state, and from the  $|2\rangle$  state to the  $|5\rangle$  state ( $|1\rangle$  refers to the lowest hyperfine state, etc.), by exciting them to the  $m_J = 1/2$  excited state manifold. At the magnetic fields used in the experiment, these levels are separated in frequency from the  $|2\rangle$  state used for imaging by  $\approx 2$  GHz and contribute negligibly to resonant imaging.

Second, if the average probe intensity is too high, the atoms subjected to higher intensities will have a lower effective cross-section, and so any spatial fluctuations in the beam intensity will be ‘imprinted’ onto the absorption images. As a result, in our experiment we use a probe beam with maximum intensity of 0.12 of the saturation intensity  $I_{sat}=2.54$  mW/cm<sup>2</sup>, where these effects are relatively small. The variation of optical density with intensity is shown in Fig. 1.

Additionally, the exposure time must be kept very short to prevent the atoms from moving between pixels during the exposure. The expected motion of atoms during the 4  $\mu\text{s}$  exposure is on the order of 1  $\mu\text{m}$ , much smaller than the effective pixel size.

## NOISE DETERMINATION

In this experiment the local atom number variance is determined by comparing the measured number of atoms in the same bin across a series of images. To do this, we

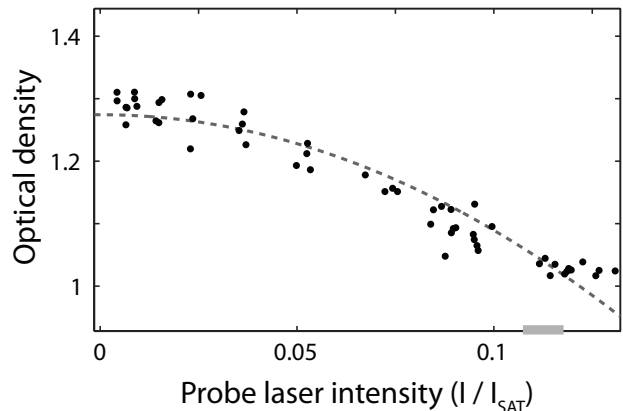


FIG. 1: Determination of the absorption cross section. The observed optical density decreases with increasing probe light intensity. The line is a quadratic fit to the data. The reduction of the cross section is mainly due to the Doppler effect caused by acceleration of the atoms by radiation pressure; a smaller reduction results from the partial saturation of the optical transition. At the probe light intensity chosen in this study (shaded bar), the number of photons absorbed per atoms is about 6. The decrease of the cross section is slightly larger than that predicted by simple models.

must first eliminate the effect of fluctuations in the total atom number between experimental cycles. Initially, we select the 85 images used in the analysis from a larger group of  $\approx 150$  images, using an automated procedure to choose the images whose total atom numbers are closest to the center of the distribution. A very small number of images ( $< 1\%$ ) are manually excluded because of obvious artifacts in the frame due to dust particles or other large perturbations. Then, we subtract a fitted profile from each OD image before computing the variance. Initially we subtracted a fitted 2D Thomas-Fermi profile, but we replaced this with a Gaussian fit which had an insignificant effect on the variances, while taking considerably less computation time.

We then compute the variance in optical density at each position. That variance has contributions from photon and atom shot noise, given by the following formula:

$$(\Delta(OD))^2 = \frac{1}{\langle N_1 \rangle} + \frac{1}{\langle N_2 \rangle} + \frac{\sigma^2}{A^2} (\Delta N_{atom})^2 \quad (1)$$

This equation holds bin by bin:  $N_1$  is the average number of photons measured in a given bin position for the image with atoms, and  $N_2$  is the average number of photons measured in that bin for the reference image.  $(\Delta N_{atom})^2$  is the variance in atom number for that bin,  $\sigma$  is the

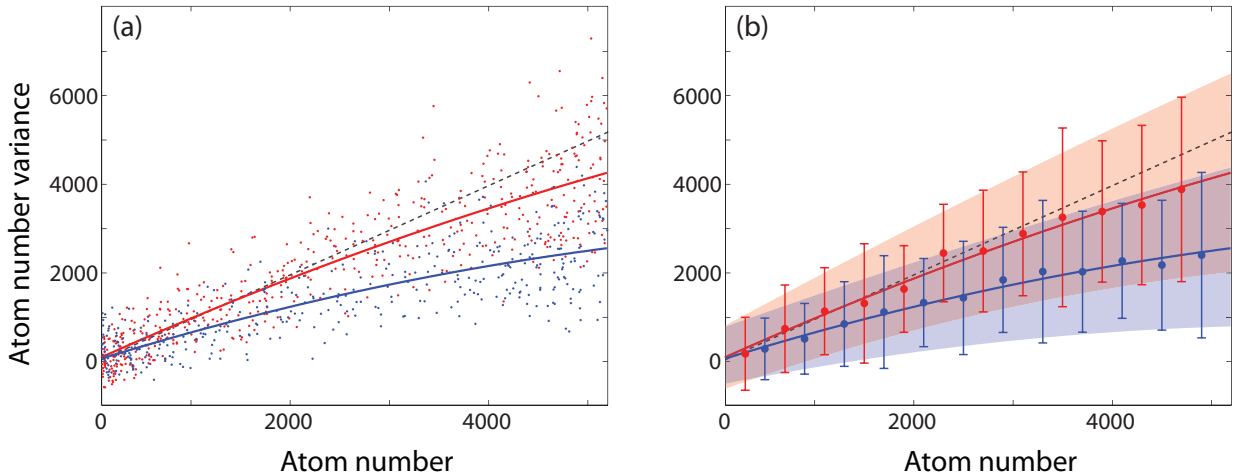


FIG. 2: Atom number variance vs. atom number. (a) Data for all of the resolution elements is plotted. Red points are from the hot cloud at  $T/T_F = 0.6$ , blue points from the cold cloud at  $T/T_F = 0.21$ . There is significant scatter in the variance data, and there are many “cold” pixels which actually have higher variance than their corresponding “hot” pixel. (b) The red and blue shaded regions indicate the expected  $2\sigma$  scatter in sample variance that is expected due to atom and photon counting statistics. The large circles are variance data averaged over pixels with similar atom number for hot (red) and cold (blue) cloud. The bars show the measured  $2\sigma$  scatter of the data points. The measured scatter agrees very well with the expected scatter, indicating that the scatter of the data is fully accounted for by counting statistics. Negative values of the observed atom number variance result from the subtraction of photon shot noise.

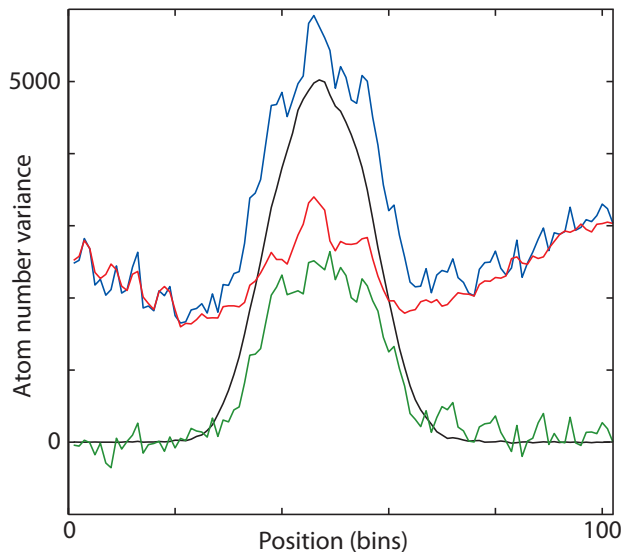


FIG. 3: Determination of profiles of the atom number variance for a cold cloud. For each bin, the total photon count is determined, and its contribution (red) to the total variance of the optical density (blue) is subtracted. The obtained atom number variance (green) is compared to the average atom number (black). The displayed trace reveals 50% noise suppression in the center of the cloud. The apparently high suppression of atom variation in the wings is a statistical fluctuation. Fig. 2 shows that the suppression is monotonic in atomic density.

absorption cross section, and  $A$  is the effective bin area. The atom number variance is isolated by calculating the first two photon shot noise terms and subtracting them. The analysis used in the paper also subtracts contributions from detector read noise and photon shot noise in the dark field, but these are fairly small contributions.

The determination of  $N_1$  and  $N_2$  depends on the CCD gain, which is measured to be 1.18 (counts/electron) from  $\approx 240$  pairs of images without atoms, employing the assumption that the detector statistics are Poissonian. After the subtraction of photon shot noise (and technical noise), the remaining variance in optical density is due to the atom number variance. Fig. 3 shows the contributions of photon and atom number variance to the overall noise in optical density.

The large scatter of the measured atom number variance, as depicted in Fig. 2, is not primarily due to technical noise, but instead a statistical property of the sampling distribution of the variance. The shaded areas are derived from theoretical values for the variance of the sample variance. This is given by

$$\text{Var}(\text{Var}(N)) = \frac{(m-1)^2}{m^3} \mu_4 - \frac{(m-1)(m-3)}{m^3} \mu_2^2 \quad (2)$$

where  $m$  is the number of observations in each sample. The moments  $\mu_2$  and  $\mu_4$  are the central moments of the population distribution. For a Poisson distribution,  $\mu_2 = \langle N \rangle^2$  and  $\mu_4 = \langle N \rangle(1 + 3\langle N \rangle)$ , and for  $m, \langle N \rangle \gg 1$ , this expression reduces to  $2\langle N \rangle^2/m$ . Fig. 2b shows the

comparison between the expected and measured variance in the sample variance.

### IMAGING SYSTEM CHARACTERIZATION

The blurring of adjacent pixels due to finite optical resolution effectively decreases the measured atom number variance. This effect is avoided by binning the data using a sufficiently large bin size (Fig. 5). In our experiment, this bin size is determined by the extension of the cloud along the optical axis, which is much larger than the depth of focus of the diffraction limit of the lens system.

Atom noise allows us to characterize the transfer function of our imaging system. Fig. 4 shows the average power spectrum (modulus squared of the spatial Fourier

transform) of the optical density images. Because the Fourier transform of uncorrelated fluctuations is flat, the deviation from flatness of the density noise corresponds to blurring induced by the lens, barring the central peak corresponding to the shape of the cloud. For wavevectors  $q$  much larger than the resolution limit of the detection scheme, the atom number fluctuations are no longer imaged, and the power spectrum is the photon shot noise. For our experiment this happens for  $q < q_F$ . Comparison of the power spectra for the cold and the hot cloud shows, at small values of  $q$ , a 50% suppression, consistent with the results obtained using spatial bins. If the imaging system still had contrast at  $q > 2q_F$ , we would expect the ratio of the power spectra to approach unity, since momentum transfer  $q > 2q_F$  to a Fermi cloud has negligible Pauli suppression.

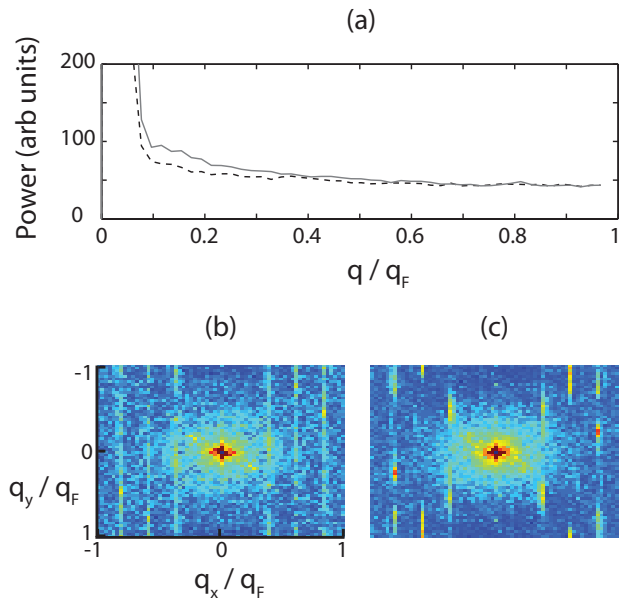


FIG. 4: (a) Radially averaged power spectra of optical density images for hot (solid line) and cold (dashed line) samples (b) Power spectrum of cold sample (arbitrary units) (c) Power spectrum of hot sample (arbitrary units). A constant offset is added to the power spectrum for the hot sample to equalize the levels of photon shot noise.

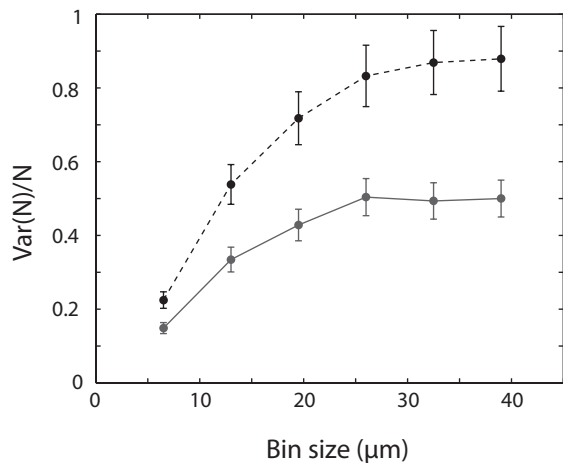


FIG. 5: Observed atom number variance versus bin size for heated (dashed line) and cold (solid line) samples, normalized to 1 for Poissonian statistics. A plateau is reached when the blurring of the bins due to finite optical resolution is negligible.



## Appendix B

# Speckle Imaging of Spin Fluctuations in a Strongly Interacting Fermi Gas

This appendix contains a reprint of Ref. [41]: Christian Sanner, Edward J. Su, Aviv Keshet, Wujie Huang, Jonathon Gillen, Ralf Gommers, and Wolfgang Ketterle, *Speckle Imaging of Spin Fluctuations in a Strongly Interacting Fermi Gas*, Phys. Rev. Lett. **106**, 01040202 (2011).

## Speckle Imaging of Spin Fluctuations in a Strongly Interacting Fermi Gas

Christian Sanner, Edward J. Su, Aviv Keshet, Wujie Huang, Jonathon Gillen, Ralf Gommers, and Wolfgang Ketterle

*MIT-Harvard Center for Ultracold Atoms, Research Laboratory of Electronics, and Department of Physics,  
Massachusetts Institute of Technology, Cambridge Massachusetts 02139, USA*

(Received 8 October 2010; revised manuscript received 10 December 2010; published 6 January 2011)

Spin fluctuations and density fluctuations are studied for a two-component gas of strongly interacting fermions along the Bose-Einstein condensate-BCS crossover. This is done by *in situ* imaging of dispersive speckle patterns. Compressibility and magnetic susceptibility are determined from the measured fluctuations. This new sensitive method easily resolves a tenfold suppression of spin fluctuations below shot noise due to pairing, and can be applied to novel magnetic phases in optical lattices.

DOI: [10.1103/PhysRevLett.106.010402](https://doi.org/10.1103/PhysRevLett.106.010402)

PACS numbers: 05.30.Fk, 03.75.Ss, 67.85.Lm

One frontier in the field of ultracold atoms is the realization of quantum systems with strong interactions and strong correlations. Many properties of strongly correlated systems cannot be deduced from mean density distributions. This has drawn interest toward novel ways of probing cold atoms, e.g., via rf spectroscopy [1,2], Bragg and Raman scattering [3], interferometric methods [4,5], and by recording density correlations [6–8]. Further insight into quantum systems is obtained by looking not only at expectation values, but also at fluctuations. Several recent studies looked at density fluctuations, either of bosons around the Mott insulator transition [9–11], or of a gas of noninteracting fermions [12,13].

In this Letter, we extend the study of fluctuations of ultracold gases in several ways. First, we introduce the technique of speckle imaging as a simple and highly sensitive method to characterize fluctuations. Second, we apply it to a two-component Fermi gas across the Bose-Einstein condensate (BEC)-BCS crossover. Third, we directly measure fluctuations in the magnetization, i.e., the difference of the densities in the two different spin components, bypassing the need to measure the individual densities separately.

Our work is motivated by the prospect of realizing wide classes of spin Hamiltonians using a two-component gas of ultracold atoms in an optical lattice [14,15]. An important thermodynamic quantity to characterize two-component systems is the spin susceptibility, which provides a clear signature of phase transitions or crossovers involving the onset of pairing or magnetic order [16–19]. At a ferromagnetic phase transition the susceptibility diverges, whereas in a transition to a paired or antiferromagnetic phase the susceptibility becomes exponentially small in the ratio of the pair binding energy (or antiferromagnetic gap) to the temperature. The fluctuation-dissipation theorem relates response functions to fluctuations, consequently the spin susceptibility can be determined by measuring the fluctuations in the relative density of the two spin components.

In our experiment, we image the atom clouds using light detuned from resonance so that each atom's real

polarizability, which contributes to the refractive index, is much larger than its imaginary polarizability, which contributes to absorption. Since the detunings for the two spin states are different, spin fluctuations lead to fluctuations in the local refractive index, resulting in phase shifts of the imaging light that vary randomly in space. We measure these phase shifts by imaging the resulting speckle patterns.

These speckle patterns are created by propagation, which converts the spatially varying phase shifts of the imaging light into an intensity pattern on our detector without the use of a phase plate. Spin and density fluctuations occur on all spatial scales down to the interatomic separation; the smallest observable fluctuations have a wavelength equal to the imaging system's maximum resolution. In our system that length has a Rayleigh range, and hence a depth of field, smaller than the cloud size, so the recorded image is necessarily modified by propagation effects. Propagation mixes up amplitude and phase signals [Fig. 1]. This can be easily seen in the case of a phase grating, which creates an interference pattern further downstream; after propagating for a distance equal to the Rayleigh range of the grating spacing, the imprinted phase is converted into an amplitude pattern. This feature of speckle makes our imaging technique both simple and robust. It is insensitive against defocusing, and allows us to image fluctuations of the real part of the refractive index (i.e., a phase signal) without a phase plate or other Fourier optics.

Similar physics is responsible for laser speckle when a rough surface scatters light with random phases [20], and occurs when a Bose-Einstein condensate with phase fluctuations develops density fluctuations during expansion [21], or when a phase-contrast signal is turned into an amplitude signal by deliberate defocusing [22].

The experiments were performed with typically  $10^6$   $^6\text{Li}$  atoms in each of the two lowest hyperfine states  $|1\rangle$  and  $|2\rangle$  confined in an optical dipole trap oriented at  $45^\circ$  to the imaging axis with radial and axial trap frequencies  $\omega_r = 2\pi \times 108.9(6) \text{ s}^{-1}$  and  $\omega_z = 2\pi \times 7.75(3) \text{ s}^{-1}$ . For the

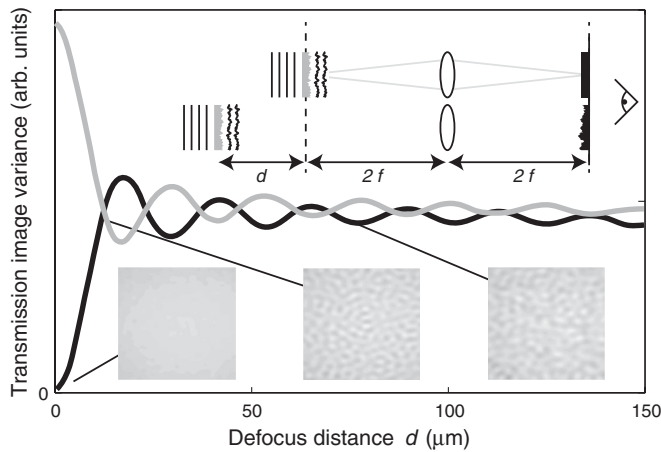


FIG. 1. Simulation of propagation effects after light has passed through a Poissonian phase noise object. Shown are the variance measured in the amplitude or in-phase quadrature (black line) and the out-of-phase quadrature (gray line) as a function of defocus distance, for an imaging system with a numerical aperture of 0.14. Within a distance less than 5% of our cloud size, noise becomes equally distributed between the two quadratures and the variances in transmission and phase-contrast images become the same. (Top inset) For small phase fluctuations, an in-focus phase noise object gives no amplitude contrast, but when it is out of focus it does. (Bottom inset) Sample intensity patterns for a defocused phase object.

samples imaged at 527 G, the sample preparation was similar to that described in [13], with a temperature of  $0.14(1)T_F$ . The samples imaged at other magnetic fields were prepared in a similar fashion, except that evaporation was performed at 1000 G to a final temperature of  $T = 0.13(1)T_F$  before ramping the magnetic field over 1.5 s to its final value. The temperature at 1000 G was determined by fitting a noninteracting Thomas-Fermi distribution in time of flight. The temperatures at other points in the crossover were related to that value assuming an isentropic ramp, using calculations presented in [23]. Using this method we obtain temperatures of  $0.13(1)T_F$  at 915 G,  $0.19(1)T_F$  at 830 G, and  $0.19(3)T_F$  at 790 G where additional evaporation was performed to achieve a central optical density similar to that at the other magnetic fields. The extent of the cloud along the imaging direction was  $135 \mu\text{m}$ , much larger than the Rayleigh range of  $8 \mu\text{m}$  for our imaging system with a NA of 0.14.

The superfluid to normal phase boundary was determined by measuring condensate fraction [Fig. 2] using the standard magnetic field sweep technique [24,25]. For this, the magnetic field was rapidly switched to 570 G to transfer atom pairs to more deeply bound pairs (molecules) which survive ballistic expansion. For resonant imaging of the molecules, the field was ramped back to 790 G over 10 ms. The condensate fraction was determined by fitting the one-dimensional density profiles with a bimodal distribution.

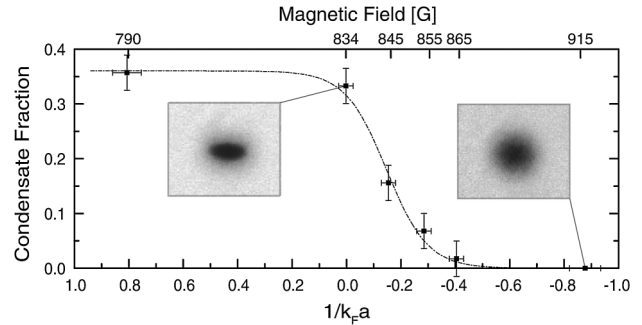


FIG. 2. Measured condensate fraction as a function of dimensionless interaction strength  $1/(k_F a)$ . Insets show typical images from which the condensate fraction was extracted by fitting a bimodal distribution. The dashed line is a sigmoidal fit to guide the eye.

As previously described, propagation converts spatial fluctuations in the refractive index into amplitude fluctuations on the detector. For different choices of the probe light frequency, the two atomic spin states will have different real polarizabilities and the local refractive index will be a different linear combination of the (line-of-sight integrated) column densities  $n_1$  and  $n_2$ . To measure the susceptibility we choose a probe light frequency exactly between the resonances for states  $|1\rangle$  and  $|2\rangle$ , so that the real polarizabilities are opposite and the refractive index is proportional to the magnetization ( $n_1 - n_2$ ). The intensity fluctuations on the detector after propagation are consequently proportional to the fluctuations in magnetization. Since a refractive index proportional to  $(n_1 + n_2)$  occurs only in the limit of infinite detuning, we measure the fluctuations in the total density by exploiting the fact that the fluctuations in total density can be inferred from the fluctuations in two different linear combinations of  $n_1$  and  $n_2$ . For convenience, we obtain the second linear combination using a detuning that has the same value, but opposite sign for state  $|2\rangle$ , and therefore three times the value for state  $|1\rangle$ . With this detuning, we record images of the fluctuations in  $(n_1/3 + n_2)$ .

In principle, this information can be obtained by taking separate absorption images on resonance for states  $|1\rangle$  and  $|2\rangle$ . However, the images would have to be taken on a time scale much faster than that of atomic motion and there would be increased technical noise from the subtraction of large numbers. The use of dispersive imaging has the additional advantage over absorption in that the number of scattered photons in the forward direction is enhanced by superradiance. As a result, for the same amount of heating, a larger number of signal photons can be collected [26]. This is crucial for measuring atomic noise, which requires the collection of several signal photons per atom. The choice of detuning between the transitions of the two states has the important feature that the index of refraction for an equal mixture fluctuates around zero, avoiding any lensing and other distortions of the probe beam. This is not

the case for other choices of detuning, and indeed, we observe some excess noise in those images (see below). At the detunings chosen, 10% residual attenuation is observed, some due to off-resonant absorption, some due to dispersive scattering of light out of the imaging system by small scale density fluctuations. The contribution to the variance of the absorption signal relative to the dispersive signal scales as  $(2\Gamma)^2/\delta^2 \approx 0.006$  and can be neglected in the interpretation of the data.

The noise analysis procedure was nearly identical to that performed in [13]. A high-pass filter with a cutoff wavelength of 13  $\mu\text{m}$  was applied to each image of the cloud to minimize the effect of fluctuations in total atom number. Then, for each pixel position, the variance of the optical densities at that position in the different images was computed. After the subtraction of the contribution of photon shot noise, the resulting variance image reflects the noise contribution from the atoms.

The goal of our noise measurements is to determine at various interaction strengths the normalized susceptibility  $\tilde{\chi} = \chi/\chi_0$  and compressibility  $\tilde{\kappa} = \kappa/\kappa_0$ , where  $\chi_0 = 3n/2E_F$  and  $\kappa_0 = 3/2nE_F$  are the susceptibility and compressibility of a zero-temperature noninteracting Fermi gas with the same total density  $n$  and Fermi energy  $E_F$ . Before studying spin fluctuations through the BEC-BCS crossover, we therefore calibrate our measurement by measuring the spin fluctuations in a noninteracting mixture, realized at 527 G where the scattering length between the two states vanishes. Figure 3 shows raw profiles of the variances  $\Delta_-^2$  and  $\Delta_+^2$  measured at the two detunings. These fluctuations in the speckle pattern are proportional to number fluctuations in the specified probe volume  $V$ :  $\Delta_-^2 = [c\Delta(N_1 - N_2)]^2$  and  $\Delta_+^2 = [c'\Delta(N_1/3 + N_2)]^2$ . In these relations  $c$  and  $c'$  are factors which have to be calibrated. Without interactions,  $N_1$  and  $N_2$  are uncorrelated, and one predicts  $[\Delta(N_1 - N_2)]^2/[\Delta(N_1/3 + N_2)]^2 = 2/[1 + (1/3)^2] = 1.8$ .

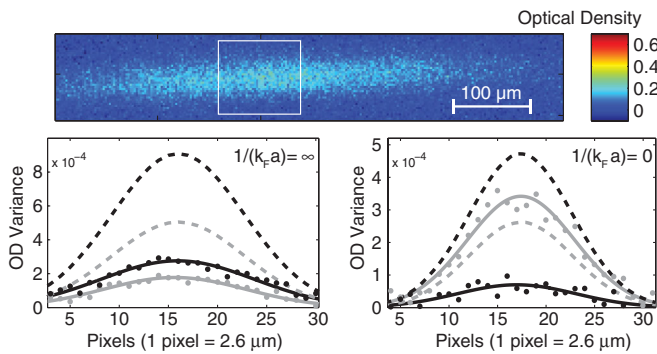


FIG. 3 (color online). (Top panel) Example speckle noise image, with white box indicating analysis region. (Bottom panels) Noise data for noninteracting (left panel) and resonantly interacting (right panel) cold clouds, showing  $\Delta_-^2$  (black dots) and  $\Delta_+^2$  (gray dots). Solid lines are Gaussian fits to the data, and dotted lines illustrate the expected full Poissonian noise for the corresponding quantities based on density determined from off-resonant absorption.

The observed ratio of  $\Delta_-^2/\Delta_+^2 = 1.56(14)$  reflects excess noise contributing to  $\Delta_+^2$  due to residual systematic dispersive effects and is accounted for by setting  $c'/c = \sqrt{1.8/1.56}$ . For high temperatures, the atomic noise of the noninteracting gas approaches shot noise; for lower temperatures we observe a reduction in noise due to Pauli blocking as in our previous work [13]. With our new method, we easily discern spin fluctuations with a variance of less than 10% of atom shot noise.

The fluctuation-dissipation theorem connects the variances  $[\Delta(N_1 - N_2)]^2$  and  $[\Delta(N_1 + N_2)]^2$  to the susceptibility  $\tilde{\chi}$  and the compressibility  $\tilde{\kappa}$  via  $[\Delta(N_1 - N_2)]^2 = 3N/2(T/T_F)\tilde{\chi}$  and  $[\Delta(N_1 + N_2)]^2 = 3N/2(T/T_F)\tilde{\kappa}$  with  $N = N_1 + N_2$  and  $T/T_F$  being the temperature measured in units of the Fermi temperature  $T_F$ . Recomposing the variances from the two experimentally accessible linear combinations these relations become  $\Delta_-^2/Nc^2 = 3/2(T/T_F)\tilde{\chi}$  and  $9/4\Delta_+^2/Nc'^2 - 1/4\Delta_-^2/Nc^2 = 3/2(T/T_F)\tilde{\kappa}$ . The constants  $c$  and  $c'$  are determined using the noise measurements at 527 G for a noninteracting Fermi gas for which  $\tilde{\chi} = \tilde{\kappa} = 1 + O((T/T_F)^2)$ . This analysis ignores line-of-sight integration corrections.

Figure 4 shows the spin susceptibility, the compressibility, and the ratio between the two quantities for the interacting mixtures as the interaction strength is varied through the BEC-BCS crossover. The susceptibility and compressibility reproduce the expected qualitative behavior: for the sample at unitarity, where the transition temperature is sufficiently high that a sizable portion of the sample is superfluid, and for the sample on the BEC side, the spin susceptibility is strongly suppressed relative to the compressibility. This reflects the fact that the atoms form bound

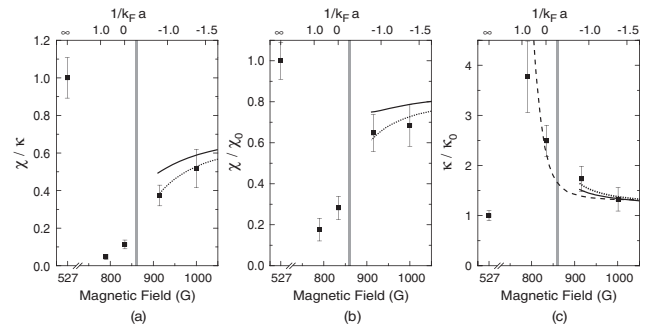


FIG. 4. (a) The ratio  $\chi/\kappa$ , (b) the normalized susceptibility  $\chi/\chi_0$ , and (c) the normalized compressibility  $\kappa/\kappa_0$  in the BEC-BCS crossover. The variances derived from sequences of images are converted into thermodynamic variables using the measured temperatures and a calibration factor determined from the noninteracting gas. The vertical line indicates the onset region of superfluidity, as determined via condensate fraction measurements. The curves show theoretical zero temperature estimates based on 1st (dotted) and 2nd order (solid) perturbative formulas obtained from Landau's Fermi-liquid theory integrated along the line of sight, and results from a Monte Carlo calculation (dashed) for the compressibility in a homogeneous system [32].

molecules or generalized Cooper pairs; the spin susceptibility should be exponentially small in the binding energy, while the enhanced compressibility reflects the bosonic character of the molecular condensate. At 915 G and 1000 G, where the sample is above the superfluid critical temperature, the susceptibility is larger but still below its value for the noninteracting gas, reflecting the persistence of pair correlations even in the normal phase of the gas.

Above the Feshbach resonance, for attractive interactions, we compare our results to first and second order perturbation theory in the small parameter  $k_F a$ . This ignores the instability to the superfluid BCS state at exponentially small temperatures. The perturbation theory is formulated for the Landau parameters for a Fermi liquid [16,27]. The susceptibility and compressibility are given by  $\chi_0/\chi = (1 + F_0^a)m/m^*$ ,  $\kappa_0/\kappa = (1 + F_0^s)m/m^*$ , where  $m^* = m(1 + F_1^s/3)$  is the effective mass, and  $F_l^s$ ,  $F_l^a$  are the  $l$ th angular momentum symmetric and antisymmetric Landau parameters, respectively. Although the experimental data are taken for relatively strong interactions outside the range of validity for a perturbative description, the predictions still capture the trends observed in the normal phase above the Feshbach resonance. This shows that more accurate measurements of the susceptibility, and a careful study of its temperature dependence, are required to reveal the presence of a possible pseudogap phase.

In our analysis we have neglected quantum fluctuations which are present even at zero temperature [16,28]. They are related to the large- $q$  static structure factor  $S(q)$  measured in [29] and proportional to the surface of the probe volume, scaling with  $N^{2/3} \log(N)$ . For fluctuations of the total density, their relative contribution is roughly  $N^{-1/3}/(T/T_F)$ , and at most 40% for our experimental parameters. Attractive interactions and pairing suppress both the thermal and quantum spin fluctuations, but it is not known at what temperature quantum fluctuations become essential.

Spin susceptibilities can also be obtained from the equation of state which can be determined by analyzing the average density profiles of imbalanced mixtures [30]. Our method has the advantage of being applicable without imbalance, and requires only local thermal equilibrium. Moreover fluctuations can be compared with susceptibilities determined from the equation of state to perform absolute, model-independent thermometry for strongly interacting systems [31].

In conclusion, we have demonstrated a new technique to determine spin susceptibilities of ultracold atomic gases using speckle imaging. We have validated and calibrated this technique using an ideal Fermi gas and applied it to a strongly interacting Fermi gas in the BEC-BCS crossover. This technique is directly applicable to studying pairing and magnetic ordering of two-component gases in optical lattices.

We acknowledge Qijin Chen and Kathy Levin for providing calculations of condensate fraction, Gregory Astrakharchik and Stefano Giorgini for providing Monte Carlo results for the compressibility, Sandro Stringari and Alessio Recati for discussions, and Yong-il Shin for experimental assistance. This work was supported by NSF and the Office of Naval Research, AFOSR (through the MURI program), and under Army Research Office Grant No. W911NF-07-1-0493 with funds from the DARPA Optical Lattice Emulator program.

- 
- [1] S. Gupta *et al.*, *Science* **300**, 1723 (2003).
  - [2] C.A. Regal and D.S. Jin, *Phys. Rev. Lett.* **90**, 230404 (2003).
  - [3] J. Stenger *et al.*, *Phys. Rev. Lett.* **82**, 4569 (1999).
  - [4] T. Kitagawa *et al.*, arXiv:1001.4358.
  - [5] Z. Hadzibabic, S. Stock, B. Battelier, V. Bretin, and J. Dalibard, *Phys. Rev. Lett.* **93**, 180403 (2004).
  - [6] T. Jelts *et al.*, *Nature (London)* **445**, 402 (2007).
  - [7] T. Rom *et al.*, *Nature (London)* **444**, 733 (2006).
  - [8] M. Greiner *et al.*, *Phys. Rev. Lett.* **94**, 110401 (2005).
  - [9] N. Gemelke *et al.*, *Nature (London)* **460**, 995 (2009).
  - [10] W.S. Bakr *et al.*, *Science* **329**, 547 (2010).
  - [11] J.F. Sherson *et al.*, *Nature (London)* **467**, 68 (2010).
  - [12] T. Müller *et al.*, *Phys. Rev. Lett.* **105**, 040401 (2010).
  - [13] C. Sanner *et al.*, *Phys. Rev. Lett.* **105**, 040402 (2010).
  - [14] L.-M. Duan, E. Demler, and M.D. Lukin, *Phys. Rev. Lett.* **91**, 090402 (2003).
  - [15] A.B. Kuklov and B.V. Svistunov, *Phys. Rev. Lett.* **90**, 100401 (2003).
  - [16] A. Recati and S. Stringari, arXiv:1007.4504.
  - [17] G.M. Bruun *et al.*, *Phys. Rev. Lett.* **102**, 030401 (2009).
  - [18] N. Trivedi and M. Randeria, *Phys. Rev. Lett.* **75**, 312 (1995).
  - [19] C.-C. Chien and K. Levin, *Phys. Rev. A* **82**, 013603 (2010).
  - [20] J.W. Goodman, *Speckle Phenomena in Optics* (Ben Roberts and Company, Greenwood Village, CO, 2007).
  - [21] D. Hellweg *et al.*, *Phys. Rev. Lett.* **91**, 010406 (2003).
  - [22] L.D. Turner *et al.*, *Opt. Lett.* **29**, 232 (2004).
  - [23] Q. Chen, J. Stajic, and K. Levin, *Phys. Rev. Lett.* **95**, 260405 (2005).
  - [24] M. Greiner *et al.*, *Nature (London)* **426**, 537 (2003).
  - [25] M.W. Zwierlein *et al.*, *Phys. Rev. Lett.* **91**, 250401 (2003).
  - [26] W. Ketterle, D.S. Durfee, and D.M. Stamper-Kurn, in *Proceedings of the International School of Physics Enrico Fermi, Varenna, 1998* (IOS, Amsterdam, 1999).
  - [27] E.M. Lifshitz and L.P. Pitaevskii, *Statistical Physics Part 2, 3rd ed.*, Course of Theoretical Physics Vol. 9 (Pergamon Press Inc., Oxford, 1980);
  - [28] G.E. Astrakharchik, R. Combescot, and L.P. Pitaevskii, *Phys. Rev. A* **76**, 063616 (2007).
  - [29] E.D. Kuhnle *et al.*, *Phys. Rev. Lett.* **105**, 070402 (2010).
  - [30] C. Salomon (private communication).
  - [31] D. McKay and B. DeMarco, arXiv:1010.0198.
  - [32] G.E. Astrakharchik, J. Boronat, J. Casulleras, and S. Giorgini, *Phys. Rev. Lett.* **93**, 200404 (2004).



## Appendix C

# Correlations and Pair Formation in a Repulsively Interacting Fermi Gas

This appendix contains a reprint of Ref. [42]: Christian Sanner, Edward J. Su, Wujie Huang, Aviv Keshet, Jonathon Gillen, and Wolfgang Ketterle, *Correlations and Pair Formation in a Repulsively Interacting Fermi Gas*, Phys. Rev. Lett. **108**, 240404 (2012).

## Correlations and Pair Formation in a Repulsively Interacting Fermi Gas

Christian Sanner, Edward J. Su, Wujie Huang, Aviv Keshet, Jonathon Gillen, and Wolfgang Ketterle  
 MIT-Harvard Center for Ultracold Atoms, Research Laboratory of Electronics, and Department of Physics,  
 Massachusetts Institute of Technology, Cambridge, Massachusetts 02139, USA  
 (Received 9 August 2011; published 13 June 2012)

A degenerate Fermi gas is rapidly quenched into the regime of strong effective repulsion near a Feshbach resonance. The spin fluctuations are monitored using speckle imaging and, contrary to several theoretical predictions, the samples remain in the paramagnetic phase for an arbitrarily large scattering length. Over a wide range of interaction strengths a rapid decay into bound pairs is observed over times on the order of  $10\hbar/E_F$ , preventing the study of equilibrium phases of strongly repulsive fermions. Our work suggests that a Fermi gas with strong short-range repulsive interactions does not undergo a ferromagnetic phase transition.

DOI: [10.1103/PhysRevLett.108.240404](https://doi.org/10.1103/PhysRevLett.108.240404)

PACS numbers: 03.75.Ss, 67.85.Lm, 75.10.Lp

Many-body systems can often be modeled using contact interactions, greatly simplifying the analysis while maintaining the essence of the phenomenon to be studied. Such models are almost exactly realized with ultracold gases due to the large ratio of the de Broglie wavelength to the range of the interatomic forces [1]. For itinerant fermions with strong short-range repulsion, textbook calculations predict a ferromagnetic phase transition—the so-called Stoner instability [2].

Here we investigate this system using an ultracold gas of fermionic lithium atoms, and observe that the ferromagnetic phase transition does not occur. A previous experimental study [3] employing a different apparatus found indirect evidence for a ferromagnetic phase, but did not observe the expected domain structure, possibly due to the lack of imaging resolution. Here we address this shortcoming by analyzing density and spin density fluctuations via speckle imaging [4]. When spin domains of  $m$  atoms form, the spin density variance will increase by a factor of  $m$  [5], even if individual domains are not resolved. One main result of this paper is the absence of such a significant increase which seems to exclude the possibility of a ferromagnetic state in the studied system.

The Stoner model assumes a two-component Fermi gas with a repulsive short-range interaction described by a single parameter, the scattering length. The predicted phase transition to a ferromagnetic state requires large repulsive scattering lengths on the order of the interatomic spacing. They can be realized only by short-range *attractive* potentials with a loosely bound state with binding energy  $\hbar^2/(ma^2)$ , with  $m$  being the atomic mass and  $a$  being the scattering length [6]. However, as shown schematically in Fig. 1, the repulsive gas is then by necessity only metastable with respect to decay into the bound state. Many theoretical studies of a Fermi gas with strong short-range repulsive interactions assume that the metastable state is sufficiently long-lived [7–18]. In recent Monte Carlo simulations, the paired state is projected out in the

time evolution of the system [19,20]. Theoretical studies concluded that the pairing instability is somewhat faster than the ferromagnetic instability [21]. The second major result of this paper is to show that pair formation occurs indeed on a very short time scale. The measured time constant of  $10\hbar/E_F$  (where  $E_F$  is the Fermi energy) indicates that the metastable repulsive state will never reach equilibrium and that, even in a metastable sense, a Fermi gas with strong short-range repulsive interactions does not exist. The fast pair formation could not be observed previously due to limited time resolution [3]. Instead, a much slower second phase in the conversion of atoms to pairs was observed leading to the wrong conclusion that the unpaired atoms have a much longer lifetime.

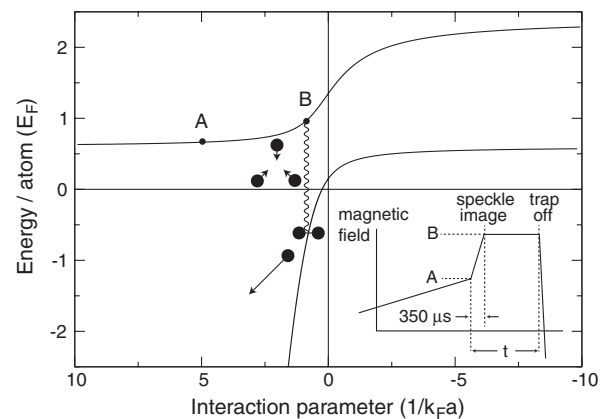


FIG. 1. Diagram showing energy levels and timing of the experiment. The upper (repulsive) and lower (attractive) branch energies, near a Feshbach resonance, are connected by three-body collisions. In our experiment, we quickly jump from a weakly interacting Fermi gas (A) to a strongly interacting one (B) with a rapid magnetic field change. The evolution of correlations and domains and the molecule formation (population of the lower branch) are studied as a function of hold time  $t$ . Adapted from [42].

The experiments were carried out with typically  $4.2 \times 10^5$   $^6\text{Li}$  atoms in each of the two lower spin states  $|1\rangle$  and  $|2\rangle$  confined in an optical dipole trap with radial and axial trap frequencies  $\omega_r = 2\pi \times 100(1) \text{ s}^{-1}$  and  $\omega_z = 2\pi \times 9.06(25) \text{ s}^{-1}$ . The sample was evaporatively cooled at a magnetic bias field  $B = 320 \text{ G}$ , identical to the procedure described in [22]. Then the magnetic field was slowly ramped to  $730 \text{ G}$  ( $k_F a = 0.35$ ) in  $500 \text{ ms}$ . The fraction of atoms being converted to molecules during the ramp was measured (see below for method) to be below  $5\%$ . The temperature of the cloud was typically  $0.23(3)T_F$  at  $527 \text{ G}$  with a Fermi energy of  $E_F = k_B T_F = h \times 6.1 \text{ kHz}$ . After rapidly switching the magnetic field from  $730 \text{ G}$  to the final value in less than  $350 \mu\text{s}$ , spin fluctuations were measured by speckle imaging. Optionally an appropriate rf pulse was applied directly before imaging to rotate the spin orientation along the measurement axis. Due to the use of  $20 \text{ cm}$  diameter coils outside the vacuum chamber, the inductance of the magnet coils was  $330 \mu\text{H}$  and the fast switching was accomplished by rapidly discharging capacitors charged to  $500 \text{ V}$ .

Experimentally, spin fluctuations are measured using the technique of speckle imaging described in Ref. [4]. For an appropriate choice of detuning, an incident laser beam experiences a shift of the refractive index proportional to the difference between the local populations of the two spin states  $N_1$  and  $N_2$ . Spin fluctuations create spatial fluctuations in the local refractive index and imprint a phase pattern into the incoming light, which is then converted into an amplitude pattern during propagation. The resulting spatial fluctuations in the probe laser intensity are used to determine the spin fluctuations in the sample.

In Ref. [4] we prepared samples on the lower branch of the Feshbach resonance, where positive values of  $k_F a$  correspond to a gas of weakly bound molecules. At  $k_F a = 1.2$ , we observed a sixfold suppression of spin fluctuations and a fourfold enhancement of density fluctuations. Typical fluctuations in the speckle images of a non-interacting Fermi gas at  $T = 0.23T_F$  amount to  $5\%$  of the average optical signal per pixel, corresponding to about  $50\%$  of Poissonian fluctuations. Those fluctuations are modified by factors between  $0.2$  and  $1.6$  due to pairing and interactions.

In this study, on the upper branch of the Feshbach resonance, the situation is reversed. For unbound atoms, as the interaction strength increases, the two spin components should develop stronger and stronger anticorrelations and enhanced spin fluctuations. Previous experimental work [3] and several theoretical studies [10,11,13–15,18,23] predicted a phase transition to a ferromagnetic state where the magnetic susceptibility and therefore the spin fluctuations diverge. Recent Monte Carlo simulations [19] predict such a divergence around  $k_F a = 0.83$ . We therefore expected an increase of spin fluctuations by one or several orders of magnitude, related to the size of magnetic domains.

Figure 2 shows the observed spin fluctuations enhancement compared to the non-interacting cloud at  $527 \text{ G}$ . The variance enhancement factor reaches its maximum value of  $1.6$  immediately after the quench, decreasing during the  $2 \text{ ms}$  afterward. The absence of a dramatic increase shows that no domains form and that the sample remains in the paramagnetic phase throughout. Similar observations were made for a wide range of interaction strengths and wait times. Note that first-order perturbation theory [24] predicts an increase of the susceptibility by a factor of  $1.5$  at  $k_F a = 0.5$  and by a factor of  $2$  at  $k_F a = 0.8$  (i.e., no dramatic increase for  $k_F a < 1$ ). Therefore, our data show no evidence for the Fermi gas approaching the Stoner instability.

Before we can fully interpret these findings, we have to take into account the decay of the atomic sample on the upper branch of the Feshbach resonance into bound pairs. We characterize the pair formation by comparing the total number of atoms and molecules  $N_a + 2N_{\text{mol}}$  (determined by taking an absorption image after ballistic expansion at high magnetic field where molecules and atoms have the same absorption resonance) to the number of free atoms (determined by rapidly sweeping the magnetic field to  $5 \text{ G}$  before releasing the atoms and imaging the cloud, converting pairs into deeply bound molecules that are completely shifted out of resonance) [25].

The time evolution of the molecule production (Fig. 3) shows two regimes of distinct behavior. For times less than  $1 \text{ ms}$ , we observe a considerable number of atoms converted into molecules, while the total number  $N_a + 2N_{\text{mol}}$  remains constant. The initial drop in atom number becomes larger as we increase the final magnetic field, and saturates at around  $50\%$  near the Feshbach resonance.

We attribute this fast initial decay in atom number to recombination [26,27] into the weakly bound molecular

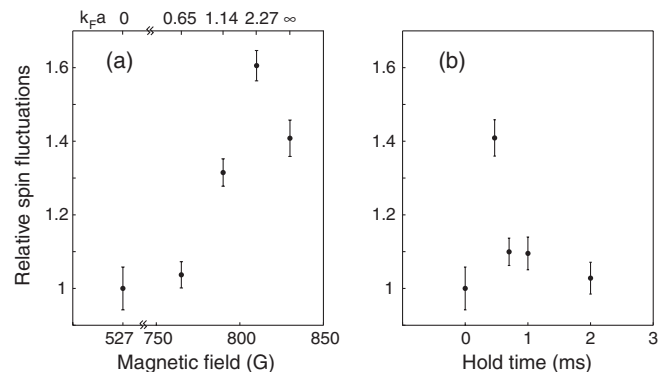


FIG. 2. Spin fluctuations (a) after  $350 \mu\text{s}$  as a function of magnetic field and (b) on resonance as a function of hold time scaled to the value measured at  $527 \text{ G}$ . Even at strong repulsive interactions, the measured spin fluctuations are barely enhanced, indicating only short-range correlations and no domain formation. The spin fluctuations were determined for square bins of  $2.6 \mu\text{m}$ , each containing on average  $1000$  atoms per spin state.

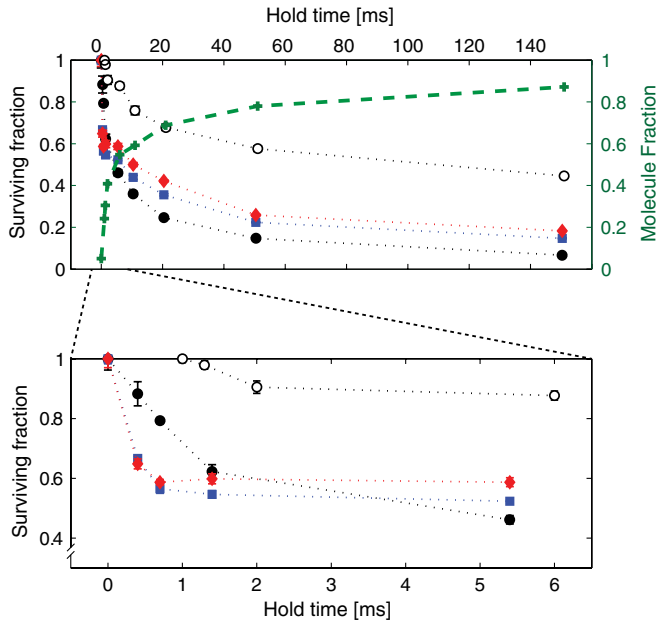


FIG. 3 (color online). Characterization of molecule formation at short and long hold times, and at different values of the interaction strength. The closed symbols, circles (black) at 790 G with  $k_F a = 1.14$ , squares (blue) at 810 G with  $k_F a = 2.27$  and diamonds (red) at 818 G with  $k_F a = 3.5$  represent the normalized number of free atoms, the open symbols the total number of atoms including those bound in Feshbach molecules (open circles at 790 G with  $k_F a = 1.14$ ). The crosses (green) show the molecule fraction. The characteristic time scale is set by the Fermi time  $\hbar/E_F = 43 \mu\text{s}$ , calculated with a cloud averaged Fermi energy.

state. We obtain an atom loss rate  $\dot{N}_a/N_a = 250 \text{ s}^{-1}$  at 790 G in the first 1 ms after the magnetic field switch. Assuming a three-body process we estimate the rate coefficient  $L_3$  at this field to be  $3.9 \times 10^{-22} \text{ cm}^6 \text{ s}^{-1}$ , though the interaction is already sufficiently strong for many-body effects to be significant. For stronger interactions, about 30% of atom loss occurs already during the relevant 100  $\mu\text{s}$  of ramping through the strongly interacting region, indicating a lower bound of around  $3 \times 10^3 \text{ s}^{-1}$  for the loss rate which is 13% of the inverse Fermi time  $E_F/\hbar$ , calculated with a cloud averaged Fermi energy.

After the first millisecond, the molecule formation rate slows down, by an order of magnitude at a magnetic field of 790 G (and even more dramatically at higher fields) when it reaches about 50%. It seems likely that the molecule fraction has reached a quasi-equilibrium value at the local temperature, which is larger than the initial temperature due to local heating accompanying the molecule formation. Reference [28] presents a simple model for the equilibrium between atoms and molecules (ignoring strong interactions). For phase space densities around unity and close to resonance, the predicted molecule fraction is 0.5, in good agreement with our observations [29].

For longer time scales (hundred milliseconds) we observe a steady increase of the molecule fraction to 90% for the longest hold time. This occurs due to continuous evaporation which cools down the system and shifts the atom-molecule equilibrium towards high molecule fractions. During the same time scale, a slow loss in both atom number and total number is observed caused by inelastic collisions (vibrational relaxation of molecules) and evaporation loss.

Is the rapid conversion into molecules necessarily faster than the evolution of ferromagnetic domains? Our answer is tentatively yes. First, for strong interactions with  $k_F a$  around 1, one expects both instabilities (pair formation and Stoner instability) to have rates which scale with the Fermi energy  $E_F$  and therefore with  $n^{2/3}$ . Therefore, one cannot change the competition between the instabilities by working at higher or lower densities. According to Ref. [21] the fastest unstable modes for domain formation have a wave vector  $q \approx k_F/2$  and grow at a rate of up to  $E_F/4\hbar$  when the cloud is quenched sufficiently far beyond the critical interaction strength. Unstable modes with such wave vectors will develop “domains” of half a wavelength or size  $\xi = \pi/q = 2\pi/k_F$  containing 5 atoms per spin state in a volume  $\xi^3$ . This rate is comparable to the observed conversion rates into pairs of  $0.13E_F$ . Therefore, at best, “domains” of a few particles could form, but before they can grow further and prevent the formation of pairs (in a fully polarized state), rapid pair formation takes over and populates the lower branch of the Feshbach resonance. Based on our observations and these arguments, it seems that it is not possible to realize ferromagnetism with strong short range interaction, and therefore the basic Stoner model cannot be realized in nature.

One possibility to suppress pair formation is provided by narrow Feshbach resonances. Here the pairs have dominantly closed channel character and therefore a much smaller overlap matrix element with the free atoms. However, narrow Feshbach resonances are characterized by a long effective range and do not realize the Stoner model which assumes short-range interactions. Other interesting topics for future research on ferromagnetism and pair formation include the effects of dimensionality [30,31], spin imbalance [32,33], mass imbalance [34], lattice and band structure [35,36].

We now discuss whether ferromagnetism is possible *after* atoms and molecules have rapidly established local equilibrium. In other words, starting at  $T = 0$ , one could heat up the fully paired and superfluid system and create a gas of atomic quasiparticles which are similar to free atoms with repulsive interactions. Density and temperature of the atoms are now coupled. It is likely that such a state is realized in our experiments after a few ms following the quench, until evaporative cooling converts the system into a molecular condensate over  $\approx 100 \text{ ms}$ . The possibility that such a quasiparticle gas could become ferromagnetic

has not been discussed in the literature. Our experiments do not reveal any major increase in spin fluctuations which seems to exclude a ferromagnetic state. In the simplest picture, we could regard the atomic quasiparticles as free atoms, and then apply the Stoner model to them. Ferromagnetic domain formation is analogous to phase separation between the two spin components [3]. Since dimers interact equally with the two spin components, one might expect that even a noticeable dimer fraction should not suppress the tendency of the atomic gas to form domains. Therefore, in a simple model, one may neglect dimer-atom interactions.

If the Stoner model applies to this quasiparticle gas, the next question is whether the temperature is low enough for the ferromagnetic phase transition. Available theoretical treatments do not predict an exact maximum transition temperature to the ferromagnetic state and obtain an unphysical divergence for large scattering lengths. Since the only energy scale is the Fermi temperature, one would expect a transition temperature which is a fraction of the Fermi temperature [37], higher or around the temperature scale probed in our experiments. However, even above the transition temperature, the susceptibility is enhanced. A simple Weiss mean field or Stoner model leads to the generic form of the susceptibility  $\chi(T) = \chi_0(T)/(1 - w\chi_0(T))$ , where  $\chi_0(T)$  is the Pauli susceptibility of the non-interacting gas and  $w$  the interaction parameter. This formula predicts a twofold increase in the susceptibility even 50% above the transition temperature, which is well within the sensitivity of our measurements.

Therefore, our experiment can rule out ferromagnetism for temperatures even slightly lower than the experimental temperatures. Temperatures are very difficult to measure in a transient way for a dynamic system which may not be in full equilibrium. For example, cloud thermometry requires full equilibration and lifetimes much longer than the longest trap period. We attempted to measure the temperature after the hold time near the Feshbach resonance by quickly switching the magnetic field to weak interactions at 527 G and then performing noise thermometry using speckle imaging [4]. We measure column-integrated fluctuations that are 0.61(8) of the Poisson value which implies an effective temperature well below  $T_F$ , around 0.33(7)  $T_F$ , not much higher than our initial temperature of 0.23  $T_F$ . Although the cloud is not in full equilibrium, an effective local temperature can still be obtained from noise thermometry.

Alternatively, we can estimate the temperature increase from the heat released by pair formation. A simple model [38] accounting for the relevant energy contributions predicts for  $k_F a = 1$  that molecule fractions of higher than 20% result in a final temperature above 0.4 $T_F$ , an estimate which is higher than the measurement reported above. One may hope that closer to resonance many-body

effects lower the released energy; however, as we show in the Supplemental Material (Fig. 1 of [38]) this is not necessarily the case due to the repulsive interaction energy.

Our experiment has not shown any evidence for a possible ferromagnetic phase in an atomic gas in “chemical” equilibrium with dimers. This implies one of the following possibilities. (i) This gas can be described by a simple Hamiltonian with strong short range repulsion. However, this Hamiltonian does not lead to ferromagnetism. This would be in conflict with the results of recent quantum Monte Carlo simulations [19,20] and second order perturbation theory [11], and in agreement with conclusions based on Tan relations [39]. (ii) The temperature of the gas was too high to observe ferromagnetism. This would then imply a critical temperature around or below 0.2 $T/T_F$ , lower than generally assumed. (iii) The quasiparticles cannot be described by the simple model of an atomic gas with short-range repulsive interactions due to their interactions with the paired fraction.

A previous experiment [3] reported evidence for ferromagnetism by presenting non-monotonic behavior of atom loss rate, kinetic energy and cloud size when approaching the Feshbach resonance, in agreement with predictions based on the Stoner model. Our measurements confirm that the properties of the gas strongly change near  $k_F a = 1$ . Similar to [3], we observe features in kinetic and release energy measurements near the resonance (see Supplemental Material [38]). However, the behavior is more complex than that captured by simple models. The atomic fraction decays non-exponentially (see Fig. 3), and therefore an extracted decay time will depend on the details of the measurement such as time resolution. Reference [3] found a maximum of the loss rate of 200  $s^{-1}$  for a Fermi energy of 28 kHz. Our lower bound of the decay rate of  $3 \times 10^3 s^{-1}$  is 15 times faster at a five times smaller Fermi energy. Our more detailed study rules out that Ref. [3] has observed ferromagnetic behavior.

Our conclusion is that an ultracold gas with strong short range repulsive interactions near a Feshbach resonance remains in the paramagnetic phase. The fast formation of molecules and the accompanying heating makes it impossible to study such a gas in equilibrium, confirming predictions of a rapid conversion of the atomic gas to pairs [21,40]. The Stoner criterion for ferromagnetism obtains when the effective interaction strength times the density of states is larger than one. This is at least an approximately valid criterion for multi-band lattice models [41]. We have shown here that this criterion cannot be applied to Fermi gases with short-range repulsive interactions (the basic Stoner model) since the neglected competition with pairing is crucial.

This work was supported by NSF and ONR, AFOSR MURI, and under ARO Grant No. W911NF-07-1-0493 with funds from the DARPA Optical Lattice Emulator

program. We are thankful to Eugene Demler, David Pekker, Boris Svistunov, Nikolay Prokof'ev, and Wilhelm Zwerger for valuable discussions and to David Weld for critical reading of the manuscript.

- 
- [1] W. Ketterle and M. W. Zwierlein, in *Proceedings of the International School of Physics "Enrico Fermi,"* Course CLXIV (IOS, Amsterdam, 2007).
- [2] D. W. Snoke, *Solid State Physics: Essential Concepts* (Addison-Wesley, San Francisco, 2008).
- [3] G.-B. Jo, Y.-R. Lee, J.-H. Choi, C. A. Christensen, T. H. Kim, J. H. Thywissen, D. E. Pritchard, and W. Ketterle, *Science* **325**, 1521 (2009).
- [4] C. Sanner, E. J. Su, A. Keshet, W. Huang, J. Gillen, R. Gommers, and W. Ketterle, *Phys. Rev. Lett.* **106**, 010402 (2011).
- [5] This is illustrated by a simplified model assuming Poissonian fluctuations in a given probe volume within the atom sample. With on average  $N$  atoms in this volume, one would measure a standard deviation in the atom number of  $\sqrt{N}$ . However, if the atoms formed clusters each made of  $m$  atoms, the standard deviation of the number of clusters would be  $\sqrt{N/m}$ , leading to a variance in atom number of  $(m\sqrt{N/m})^2 = mN$ .
- [6] Potentials with a positive scattering length  $a$  have no bound state only if the effective range  $r_e$  is larger than  $a/2$ . Otherwise, the  $s$ -wave scattering amplitude  $f(k) = 1/(-1/a + r_e k^2/2 - ik)$  has a pole on the imaginary axis corresponding to a bound state.
- [7] M. Houbiers, R. Ferwerda, H. T. C. Stoof, W. I. McAlexander, C. A. Sackett, and R. G. Hulet, *Phys. Rev. A* **56**, 4864 (1997).
- [8] M. Amoruso, I. Meccoli, A. Minguzzi, and M. P. Tosi, *Eur. Phys. J. D* **7**, 441 (1999).
- [9] L. Salasnich, B. Pozzi, A. Parola, and L. Reatto, *J. Phys. B* **33**, 3943 (2000).
- [10] T. Sogo and H. Yabu, *Phys. Rev. A* **66**, 043611 (2002).
- [11] R. A. Duine and A. H. MacDonald, *Phys. Rev. Lett.* **95**, 230403 (2005).
- [12] H. Zhai, *Phys. Rev. A* **80**, 051605 (2009).
- [13] G. J. Conduit and B. D. Simons, *Phys. Rev. Lett.* **103**, 200403 (2009).
- [14] L. J. LeBlanc, J. H. Thywissen, A. A. Burkov, and A. Paramekanti, *Phys. Rev. A* **80**, 013607 (2009).
- [15] I. Berdnikov, P. Coleman, and S. H. Simon, *Phys. Rev. B* **79**, 224403 (2009).
- [16] X. Cui and H. Zhai, *Phys. Rev. A* **81**, 041602 (2010).
- [17] S. Zhang, H. Hung, and C. Wu, *Phys. Rev. A* **82**, 053618 (2010).
- [18] H. Heiselberg, *Phys. Rev. A* **83**, 053635 (2011).
- [19] S. Pilati, G. Bertaina, S. Giorgini, and M. Troyer, *Phys. Rev. Lett.* **105**, 030405 (2010).
- [20] S.-Y. Chang, M. Randeria, and N. Trivedi, *Proc. Natl. Acad. Sci. U.S.A.* **108**, 51 (2010).
- [21] D. Pekker, M. Babadi, R. Sensarma, N. Zinner, L. Pollet, M. W. Zwierlein, and E. Demler, *Phys. Rev. Lett.* **106**, 050402 (2011).
- [22] C. Sanner, E. J. Su, A. Keshet, R. Gommers, Y. Shin, W. Huang, and W. Ketterle, *Phys. Rev. Lett.* **105**, 040402 (2010).
- [23] M. Sandri, A. Minguzzi, and F. Toigo, *Europhys. Lett.* **96**, 66004 (2011).
- [24] A. Recati and S. Stringari, *Phys. Rev. Lett.* **106**, 080402 (2011).
- [25] S. Jochim, M. Bartenstein, A. Altmeyer, G. Hendl, C. Chin, J. Hecker Denschlag, and R. Grimm, *Phys. Rev. Lett.* **91**, 240402 (2003).
- [26] C. Chin, R. Grimm, P. Julienne, and E. Tiesinga, *Rev. Mod. Phys.* **82**, 1225 (2010).
- [27] G. J. Conduit and E. Altman, *Phys. Rev. A* **83**, 043618 (2011).
- [28] C. Chin and R. Grimm, *Phys. Rev. A* **69**, 033612 (2004).
- [29] Note that the drop in molecule formation after 1 ms cannot be explained by the drop in atomic density by a factor of 2 due to conversion into molecules and to an increase in the size of the sample due to the increased repulsive interactions.
- [30] N. D. Drummond, N. R. Cooper, R. J. Needs, and G. V. Shlyapnikov, *Phys. Rev. B* **83**, 195429 (2011).
- [31] V. Pietilä, D. Pekker, Y. Nishida, and E. Demler, *Phys. Rev. A* **85**, 023621 (2012).
- [32] X.-J. Liu and H. Hu, *Phys. Rev. A* **82**, 043626 (2010).
- [33] H. Dong, H. Hu, X.-J. Liu, and P. D. Drummond, *Phys. Rev. A* **82**, 013627 (2010).
- [34] C. W. von Keyserlingk and G. J. Conduit, *Phys. Rev. A* **83**, 053625 (2011).
- [35] C.-C. Chang, S. Zhang, and D. M. Ceperley, *Phys. Rev. A* **82**, 061603 (2010).
- [36] G. Carleo, S. Moroni, F. Becca, and S. Baroni, *Phys. Rev. B* **83**, 060411 (2011).
- [37] X.-J. Liu, H. Hu, and P. D. Drummond, *Phys. Rev. A* **82**, 023619 (2010).
- [38] See Supplemental Material at <http://link.aps.org/supplemental/10.1103/PhysRevLett.108.240404> for a discussion of cloud release energy and heating due to molecule formation.
- [39] M. Barth and W. Zwerger, *Ann. Phys. (N.Y.)* **326**, 2544 (2011).
- [40] S. Zhang and T.-L. Ho, *New J. Phys.* **13**, 055003 (2011).
- [41] J. Bünemann, W. Weber, and F. Gebhard, *Phys. Rev. B* **57**, 6896 (1998).
- [42] L. Pricoupenko and Y. Castin, *Phys. Rev. A* **69**, 051601 (2004).

# Correlations and Pair Formation in a Repulsively Interacting Fermi Gas: Supplementary Information

In this supplement we present measurements of the release energy of fermions with strong repulsive interactions, derive estimates for sample heating due to molecule formation, adapt predictions for ferromagnetic domain formation after a quench to our experimental parameters, and discuss our temporal and spatial resolution for spin fluctuations.

## KINETIC ENERGY AND RELEASE ENERGY

The energy of a trapped interacting gas is the sum of three contributions: the kinetic energy, the interaction energy, and the potential energy in the trapping potential.

$$E = T + U_{\text{int}} + U_{\text{trap}} \quad (1)$$

By suddenly releasing the atoms from the trap and measuring the radius of the cloud, it is possible to measure either the release energy ( $T + U_{\text{int}}$ ) or the kinetic energy  $T$ , depending on whether the interactions are left on or are switched off, respectively, at the time of release, by leaving the external magnetic field constant or rapidly switching it to a value away from the Feshbach resonance.

The system is prepared with variable interaction strength by rapidly switching the magnetic field to a value near the Feshbach resonance. For the kinetic energy measurement, the field is again rapidly switched to 5G, after which the atoms are released from the trap. After 8 ms of free expansion, the size of the cloud reflects the width of the in-trap momentum distribution and the average in-trap kinetic energy. The observed increase in kinetic energy with increasing interaction strength reflects the onset of pair (anti-)correlations of opposite-spin atoms — those anti-correlations reduce the repulsive potential energy at the price of increased kinetic energy. The observed increase in kinetic energy is consistent with the observations in Ref. [3]. We do not observe a minimum in kinetic energy as in [3], since the interactions are suddenly increased and the cloud cannot adiabatically expand during the ramp as was the case in the earlier work. For fully spin-polarized domains, the kinetic energy would increase by a factor of  $2^{2/3}$  which provides an upper bound (since the true ground state must have an energy lower than or equal to the fully phase-separated state). The smaller observed energy increase (factor of 1.3) implies that fully spin polarized domains have not formed. It should be noted that the kinetic energy increase is insensitive to the correlation length or size of

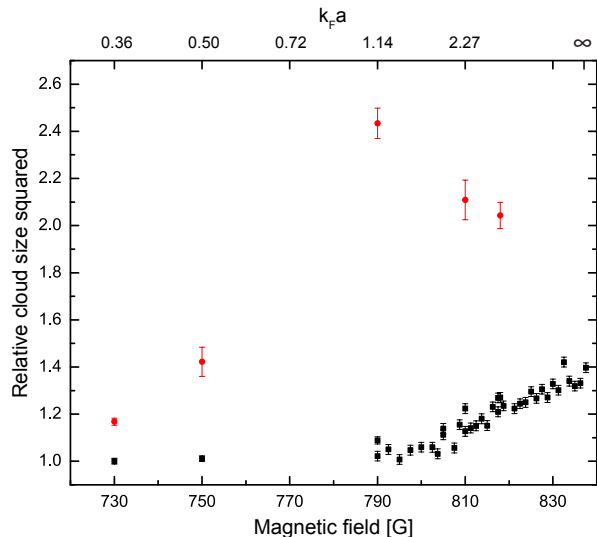


FIG. 1: Measured transverse mean square cloud size after time-of-flight expansion as a function of the interaction strength before the release in units of the value of the non-interacting cloud. The interactions are switched off (squares) or left on (circles) at the time of release. For sufficiently long time-of-flight the transverse 2D release energy is directly proportional to the measured mean square width of the cloud. The expansion is either isotropic (in the case of switched off interactions) or mostly transverse (in case of strong interactions leading to hydrodynamic expansion) [1, 2]. Uncertainties as indicated by the error bars are purely statistical.

domains and cannot clearly distinguish between ferromagnetic domains and strong anti-correlations [4, 5].

In-trap kinetic and interaction energies are measured when the magnetic field is left at its value near the Feshbach resonance while the trap is switched off. After 4 ms of the 8 ms free expansion the field is switched to 5G for imaging. The resulting cloud size is directly related to the release energy of the cloud, the sum of the in-trap kinetic and interaction energies. Around  $k_F a = 0.5$ , we observe a strong increase of the transverse release energy by a factor of about 2. This implies that the total energy has increased by a factor of  $4/3$  compared to the non-interacting case since the interactions modify the expansion from ballistic to hydrodynamic. The comparison of kinetic energy and release energy at 790G and 810G shows that the extra energy due to repulsive interactions is clearly dominated by repulsive potential energy and not by kinetic energy. The latter would occur for ferromagnetic domains. In case of fully spin-polarized domains, the repulsive interaction energy would vanish, and

kinetic energy and release energy should be the same. Therefore, the energy measurements also rule out a ferromagnetic phase.

The interaction-strength dependence of the release energy shows a weak maximum at 790G. The ground state energy has to vary monotonically with the strength of the repulsive interactions. This follows from a simple variational argument where the exact ground state wavefunction at strong interactions is used as a trial wavefunction at weaker interactions. Therefore, the observed maximum is most likely related to non-equilibrium excitations caused by the sudden jump in the scattering length.

### HEATING DUE TO MOLECULE FORMATION

Molecule formation heats the sample by transferring the binding energy and excess kinetic energy of the molecules to the remaining atoms, and also by creating holes in the Fermi sea. For small values of  $k_F a$ , the total energy release per molecule is  $\hbar^2/ma^2 + 2E_F$ . From the energy per particle for an ideal homogeneous degenerate Fermi gas  $E = 0.6E_F[1 + (5\pi^2/12)(T/T_F)^2]$  we obtain

$$\frac{T}{T_F} = \sqrt{\frac{4\eta}{\pi^2} \left(1 + \frac{1}{(k_F a)^2}\right)} \quad (2)$$

for the final temperature with a small molecule fraction  $\eta$  (assuming initially  $\eta=0$  and  $T=0$ ). Evaluating this result at  $k_F a = 1$ , where the two-body binding energy is  $2E_F$ , one finds that molecule fractions of higher than 20 % result in a final temperature above  $0.4T_F$ , an estimate which is somewhat higher than the measurement reported in the main article.

### DOMAIN GROWTH PREDICTIONS AND EXPERIMENTAL RESOLUTION

As described in the main paper, we have observed two dynamic time scales - a sub-ms timescale for rapid pair formation, followed by a slower time scale of tens of milliseconds where further cooling led to a full conversion of the atomic into a molecular gas. We now want to discuss over what time scale we could have observed ferromagnetic domain formation if it had happened, and some experimental aspects regarding temporal and spatial resolution.

Pekker et al. [6] predicted in uniform systems fast growth rates for small domains. Unstable modes with wavevector  $q \approx k_F/2$  grow at a rate of up to  $E_F/4\hbar$  when the cloud is quenched sufficiently far beyond the critical interaction strength. This corresponds to a growth time of around  $100\mu\text{s}$ . For a wide range of interactions

and wavevectors, the predicted growth time is faster than  $10\hbar/E_F$  or  $250\mu\text{s}$ . During this time one would expect the thermal fluctuations to increase by a factor of  $e$ .

Wavevectors  $q \approx k_F/2$  will develop “domains” of half a wavelength or size  $\xi = \pi/q = 2\pi/k_F$ , which is  $2.3\mu\text{m}$  at the experimental density of  $3 \times 10^{11} \text{ cm}^{-3}$  corresponding to  $k_F = 2.7 \times 10^4 \text{ cm}^{-1}$ . For speckle imaging the smallest effective probe volume is given by the nominal optical resolution or the optical wavelength times the aperture of the lens system which is equal to the bin size of  $2.6\mu\text{m}$  in our experiment. For a bin size  $d$ , the measured fluctuations are an integral over fluctuations at all wavevectors  $q$  with an effective cutoff around  $1/d$ . Due to a mode density factor  $q^2$  the largest contribution comes from wavevectors around  $\pi/d$  which is equal to  $0.4 k_F$  for our experimental parameters, fortuitously close to the wavevector of the fastest growing unstable modes. Therefore, for a quench across a ferromagnetic phase transition, we would have expected a sub-millisecond growth time for the spin fluctuations, which was not observed.

Another analysis focuses on domains. As discussed in the main paper, random domains containing  $m$  atoms will increase the variance of spin fluctuations by a factor of  $m$ . The fastest growing unstable modes contain around 5 atoms per spin state in a volume  $\xi^3$ . At our temperatures, the thermal fluctuations correspond to Poisson fluctuations reduced by the Pauli suppression factor  $(3/2)T/T_F$ , i.e. in a small volume with about ten particles, the spin fluctuations correspond to plus/minus one particle, and will approach saturation (i.e. fully spin polarized domains) after a few growth times (when, of course, the unstable mode analysis is no longer applicable). If these domains randomize through spin diffusion, it will increase the variance of the spin fluctuations at *all* length scales larger than  $\xi$  by a factor of  $m$ , without requiring optical resolution of the domain size  $\xi$ . Spin diffusion effectively “converts” initial fluctuations at wavevector  $q$  to fluctuations at all wavevectors smaller than  $q$ .

Since we start with a balanced two-state mixture with zero spin density, formation of random (i.e. uncorrelated) domains requires spin diffusion. Full sensitivity to domains requires spin transport over a distance equal to the bin size. Assuming diffusive motion at resonant interactions with a spin diffusivity  $D_s \approx \hbar/m$  as observed in [7] results in a corresponding minimum wait time of about  $300\mu\text{s}$ . This means that after crossing a ferromagnetic phase transition, formation of domains of a few to tens of particles should have occurred on ms scales and should have resulted in an observable increase of spin fluctuations. Therefore, we conclude that we have not entered any ferromagnetic phase within our experimental parameters.

- 
- [1] K. M. O'Hara, S. L. Hemmer, M. E. Gehm, S. R. Granade, and J. E. Thomas, *Science* **298**, 2179 (2002).
- [2] C. Menotti, P. Pedri, and S. Stringari, *Phys. Rev. Lett.* **89**, 250402 (2002).
- [3] G.-B. Jo et al., *Science* **325**, 1521 (2009).
- [4] H. Zhai, *Phys. Rev. A* **80**, 051605 (2009).
- [5] G.-B. Jo et al., arXiv:0910.3419v2 (2009).
- [6] D. Pekker et al., *Phys. Rev. Lett.* **106**, 050402 (2011).
- [7] A. Sommer, M. Ku, G. Roati, and M. W. Zwierlein, *Nature* **472**, 201 (2011).



# Appendix D

## Kapitza-Dirac Diffraction Simulation

```
% Kapitza-Dirac Diffraction

%Parameters
Va=20; %lattice depth in recoils
k=0; %starting momentum in lattice recoils
t=0:.001:0.4; % time (x axis) in units of 1/f_recoil
% Li recoil 29.2 KHz, Na recoil 7.6 KHz

k_numpts=200; % number of orders to calculate
k_numshow=3; % number of orders to show

Pi=3.14159265;
e=2.71828;

%Diagonalize Hamiltonian Matrix

k_mid=ceil(k_numpts/2);
H=zeros(k_numpts);
for ii=1:k_numpts
    H(ii,ii) = (k+2*(ii-k_mid))^2;
    if ii>1
        H(ii,ii-1) = Va/4;
    end
    if ii<k_numpts
        H(ii,ii+1) = Va/4;
    end
end

[V,E]=eig(H);
Ex=2*Pi*li*diag(E)*t;
expEx=e.^Ex;
Vproj=V*diag(V(k_mid,:));

Vprop=abs(Vproj*expEx).^2;
Vshow=Vprop(k_mid:k_mid+k_numshow,:);
FigHandle = figure('Position', [200, 200, 600, 300]);
```

```
%Generate plots

plot(t*1000/7.6,Vshow); % IR
%plot(t*1000/30.4,Vshow); % Green

title( sprintf( 'Lattice Depth of %d E_R', Va ) );
xlabel('Pulse Duration / us');
xlim([0 52]);
ylim([0 1]);
ylabel('Relative Strength');
hold on;
```



# Appendix E

## Superlattice Band Structure Calculation

```
% Superlattice Band Structure Calculation
clearvars;

% Calculate the Band Structure

V1 = 40; %in the unit of E_IR
V2 = 10; %in the unit of E_Green
phi = 0.5; %in the unit of 2*pi. (nearest symmetric points
are -0.5 and 0.5)

lc=1:1:200;%1BZ is discretized into 2000 parts, which is
also the number of the sites involved in the calculation;
for l=1:length(lc)
    q(l)=lc(l)/100-1;%[-1,1], momentum scale : PI()/a

%Creating H on the basis of plain wave;
N=51; %must be odd;
h=zeros(N,N);
c1=1:1:N;
c2=1:1:N;
for c11=1:length(c1)
for c12=1:length(c2)
    switch c11-c12
        case 0
            h(c11,c12)=(q(l)-((N+1)/2-c11)*2)^2;
        case 1
            h(c11,c12)=-V1/4;
        case -1
            h(c11,c12)=-V1/4;
        case 2
            h(c11,c12)=-(4*V2*exp(2*1i*phi*pi))/4;
        case -2
            h(c11,c12)=-(4*V2*exp(-2*1i*phi*pi))/4;
        otherwise
            h(c11,c12)=0;
    end
end
end
```

```
end

[V,D] = eig(h); %E(q(1)) for different bands in a column;
ge(:,l) = D*ones(51,1);

    if l==100
        Band_mid = abs(V).^2;
    end
    if l==200
        Band_edge = abs(V).^2;
    end
end
k = lc(101:200)/100-1;
bands = ge(1:4,101:200);

center = median(bands');
zero = center(1);
width = range(bands');

% Plot Superlattice Band Structure
figure;
plot(k,ge(1,101:200)-zero); hold on;
plot(k,ge(2,101:200)-zero); hold on;
plot(k,ge(3,101:200)-zero); hold on;
plot(k,ge(4,101:200)-zero); hold on;
plot(k,ge(5,101:200)-zero); hold on;
plot(k,ge(6,101:200)-zero); hold on;

% Plot Quasi-momentum States

x = -5:2:7;
FigHandle = figure('Position', [200, 200, 800, 400]);
subplot(1,3,1);
bar(x,Band_edge(23:29,1));ylim([0 1]);
subplot(1,3,2);
bar(x,Band_edge(23:29,2));ylim([0 1]);
```

```

subplot(1,3,3);
bar(x,Band_edge(23:29,3));ylim([0 1]);

% x = -6:2:6;
% FigHandle = figure('Position', [200, 200, 800, 400]);
% subplot(1,3,1);
% bar(x,Band_mid(23:29,1));ylim([0 1]);
% subplot(1,3,2);
% bar(x,Band_mid(23:29,2));ylim([0 1]);
% subplot(1,3,3);
% bar(x,Band_mid(23:29,3));ylim([0 1]);

%% Plotting the Potential

x2 = -0.1:0.001:1.1;
r = (x2+0.5)*pi;
y2 = -V1/2*cos(2*r)-4*V2/2*cos(4*r+phi*2*pi);
y1 = center'*ones(size(x2));

figure;
plot(x2, y2-zero, 'Color',[0.2,0.9,0.1]); hold on;
plot(x2, y1(1,:)-zero, 'linewidth',width(1), 'Color',[0.9,0.1,0.1]);
plot(x2, y1(2,:)-zero, 'linewidth',width(2), 'Color',[0,0.1,0.9]);
plot(x2, y1(3,:)-zero, 'linewidth',width(3), 'Color',[0.4,0.4,0.3]);
plot(x2, y1(4,:)-zero, 'linewidth',width(4), 'Color',[0.4,0.4,0.3]);
xlim([-0.1 1.1])
ylim([-20 60])

title(['V_R = ',num2str(V1),'E_{IR}, V_G = ',num2str(V2),'E_{G}, \phi = ', num2str(2*phi),'\pi'])
ylabel('E/E_{IR}')

```

# Appendix F

## Simulation of Double-Slit Interference Pattern in a Superlattice

```
% Simulate Double-Slit Pattern in Superlattices

clear;
x = -0.3:0.000001:0.3;
oneslit = 5;           % single slit size
multislit = 10;       % distance between nearest
double-wells
doubleslit = multislit/2; % distance between left and
right wells
Ramanslit = 20;      % Raman coupling period, for 1064nm
light it is twice double-well spacing

N = 50;      % total number of double-wells
Raman_phi = pi; % Raman phase between nearest double-
wells, always pi
LR_phase = 0*pi; % relative phase between left and right

% calculate relative phases

c=sin(x*3.1/2);
oneslit_phase = pi*oneslit*c;
multislit_phase = pi*multislit*c;
Ramanslit_phase = pi*Ramanslit*c;

%% k=0 component

zero_k_db_phase= 2*pi*doubleslit*c + LR_phase;

I_k0 = (cos(zero_k_db_phase/2)).^2.*(sin
(N*multislit_phase)./sin(multislit_phase)).^2.*(sin
(oneslit_phase)./oneslit_phase).^2;

% k=+/-k_L Spin-Orbit-Coupling, also Onsite-Coupling with
```

```
100/0 population
```

```
Raman_phase = 2*pi*multislit*c + Raman_phi;
```

```
I_SOC = (cos(Raman_phase/2)).^2.*(sin(N*Ramanslit_phase).  
/sin(Ramanslit_phase)).^2.*(sin(oneslit_phase).  
/oneslit_phase).^2;
```

```
%% k=+/-k_L Onsite-Coupling with 50/50 population
```

```
finite_k_db_phase = 2*pi*doubleslit*c + LR_phase + pi/2;  
Raman_phase = 2*pi*multislit*c + Raman_phi;
```

```
I_OC = (cos(finite_k_db_phase/2)).^2.*(cos(Raman_phase/2)).  
^2.*(sin(N*Ramanslit_phase)./sin(Ramanslit_phase)).^2.*(sin  
(oneslit_phase)./oneslit_phase).^2;
```

```
%% Equal OC and SOC with 50/50 population (simplified)
```

```
OC_phase = 2*pi*doubleslit*c + LR_phase + pi/2;  
SOC_phase = 2*pi*doubleslit*c + pi/4;
```

```
I_Both = 0.5*(3/2+cos(SOC_phase)+cos(OC_phase)+cos  
(OC_phase-SOC_phase)).*(cos(Raman_phase/2)).^2.*(sin  
(N*Ramanslit_phase)./sin(Ramanslit_phase)).^2.*(sin  
(oneslit_phase)./oneslit_phase).^2;
```

```
%% plot the interference pattern
```

```
FigHandle = figure('Position', [200, 200, 800, 400]);  
plot(x/0.065, I_SOC);  
xlim([-3 3])
```

```
% case 1: k=0 for 50/50 population

x = -4.5:0.0001:4.5;
y = (normpdf(x,-3,0.02)+normpdf(x,-2,0.02)+normpdf(x,
-1,0.02)+normpdf(x,0,0.02)+normpdf(x,1,0.02)+normpdf(x,
2,0.02)+normpdf(x,3,0.02));
z1 = 1 + cos(-pi*x);
z2 = 1 + cos(pi-pi*x);
w = normpdf(x,0, 1.5)*7.5;

FigureHandle = figure('Position',[200, 200, 800, 400]);
subplot(2,1,1);
plot(x,y);hold on;
plot(x,z1);
plot(x,w);
ylim([0 2]);
xlim([-4 4]);
xlabel('q / [2\pi/d]');
%title('\phi = 0');

subplot(2,1,2);
plot(x,y);hold on;
plot(x,z2);
plot(x,w);
ylim([0 2]);
xlim([-4 4]);
xlabel('q / [2\pi/d]');
%title('\phi = \pi');

% case 2: k=+/- k_L for 100/0 population with only OC or
SOC

x = -4.5:0.0001:4.5;
y = (normpdf(x,-3.5,0.02)+normpdf(x,-3,0.02)+normpdf(x,
-2.5,0.02)+normpdf(x,-2,0.02)+normpdf(x,-1.5,0.02)+normpdf
(x,-1,0.02)+normpdf(x,-0.5,0.02)+normpdf(x,0,0.02)+normpdf
(x,0.5,0.02)+normpdf(x,1,0.02)+normpdf(x,1.5,0.02)+normpdf
```

```
(x,2,0.02)+normpdf(x,2.5,0.02)+normpdf(x,3,0.02)+normpdf(x,
3.5,0.02));
    z1 = 1 + cos(-2*pi*x+pi);
    w = normpdf(x,0, 0.75)*3.75;

    FigHandle = figure('Position',[200, 200, 800, 200]);
    plot(x,y);hold on;
    plot(x,z1);
    plot(x,w);
    ylim([0 2]);
    xlim([-4 4]);
    xlabel('q / [2\pi/d]');

% case 3: k=+/- k_L for 100/0 population with both OC and
SOC

    x = -4.5:0.0001:4.5;
    y = (normpdf(x,-3.5,0.02)+normpdf(x,-3,0.02)+normpdf(x,
-2.5,0.02)+normpdf(x,-2,0.02)+normpdf(x,-1.5,0.02)+normpdf
(x,-1,0.02)+normpdf(x,-0.5,0.02)+normpdf(x,0,0.02)+normpdf
(x,0.5,0.02)+normpdf(x,1,0.02)+normpdf(x,1.5,0.02)+normpdf
(x,2,0.02)+normpdf(x,2.5,0.02)+normpdf(x,3,0.02)+normpdf(x,
3.5,0.02));
    z1 = 1 + cos(-2*pi*x+pi);
    z2 = 1 + cos(-pi*x-3*pi/4);
    w = normpdf(x,0, 0.75)*3.75;

    FigHandle = figure('Position',[200, 200, 800, 400]);
subplot(2,1,1);
    plot(x,y);hold on;
    plot(x,z1);
    plot(x,w); plot(x,z2);
    fn = y.*z1.*z2.*w/80;plot(x,fn);
    ylim([0 2]);
    xlim([-4 4]);
    xlabel('q / [2\pi/d]');
```

```
subplot(2,1,2);
z1 = 1 + cos(-2*pi*x+pi);
z2 = 1 + cos(-pi*x+pi/4);
plot(x,y);hold on;
plot(x,z1);
plot(x,w); plot(x,z2);
fn = y.*z1.*z2.*w/80;plot(x,fn);
ylim([0 2]);
xlim([-4 4]);
xlabel('q / [2\pi/d]');

% case 4: No interference between quasi-momentum q=0 and
q=k_L states

x = -4.5:0.0001:4.5;
y = (normpdf(x,-3.5,0.02)+normpdf(x,-3,0.02)+normpdf(x,
-2.5,0.02)+normpdf(x,-2,0.02)+normpdf(x,-1.5,0.02)+normpdf
(x,-1,0.02)+normpdf(x,-0.5,0.02)+normpdf(x,0,0.02)+normpdf
(x,0.5,0.02)+normpdf(x,1,0.02)+normpdf(x,1.5,0.02)+normpdf
(x,2,0.02)+normpdf(x,2.5,0.02)+normpdf(x,3,0.02)+normpdf(x,
3.5,0.02));
z1 = 1 + sin(pi/4-pi*x).*sin(2*pi*x);
w = normpdf(x,0, 0.75)*3.75;

FigHandle = figure('Position',[200, 200, 800, 200]);
plot(x,y);hold on;
plot(x,z1);
plot(x,w);
fn = y.*z1.*w/40;plot(x,fn);
ylim([0 2]);
xlim([-4 4]);
xlabel('q / [2\pi/d]');
```

# Bibliography

- [1] Dallin S. Durfee. *Dynamic Properties of Dilute Bose-Einstein Condensates*. PhD thesis, MIT, 1999. An optional note.
- [2] Zoran Hadzibabic. *Studies of a quantum degenerate fermionic lithium gas*. PhD thesis, MIT, 2003. An optional note.
- [3] J K Chin, D E Miller, Y Liu, C Stan, W Setiawan, C Sanner, K Xu, and W Ketterle. Evidence for superfluidity of ultracold fermions in an optical lattice. *Nature*, 443(7114):961–964, October 2006.
- [4] D E Miller, J K Chin, C A Stan, Y Liu, W Setiawan, C Sanner, and W Ketterle. Critical Velocity for Superfluid Flow across the BEC-BCS Crossover. *Physical Review Letters*, 99(7):070402, August 2007.
- [5] Waseem S Bakr, Jonathon I Gillen, Amy Peng, Simon Fölling, and Markus Greiner. A quantum gas microscope for detecting single atoms in a Hubbard-regime optical lattice. *Nature*, 462(7269):74–77, November 2009.
- [6] Cheng-Hsun Wu. *Strongly Interacting Quantum Mixtures of Ultracold Atoms*. PhD thesis, MIT, 2013. An optional note.
- [7] Aviv Keshet. *A Next-Generation Apparatus for Lithium Optical Lattice Experiments*. PhD thesis, MIT, 2012. An optional note.
- [8] Edward Su. *Fluctuations and State Preparation in Quantum Degenerate Gases of Sodium and Lithium*. PhD thesis, MIT, 2014. An optional note.
- [9] Dan M. Stamper-Kurn. *Peeking and poking at a new quantum fluid: Studies of gaseous Bose-Einstein condensates in magnetic and optical traps*. PhD thesis, MIT, 1999. An optional note.
- [10] M H Anderson, J R Ensher, M R Matthews, C E Wieman, and E A Cornell. Observation of Bose-Einstein Condensation in a Dilute Atomic Vapor. *Science*, 269(5221):198–201, July 1995.
- [11] K B Davis, M O Mewes, M R Andrews, N J van Druten, D S Durfee, D M Kurn, and W Ketterle. Bose-Einstein Condensation in a Gas of Sodium Atoms. *Physical Review Letters*, 75(22):3969–3973, November 1995.

- [12] Y J Lin, A R Perry, R L Compton, I B Spielman, and J V Porto. Rapid production of R87bBose-Einstein condensates in a combined magnetic and optical potential. *Physical Review A*, 79(6):063631, June 2009.
- [13] Wolfgang Ketterle, Kendall B Davis, Michael A Joffe, Alex Martin, and David E Pritchard. High densities of cold atoms in a darkspontaneous-force optical trap. *Physical Review Letters*, 70(15):2253–2256, April 1993.
- [14] Gretchen K Campbell, Jongchul Mun, Micah Boyd, Patrick Medley, Aaron E Leanhardt, Luis G Marcassa, David E Pritchard, and Wolfgang Ketterle. Imaging the Mott Insulator Shells by Using Atomic Clock Shifts. *Science*, 313(5787):649–652, August 2006.
- [15] Markus Greiner, Olaf Mandel, Tilman Esslinger, Theodor W Hänsch, and Immanuel Bloch. Quantum phase transition from a superfluid to a Mott insulator in a gas of ultracold atoms. *Nature*, 415(6867):39–44, January 2002.
- [16] W S Bakr, A Peng, M E Tai, R Ma, J Simon, J I Gillen, S Fölling, L Pollet, and M Greiner. Probing the Superfluid-to-Mott Insulator Transition at the Single-Atom Level. *Science*, 329(5991):547–550, July 2010.
- [17] Jacob F Sherson, Christof Weitenberg, Manuel Endres, Marc Cheneau, Immanuel Bloch, and Stefan Kuhr. Single-Atom Resolved Fluorescence Imaging of an Atomic Mott Insulator. *arXiv.org*, June 2010.
- [18] Chen-Lung Hung, Xibo Zhang, Nathan Gemelke, and Cheng Chin. Observation of scale invariance and universality in two-dimensional Bose gases. *Nature*, 470(7333):236–239, February 2011.
- [19] Robert Jördens, Niels Strohmaier, Kenneth Günter, Henning Moritz, and Tilman Esslinger. A Mott insulator of fermionic atoms in an optical lattice. *Nature*, 455(7210):204–207, September 2008.
- [20] U Schneider, L Hackermüller, S Will, Th Best, I Bloch, T A Costi, R W Helmes, D Rasch, and A Rosch. Metallic and Insulating Phases of Repulsively Interacting Fermions in a 3D Optical Lattice. *Science*, 322(5907):1520–1525, December 2008.
- [21] R Jördens, L Tarruell, D Greif, T Uehlinger, N Strohmaier, H Moritz, T Esslinger, L De Leo, C Kollath, A Georges, V Scarola, L Pollet, E Burovski, E Kozik, and M Troyer. Quantitative Determination of Temperature in the Approach to Magnetic Order of Ultracold Fermions in an Optical Lattice. *Physical Review Letters*, 104(18):180401, May 2010.
- [22] Russell A Hart, Pedro M Duarte, Tsung-Lin Yang, Xinxing Liu, Thereza Paiva, Ehsan Khatami, Richard T Scalettar, Nandini Trivedi, David A Huse, and Randall G Hulet. Observation of antiferromagnetic correlations in the Hubbard model with ultracold atoms. *Nature*, 519(7542):211–214, March 2015.

- [23] M Aidelsburger, M Atala, S Nascimbène, S Trotzky, Y A Chen, and I Bloch. Experimental Realization of Strong Effective Magnetic Fields in an Optical Lattice. *Physical Review Letters*, 107(25):255301, December 2011.
- [24] M Aidelsburger, M Atala, M Lohse, J T Barreiro, B Paredes, and I Bloch. Realization of the Hofstadter Hamiltonian with Ultracold Atoms in Optical Lattices. *Physical Review Letters*, 111(18):185301, October 2013.
- [25] Hirokazu Miyake, Georgios A Siviloglou, Colin J Kennedy, William Cody Burton, and Wolfgang Ketterle. Realizing the Harper Hamiltonian with Laser-Assisted Tunneling in Optical Lattices. *Physical Review Letters*, 111(18):185302, October 2013.
- [26] Colin J Kennedy, William Cody Burton, Woo Chang Chung, and Wolfgang Ketterle. Observation of Bose–Einstein condensation in a strong synthetic magnetic field. *Nature Physics*, August 2015.
- [27] M Aidelsburger, M Lohse, C Schweizer, M Atala, J T Barreiro, S Nascimbène, N R Cooper, I Bloch, and N Goldman. Measuring the Chern number of Hofstadter bands with ultracold bosonic atoms. *Nature Physics*, 11(2):162–166, February 2015.
- [28] Gregor Jotzu, Michael Messer, Rémi Desbuquois, Martin Lebrat, Thomas Uehlinger, Daniel Greif, and Tilman Esslinger. Experimental realization of the topological Haldane model with ultracold fermions. *Nature*, 515(7526):237–240, November 2014.
- [29] S Inouye, M R Andrews, J Stenger, H J Miesner, D M Stamper-Kurn, and W Ketterle. Observation of Feshbach resonances in a Bose—[ndash]—Einstein condensate. *Nature*, 392(6672):151–154, March 1998.
- [30] Antoine Georges. Condensed Matter Physics With Light And Atoms: Strongly Correlated Cold Fermions in Optical Lattices. *arXiv.org*, February 2007.
- [31] Nathan Gemelke, Xibo Zhang, Chen-Lung Hung, and Cheng Chin. In situ observation of incompressible Mott-insulating domains in ultracold atomic gases. *Nature*, 460(7258):995–998, August 2009.
- [32] M. Z. Hasan and C. L. Kane. *Colloquium* : Topological insulators. *Rev. Mod. Phys.*, 82:3045–3067, Nov 2010.
- [33] Xiao-Liang Qi and Shou-Cheng Zhang. Topological insulators and superconductors. *Rev. Mod. Phys.*, 83:1057–1110, Oct 2011.
- [34] Y J Lin, K Jiménez-García, and I B Spielman. Spin-orbit-coupled Bose-Einstein condensates. *Nature*, 471(7336):83–86, March 2011.

- [35] Pengjun Wang, Zeng-Qiang Yu, Zhengkun Fu, Jiao Miao, Lianghai Huang, Shijie Chai, Hui Zhai, and Jing Zhang. Spin-Orbit Coupled Degenerate Fermi Gases. *Physical Review Letters*, 109(9):095301, August 2012.
- [36] Lawrence W Cheuk, Ariel T Sommer, Zoran Hadzibabic, Tarik Yefsah, Waseem S Bakr, and Martin W Zwierlein. Spin-Injection Spectroscopy of a Spin-Orbit Coupled Fermi Gas. *Physical Review Letters*, 109(9):095302, August 2012.
- [37] S Chaitanya Kumar, G K Samanta, and M Ebrahim-Zadeh. High-power, single-frequency, continuous-wave second-harmonic-generation of ytterbium fiber laser in PPKTP and MgO:sPPLT. *Optics Express*, 17(16):13711–13726, August 2009.
- [38] Chunji Wang, Chao Gao, Chao-Ming Jian, and Hui Zhai. Spin-Orbit Coupled Spinor Bose-Einstein Condensates. *Physical Review Letters*, 105(16):160403, October 2010.
- [39] Yun Li, Lev P Pitaevskii, and Sandro Stringari. Quantum Tricriticality and Phase Transitions in Spin-Orbit Coupled Bose-Einstein Condensates. *Physical Review Letters*, 108(22):225301, May 2012.
- [40] Christian Sanner, Edward J Su, Aviv Keshet, Ralf Gommers, Yong-il Shin, Wujie Huang, and Wolfgang Ketterle. Suppression of Density Fluctuations in a Quantum Degenerate Fermi Gas. *Physical Review Letters*, 105(4):040402, July 2010.
- [41] Christian Sanner, Edward J Su, Aviv Keshet, Wujie Huang, Jonathon Gillen, Ralf Gommers, and Wolfgang Ketterle. Speckle Imaging of Spin Fluctuations in a Strongly Interacting Fermi Gas. *Physical Review Letters*, 106(1):010402, January 2011.
- [42] Christian Sanner, Edward J Su, Wujie Huang, Aviv Keshet, Jonathon Gillen, and Wolfgang Ketterle. Correlations and Pair Formation in a Repulsively Interacting Fermi Gas. *Physical Review Letters*, 108(24):240404, June 2012.
- [43] Christian Sanner. *Fluctuations in Quantum Degenerate Fermi Gases*. PhD thesis, University of Heidelberg, 2012. An optional note.